Towards a realistic estimation of the walls moisture buffering in an occupied room

Rudy Bui

Université Fédérale

Toulouse Midi-Pyrénées

THÈSE

En vue de l'obtention du

DOCTORAT DE L'UNIVERSITÉ DE TOULOUSE

Délivré par : *l'Université Toulouse 3 Paul Sabatier (UT3 Paul Sabatier)*
Discipline ou spécialité : *Génie Civil*

Présentée et soutenue par

Rudy BUI

Le 30 Novembre 2018

Towards a realistic estimation of the walls moisture buffering in an occupied room

---

JURY

Monika WOLOSZYN, Université Savoie Mont Blanc (Rapporteur)
Antonin FABBRI, Ecole Nationale des Travaux Publics de l'Etat (Rapporteur)
Christian INARD, Université de La Rochelle (Examinateur)
Thibaut COLINART, Université Bretagne Sud (Examinateur)
Sylvie LORENTE, Institut National des Sciences Appliquées Toulouse (Directrice de thèse)
Matthieu LABAT, Institut National des Sciences Appliquées Toulouse (Directeur de thèse)

Ecole doctorale : *Mécanique, Energétique, Génie civil et Procédés (MEGeP)*
Unité de recherche : *Laboratoire Matériaux et Durabilité des Constructions (LMDC)*
Directeur(s) de Thèse : *Sylvie LORENTE et Matthieu LABAT*

Abstract

Humidity in buildings has nowadays become a major concern as it impacts simultaneously the energy consumption, the occupants' comfort and the moisture related risks in the buildings envelope. Buildings materials have the ability to absorb and release large amounts of moisture and therefore they may dampen the indoor relative humidity variations. This is called the moisture buffering capacity. It depends on the vapour exchanges between the air and the walls, the ventilation and the indoor moisture sources. This property was previously highlighted at material and wall scales through laboratory experiments and numerical models. However, few models describe the indoor sources due to the occupants' presence and activities in a realistic way.

In this work, a hygrothermal room model was developed in *Python* to investigate the influence of the occupancy scenario and of the impact of the walls moisture buffering on indoor air balance. This model regroups the coupled heat and mass transfer in the walls, as well as the indoor sources depicted by the air-conditioning system and the occupants' presence and activities. The numerical modelling of the latter relies on a stochastic occupancy model implemented in a platform called NoMASS. Performance indicators on the energy demand, the indoor hygric comfort and the moisture related risks in the walls were defined to quantify the hygothermal performance of a room.

The sensitivity of the performance indicators towards the occupancy scenario was assessed by simulating a stochastic occupancy scenario, a deterministic one and a constant one. Results showed a marginal influence of the scenario at year scale. However, at smaller time scales (seasonal or monthly), their impact on the indoor relative humidity dampening was not negligible, mainly due to the consideration of a seasonal effect for the stochastic scenario. The walls moisture buffering impact on the performance indicators was estimated by simulating a room subjected to different climates. The buffering effect was emphasised by applying a hygroscopic plaster on the walls. While its impact on indoor air was not noticeable at year scale, the indoor relative humidity variations could be dampened at smaller time scales, especially at week and day scales, highlighting the importance of describing accurately the indoor sources.

Keywords

moisture buffering, heat and mass transfer, occupants' presence modelling, hygrothermal performance, numerical modelling

Résumé

De nos jours, l'humidité dans les bâtiments est une problématique majeure car elle impacte simultanément la consommation énergétique, le confort des occupants, ainsi que les risques de moisissures dans l'envelope du bâtiment. Les matériaux de construction ont la capacité d'absorber et de libérer de grandes quantités de vapeur d'eau et peuvent par conséquent amortir les variations d'humidité relative intérieure. Cette proporiété est appelée tampon hygrique. Elle est liée aux échanges de vapeur d'eau entre l'air intérieur et les parois, à la ventilation, et aux sources de vapeur. Cet effet a été précédemment mis en évidence à l'échelle du matériau et de la paroi par des expériences de laboratoire et des modèles numériques. Cependant, peu de modèles décrivent de manière réaliste les sources intérieures dues à la présence et aux activités des occupants.

Dans ce travail, un modèle hygrothermique à l'échelle de la pièce a été développé en *Python* afin d'investiguer l'influence du scénario d'occupation, et l'impact du tampon hygrique des parois sur l'air intérieur. Ce modèle regroupe les transferts couplés d'énergie et de masse dans les parois, ainsi que les sources intérieures décrites par un système de conditionnement d'air et par la présence et les activités des occupants. Ce dernier étant modélisé de manière stochastique par un modèle implémenté dans une plateforme nommée No-MASS. Des indicateurs de performance sur les besoins énergétiques, le confort hygrique intérieur, et les risques liés aux moisissures dans les parois ont été définis pour quantifier la performance hygrothermique d'une pièce.

La sensibilité des indicateurs de performance vis-à-vis du scénario d'occupation a été évaluée en simulant des scénarios stochastique, déterministe et constant. Les résultats ont montré une influence marginale du scénario à l'échelle de l'année. Cependant, à des échelles plus courtes (saison ou mois) l'impact du scénario est non négligeable, notamment dû à la prise en compte d'un effet saisonnier pour le scénario stochastique. L'impact du tampon hygrique des parois sur les indicateurs de performance a été estimé en simulant une pièce exposée à différents climats. L'effet tampon a été mis en avant en appliquant un enduit hygroscopique sur les parois. Bien que son impact sur l'air intérieur ne soit que peu visible à l'échelle de l'année, les variations d'humidité relative peuvent être atténuées à plus courtes échelles, notamment à l'échelle de la semaine et de la journée, mettant en évidence l'importance de décrire les sources intérieures de manière précise.

Mots-clés

tampon hygrique, transferts de chaleur et de masse, modélisation de la présence des occupants, performance hygrothermique, modélisation numérique

Remerciements

Ces travaux de thèse ont été réalisés au Laboratoire Matériaux et Durabilité des Constructions de Toulouse (LMDC) de Septembre 2015 à Novembre 2018, et financés par le Ministère de l'Enseignement Supérieur et de la Recherche. Je remercie Gilles Escadeillas et Alain Sellier, directeurs du LMDC durant cette période, pour m'avoir accueilli au sein du LMDC.

Je tiens tout d'abord à remercier l'ensemble des membres de mon jury : Monika Woloszyn et Antonin Fabbri pour m'avoir fait l'honneur d'accepter de rapporter ce travail, Christian Inard pour avoir présidé mon jury et Thibaut Colinart pour avoir examiné ma thèse. Je salue votre dévouement pour avoir digéré 164 pages sur de la modélisation. Je vous remercie aussi pour les échanges enrichissants que nous avons eu sur de nombreux points abordés dans mon travail.

Je remercie chaleureusement mes directeurs de thèse Sylvie Lorente et Matthieu Labat pour m'avoir encadré et accompagné tout au long de ces 38 mois. Au début de ma thèse, je n'étais qu'un simple débutant en modélisation. Cependant, votre patience et votre pédagogie m'ont permis d'apprendre la rigueur nécessaire à l'élaboration de ce travail de recherche. Je me sens très honoré et heureux d'avoir été formé par vous, et j'espère que nous aurons à nouveau l'opportunité de travailler ensemble.

Je remercie aussi l'ensemble du personnel du laboratoire, notamment Fabienne et Ghislaine pour leur énorme travail. J'exprime particulièrement ma gratitude envers Stéphane Multon qui m'a soutenu tout au long de mon cursus de Licence et Master à l'Université de Toulouse, et qui m'a sensibilisé à la recherche. Et aussi envers Jean-Emmanuel Aubert qui m'a encadré durant mon stage de recherche et introduit aux matériaux biosourcés ainsi qu'aux problématiques liées à l'humidité.

Je tiens à remercier l'équipe de The University of Sheffield — School of Architecture, Darren Robinson et Jacob Chapman, pour notre collaboration durant cinq

mois qui a conduit au développement d'une partie majeure de ma thèse.

Je remercie bien sûr mes collègues et amis doctorants et ex-doctorants : Aurélie pour les gâteaux et les 409 mots fléchés (et les 20 g de paille à couper...), Lucie pour les nombreux "instants rafraîchissement", les chercheurs de l'axe Energie Constructions Confort : Billy, Sophie, Alexandre et Mohamed pour tous les échanges scientifiques qu'on a pu avoir sur nos sujets de recherche. Je remercie aussi Célimène, Nuraziz, Julie, Emanuel, Mathilde, Elie, Yvan, Bernard, Ponleu, Moustapha, Khadim, Souad et Daniéla, en espérant n'oublier personne.

Je tiens à remercier à nouveau Célimène pour le fort soutien moral tout au long de ma thèse, Alexandre pour tous les moments passés ensemble au labo et en dehors, et bien sûr Billy ; un jour notre projet aboutira et nous ferons fortune !

Enfin, j'adresse mes derniers remerciements à tous ceux qui n'ont aucun lien avec le LMDC mais dont le soutien m'a été primordial. A mes parents, mon frère et sa famille ; à Martine et Joëlle pour les cafés et votre bonne humeur communicative ; et à mes amis proches : mon cher ami d'enfance Rémy, assoc' Youssouf, Yann le mousquetaire, boss Anaïs, papa Alex, ma première stagiaire Claire, Samuel, Christel et sa famille, Delphine, et padawan Kimi.

... in real life mistakes are likely to be irrevocable. Computer simulation, however, makes it economically practical to make mistakes on purpose. [...], if you are at all discreet, no one but you need ever know you made a mistake.

John H. Mcleod

Contents

List of Figures

List of Tables

Nomenclature

Greek letters

β	Thermal expansion coefficient $(1/K)$
δ	Permeability $(kg/(m.s.Pa))$ or (s)
ϵ	Emissivity
γ	Fractional year (rad)
κ	Absorptivity
μ	Factor of mobility
Φ	Angle of inclination $(°)$
Ψ	Relative humidity
ρ	Density (kg/m^3)
σ	Stefan-Boltzman constant $(W/(m^2.K^4))$
ξ	Hygric capacity (kg_v/kg_{mat})

Latin letters

$\dot{m}$, g	Vapour flux (kg/s)
$\dot{Q}$	Heat flux (W)
A	Surface (m^2)
A_z	Azimuth $(°)$
Alb	Albedo
AST	Apparent Solar Time
b_m	Moisture effusivity $(kg/(m^2.Pa.s^{1/2}))$
C	Correction
c_p	Heat capacity $(J/(kg.K))$

cf	Covering factor
D	Coefficient of diffusion (m^2/s)
d	Pore diameter (m)
Dif	Diffuse
Dir	Direct
dx	Mesh size (m)
e	Specific internal energy (J)
E_T	Equation of Time
Err	Error
h	Specific enthalpy (J/kg)
h_h	Convective heat transfer coefficent $(W/(m^2.K))$
h_m	Convective mass transfer coefficent $(kg/(m^2.s.Pa))$
HAM	Heat Air Moisture
k	Thermal conductivity $(W/(m.K))$
K_n	Knudsen number
L	Longitude
L_v	Latent heat of vaporisation (J/kg)
L_{pm}	Free mean path (m)
LWR	Long-Wave Radiation
M	Molar mass (kg/mol)
m	Mass (kg)
MBV	Moisture Buffering Value $(g/(m^2.\%))$
MI	Mould Index
MST	Mean Solar Time
P	Probability
p	Pressure (Pa)
q	Progressive factor
R	Ideal gas constant $(J/(kg.K))$

Ref	Reflected
RH	Relative humidity (%)
S	Source (W) or (kg/s)
SWR	Short-Wave Radiation
T	Temperature (K)
t	Time (s)
Tol	Tolerance
u	Water content (kg_v/kg_{mat})
UT	Universal Time
V	Wind velocity (m/s)
w	Water content (kg/m^3)
X	Random variable
x	Mass ratio
Z	Sun altitude (m)

Subscripts

a	Air
AC	Air-conditioner
atm	Atmosphere
c	Capillary
$conv$	Convective
$crit$	Critical
$dehumid$	Dehumidification
$diff$	Diffusion
es	Exterior surface
ext	Exterior
gro	Ground
H	Horizontal
h	Heat

humid	Humidification
int	Interior
is	Interior surface
l	Liquid
loc	Local
m	Mass
mat	Material
N	Normal
opt	Optimal
sat	Saturated
v	Vapour
ventil	Ventilation

Scope

Many agreements have already been signed to tackle global warming, starting with the Rio's summit in 1992 and Kyoto's protocol in 2005. More recently, the Paris' agreement in 2016 aimed to limit the global warming under 2°C per year. Lots of efforts are needed in the building sector, as it is a large contributor to global warming. For example, in France, it corresponds to around 45% of the total energy consumption according to Dixit et al. (2010). Heating Ventilation and Air-Conditioning (HVAC) systems are the most energy consuming systems, corresponding to approximately 50% of the global consumption of buildings (Perez-Lombard et al., 2011), mostly for tertiary buildings. As there is an urgent need to reduce the energy consumption, new thermal regulations started to appear leading to the creation of labels like Passivhaus in Germany, the High Environmental Quality in France or the LEED certification among others.

The most simple and obvious solution to reduce the energy consumption is to improve the buildings insulation performances. However, making airtight buildings brought also new issues, especially the ones related to humidity which does not only impact the energy consumption, but also the occupants' comfort and the durability of materials. This became a major concern and projects started in France to predict the issues related to humidity (project HUMIBATex) or to propose a hygrothermal conception method (project HYGRO-BAT). Other national and international projects were conducted on this topic; an exhaustive state of the art on older projects can be found in Piot (2009).

A recent alternative to reduce the energy consumption of buildings and to limit their environmental impact is to rely on biobased materials. They offer a relatively good thermal insulation and have a low environmental impact as they usually come from agricultural waste. These materials also have the property of absorbing (or releasing) large amounts of humidity when they are subjected to humidity variations. Hence, they may smooth the humidity in a passive way. According to Diasty et al. (1992), this property can contribute to as much as one third of the global humidity regulation of the indoor air depending on the material. Exploiting this

property could lead to energy savings by reducing the humidifying and dehumidifying needs, or could improve the hygric comfort by dampening the indoor relative humidities. Yet, despite these advantages, biobased materials are sensitive to high relative humidities. Mould growth may be observed, affecting the durability of materials and the occupants' health. Recently, project BIOTERRA (ended in 2018) aimed at identifying the mould growth at material scale and at proposing solutions to contain it.

Therefore, assessing the indoor air hygrothermal conditions of a room has nowadays become a major research topic. It combines complex phenomena impacting simultaneously the energy consumption of buildings, the hygric comfort and also the moisture related risks affecting the construction materials and the occupants' health. As stated by Diasty et al. (1992), the main factors influencing indoor air balance are the ventilation system, the interaction between the indoor air and the materials, as well as the indoor sources.

In this context, our work aimed at contributing to the ongoing researches on the impact of humidity in buildings. A numerical methodology is proposed in order to estimate the influence of the walls materials on indoor humidity. Special attention was dedicated to the modelling of the occupants' presence and activities in buildings. We relied on a stochastic approach which has been recently used in the energy performance field.

Chapter 1

Factors influencing the indoor air humidity in buildings

Contents

1.1 Introduction

Numerous factors impact the hygrothermal balance in a room: the interactions between the indoor air and the materials, the ventilation systems and the indoor sources.

Ventilation systems have been extensively investigated in the literature, from a simple constant ventilation rate, as exemplified in Künzel et al. (2005), to a Relative Humidity Sensitive (RHS) ventilation (investigated by Afshari and Bergsoe (2003) or Savin et al. (2005) among others). A state of the art on the existing technologies for meeting residential ventilation requirements can be found in Walker and Sherman (2006) and Cao et al. (2014). Their impact on the hygrothermal balance of a room and on the moisture buffering of the walls was also highlighted by numerous studies (Knabe and Le (2001), Woloszyn et al. (2009), ...). Consequently, the work presented in this report does not focus on the ventilation systems.

The interaction between the indoor air and the walls is interrelated to the materials ability to absorb or release moisture when they are subjected to humidity variations: this is called the moisture buffering effect (Hameury, 2005). The materials could therefore dampened the humidity variations in buildings. This phenomenon has been observed and investigated at both material and wall scales.

1.1.1 Moisture buffering effect at material scale

At material scale, the most widespread indicator is the *Moisture Buffering Value* (MBV) defined in the Nordtest protocol (Rode et al., 2005), expressed in $(g/(m^2.\%))$. It defines the ability of a material to absorb and desorb humidity when it is subjected to humidity variations cycles alternating from high to low humidities according to a sine function. Its theoretical value can be calculated with Eq. (1.1):

$$MBV_{ideal} = 0.00568 \cdot p_{v,sat} \cdot b_m \cdot \sqrt{t_p} \tag{1.1}$$

where the coefficient 0.00568 is deduced by assuming a 8/16 hours scheme at high/low humidities (see Rode et al. (2005) for details on its calculation), $p_{v,sat}$ is the saturated water vapour pressure (Pa), t_p is the time period (s) and b_m is the moisture effusivity calculated as follows:

$$b_m = \sqrt{\frac{\delta_v \cdot \rho_{mat} \cdot \frac{\partial u}{\partial \Psi}}{p_{v,sat}}} \tag{1.2}$$

where δ_v is the water vapour permeability of the material $(kg/(m.s.Pa))$, ρ_{mat} is its dry density (kg/m^3), u is the water content (kg_v/kg_{mat}) and Ψ is the relative humidity (%). The moisture effusivity expresses the rate of moisture absorbed by a material when it is subjected to an increase of relative humidity under steady state and equilibrium conditions. As these conditions are hardly respected in buildings, the practical MBV is defined and is measured by an experiment consisting on subjecting a sample to several cycle of humidity from 33% to 75% for 16 and 8 hours respectively (meaning that $t_p = 24$ h). These cycles aimed at emulating the humidity variations in a room throughout a day. The MBV is then calculated by measuring the mass variation of the sample, leading directly to the amount of absorbed (or desorbed) moisture by the material:

$$MBV_{practical} = \frac{\Delta m}{A \cdot \Delta\Psi} \tag{1.3}$$

where Δm is the mass variation of the sample during the 8h or 16h phase (kg), A is the total exchange surface (m^2) and $\Delta\Psi$ is the difference between the high and low relative humidity of the cycle. The experiment is illustrated in Figure 1.1 (Rode et al., 2005).

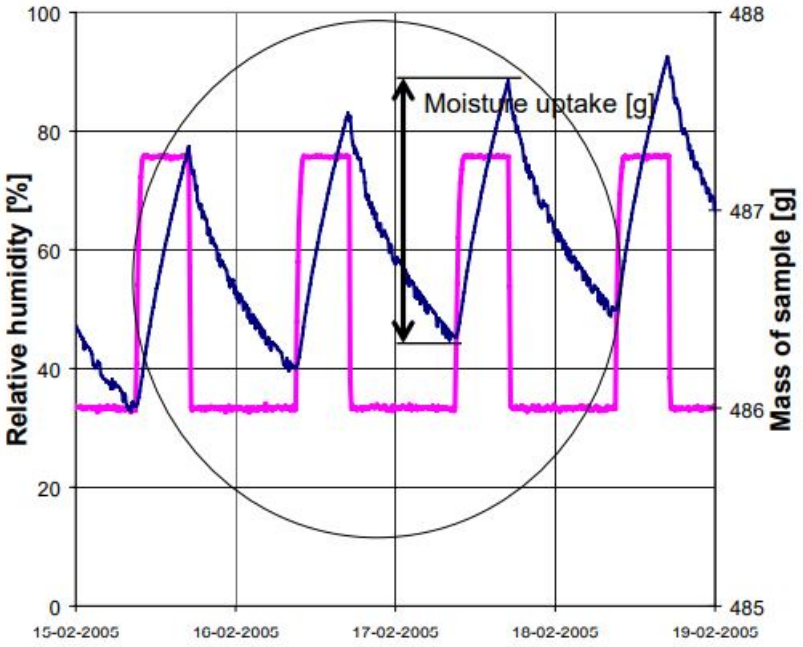

Figure 1.1 – Measurement of the $MBV_{practical}$, where the circle represents the quasi-steady state between 3 cycles (Rode et al., 2005)

Another indicator defined in the Nordtest protocol is the moisture penetration depth. It corresponds to the depth where the amplitude of moisture content variations represents 1% of its variation on the surface, when the material is subjected

to relative humidity variations corresponding to a MBV test. It is calculated by Eq. (1.4):

$$d_{p,1\%} = 4.61\sqrt{\frac{D_w t_p}{\pi}} \tag{1.4}$$

where $d_{p,1\%}$ is the moisture penetration depth (m) and D_w is the moisture diffusivity of the material given by Eq. (1.5):

$$D_w = \frac{\delta_v p_{v,sat}}{\xi} \tag{1.5}$$

where ξ is the hygric capacity of the material (kg_v/kg_{mat}).

The MBV has been measured for numerous materials in the literature. For example McGregor et al. (2014) investigated it for unfired clay masonry. They estimated the impact of the vapour diffusion with two tests: a static test by putting a clay sample in a climatic chamber, and a dynamic one by using a Dynamic Vapour Sorption device (see Bui et al. (2017a) for details on the device). They highlighted that the main factor influencing the MBV is vapour diffusion through the material as a slow diffusion would reduce the overall buffering potential.

Cerolini et al. (2009) estimated the MBV of polyacrylate and a cellulose-based material. They stated that both materials have an "excellent" MBV according to the Nordtest classification (Rode et al., 2005). However, the hysteretic behaviour of the polyacrylate did not allow it to discharge the water absorbed and thus it could become saturated in time. This was not the case for the cellulose-based material.

Additionally, Dubois et al. (2014) measured the MBV of clay masonry subjected to 50/85% humidity cycles. They also proposed an inverse modelling approach to deduce the hygric properties (hygric capacity and vapour permeability) from the MBV measurements using Bayesian techniques.

These are just few examples among others, but there is strong consensus that the main factors influencing the buffering capacity of a material are its hygric capacity and its water vapour permeability.

1.1.2 Moisture buffering effect at wall scale

While the buffering property has been extensively studied at material scale, some researches were conducted at wall scale. At this scale, it is already known that the moisture buffering of materials has a non-negligible impact on indoor air balance. For example, in the case of high moisture loads corresponding to a peak of vapour production in a kitchen, the moisture buffering of materials could absorbed about half of the moisture according to Plathner and Woloszyn (2002).

Hameury (2005) numerically investigated the buffering capacity of heavy timber structures exposed to indoor climate. A room envelope made of heavy timber was simulated. A constant indoor moisture source equal to 60 g/h or 120 g/h was added during the night while the exterior conditions were kept constant. Results showed that the indoor relative humidity was smoothed as the amplitude in humidity represented 73% of what would have occurred if the walls were moisture impermeable.

Woloszyn et al. (2009) studied a one-story test building located in Germany which indoor walls materials were in wood fibreboard. The air was controlled at 20°C and a cyclic moisture source ranging from 200 to 400 g/h. By combining a RHS ventilation type and the buffering capacity of the wood they managed to keep the indoor humidity between 43 and 59%.

Additionally, Yoshino et al. (2009) estimated experimentally the moisture buffering of gypsum boards installed in a test chamber. Their experiment is illustrated by Figure 1.2.

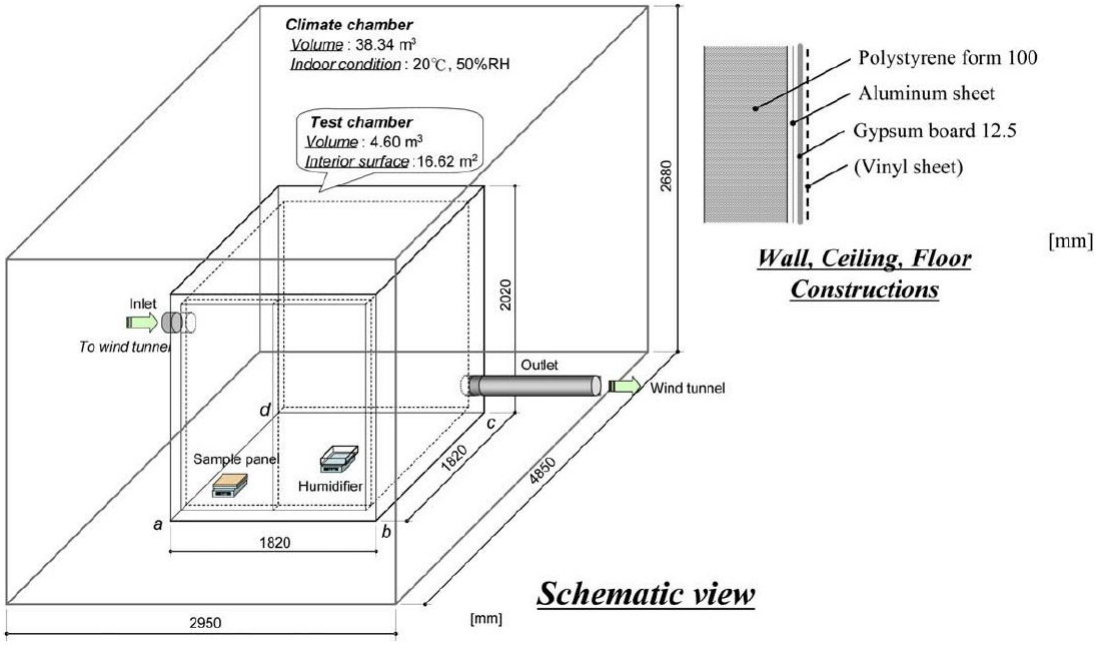

Figure 1.2 – Schematic view of the test chamber from Yoshino et al. (2009)

The experiment consisted in adding a constant moisture source of approximately 20 g/h for 6h, followed by 12h without humidification. Different ventilation rates were tested ranging from 0 to 5 h^{-1}. Yoshino et al. (2009) highlighted that the effectiveness of the gypsum board moisture buffering was reduced when the ventilation rate was increased. According to the authors, this was previously showed by Sakamoto et al. (1996) for residential buildings. The comparison between their experimental results with numerous simulations tools showed significant discrepancies between models, especially when no ventilation was simulated. The authors indicate

that these deviations came from the different description of the exchange between the air and the walls from one model to another. But no more details were given on this topic.

Li et al. (2012) measured experimentally the MBV of wood panels installed in a test room, in which a ventilation system and a moisture source were added. This experiment was similar to Yoshino et al. (2009) one. The exterior conditions were fixed and they investigated the variation of the ventilation rate (from 0 to 0.75 ACH) and the moisture sources (a constant source with a rate ranging from 25 to 58 g/h depending on the case study). They concluded that the indoor humidity could be dampened up to 17% by the buffering property of the wood panels.

Similarly, in Yang et al. (2012), the moisture buffering behaviour of uncoated gypsum board and wood panelling was measured in a test hut in which a cyclic moisture source ranging from 55.5 g/h to 200.2 g/h was added. They defined a new indicator: the *Maximum Accumulated Moisture Buffering Value* (MAMBV) representing the maximum amount of moisture buffered by a surface material in a daily moisture load cycle. The conclusion was that the differences in hygric capacity and water vapour permeability of the two materials did not lead to a significant buffering effect when a constant moisture load was applied for a long period of time (around 100 g/h for 10h). However, for a high moisture load over a short period (200.2 g/h for 2h) the gypsum board provided a greater buffering potential than the wood panelling. These results were similar to the ones obtained by Ge et al. (2014) who tested two groups of materials subjected to roughly the same moisture load: a group with high vapour permeability and low hygric capacity, and another group with low vapour permeability but high hyric capacity.

In Zhang et al. (2017), three types of finishing hygroscopic materials were tested: a porous baked clay tile, a biomass fibre wallpaper and a vermiculite board. They were installed in a test house which walls were subjected to the exterior climate. Different air change rates, loading ratios of hygroscopic materials and moisture loads were selected. The results were in adequacy with the ones from Li et al. (2012) and Yang et al. (2012): the indoor relative humidity was dampened by the hygroscopic materials, and this effect was less pronounced with a high ventilation rate.

Another approach was proposed by Labat and Woloszyn (2015). They relied on a variable occupancy scenario to simulate a realistic vapour production in a studio. Numerous activities were considered like showering, cooking, dishwashing, etc... corresponding to an average moisture production of 82 g/h. As in Woloszyn et al. (2009), they highlighted that combining a relative humidity sensitive ventilation system with highly hygroscopic materials could improve the indoor comfort by dampening the humidity.

Finally, Vereecken et al. (2011) stated that determining the moisture buffering

potential of all materials in a room is time-consuming and not realistic. They proposed a methodology based on in situ measurements. It consisted in sealing air leaks around the windows and the doors with plastic foil. A humidifier providing a cyclic moisture production was added. The experimental results were then compared with a moisture balance model and good agreement was observed.

1.1.3 Summary

The moisture buffering of materials is a well known phenomenon and has been highlighted by numerous methods at material and wall scale. However, at wall scale, most of the approaches use controlled environmental conditions. We decided to rely on a numerical methodology taking into account the following modules: the coupled heat and mass transfer in the walls, variable exterior boundary conditions, the air-conditioning system, and the modelling of the occupants' presence and activities in a realistic way. The methodology is illustrated in Figure 1.3.

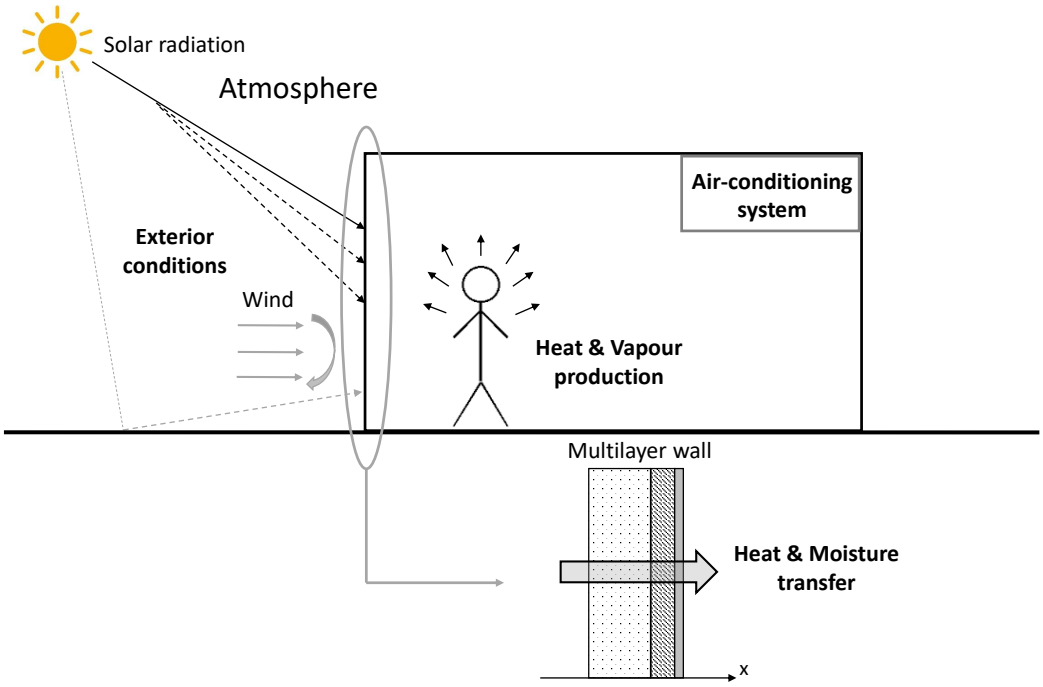

Figure 1.3 – Schematic representation of the methodology

The next sections present a literature review on two key modelling points: the coupled heat and moisture transfer in a porous material with an emphasis on moisture transfer, and the modelling of the occupants' presence and activities in buildings.

1.2 Coupled heat and moisture transfer in porous media

According to Rose (2003), the firsts attempts based on heat and moisture transfer, to understand the deterioration of building materials due to the humidity, started in the 1930s in the USA. Rose (2003) highlighted that during this era, most construction were in wood. They were then isolated using fiber-board panel, expanded mineral products (perlite and vermiculite), and mineral products (slag wool, rock wool and glass fiber). It was in the middle of the 1930s that the firsts mould growth were identified. However Teesdale (1937) defended the use of insulation as their impact on the indoor comfort and the energy consumption were non negligible. Researches on coupled heat and moisture transfer were hence needed to address this issue.

The coupled heat and mass transfer theory was introduced by Philip and De Vries (1957) and later by Luikov (1975). These investigations were not in the field of building physics but focused on soil physics, except for Glaser's researches. According to Hens (2015), Glaser published 4 articles between 1958 and 1959 on the interstitial condensation in cold store walls. His method was very popular in the USA to estimate the building response to humidity, but it did not take into account the hygroscopic behaviour of materials. The firsts numerical models, named HAM (Heat, Air and Moisture) models were developed in the beginning of the 1990s with the models MATCH (Pedersen, 1990) and WUFI (Künzel, 1995). An exhaustive state of the art can be found in Delgado et al. (2010) in which 14 open access models among more than 50 existing models are listed. A more detailed description of some of these models is available in Woloszyn and Rode (2008). This description accounts for the method used (finite differences, volumes or elements), the chosen driving potential (water vapour pressure, capillary pressure, relative humidity...), the physical phenomenon (hysteresis, liquid and/or vapour diffusion) or the simulation of a ventilation system.

An exact mathematical solution for coupled heat and mass transfer is not possible since many physical phenomenon have to be taken into account: soluble substances precipitation, crystallization/hydration of salt, diffusion of solid substances... All of these phenomena alter the material matrix, modify the shape and the diameter of the pores and change their specific surface. For building materials, these phenomena are not considered and the common assumption of all HAM model is that the material matrix is inalterable (unlike in, for example, coupled heat and mass transfer in aliments (Nicolas et al., 2014)). The material properties such as its dry density, the pore size distribution and the specific surface are invariable (Hens, 2012).

HAM models are governed by conservation equations. These are applied on a representative elementary volume (REV) under the assumption that the media is continuous.

1.2.1 Mass transport

The "mass transfer" expression referred to the transport of air, water vapour, liquid water (or other gases or liquids) and chemical compounds dissolved in the liquid. This transport can only exist if the pores of the materials are large enough for the molecules to pass. The most detrimental transport for construction materials is the humidity transport. Hens (2012) defined the humidity as "the water in the pores in two or three phases, with different chemical substances dissolved inside". These phases include the ice, the liquid and the water vapour under 0°C and liquid and water vapour above 0°C. In this section, only the liquid and vapour transport are presented. Künzel and Kiesel (1994) and Qin (2010) list the different transport mechanisms with their driving potentials (Table 1.1):

	Transport mechanism	**Driving potential**
Vapour transport	Gas diffusion	Vapour pressure
	Convection	Total pressure gradient
	Molecular transport (effusion)	Vapour transport
	Thermodiffusion (Soret effect)	Temperature
Liquid transport	Capillarity	Capillary pressure
	Thermodiffusion	Temperature
	Surface diffusion	Relative humidity
	Hydraulic flow	Total pressure gradient
	Seepage flow	Gravitation

Table 1.1 – Liquid water and water vapour transport mechanisms

Figure 1.4 (Peuhkuri, 2003) illustrates the different humidity transport mechanisms in the pores as a function of the material water content.

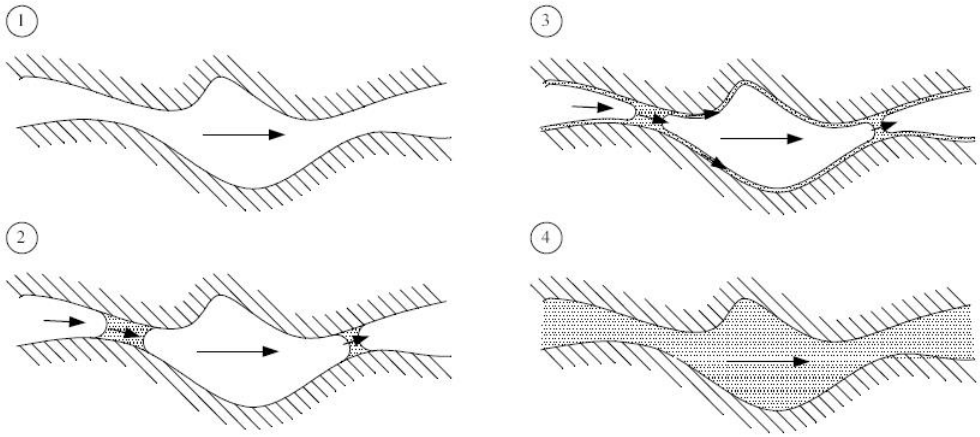

Figure 1.4 – Humidity transport mechanisms in the pores as a function of the water content (Peuhkuri, 2003)

At low relative humidity (1), only water vapour transport occurs under a vapour pressure gradient. With the increase of humidity (2), the water layer on the pores surface grows and forms liquid bridges; the transport is governed by successive condensation-evaporation. When the humidity increase even more (3), the driving potentials are the condensation-evaporation and the surface diffusion. Finally, at stage (4), only liquid water transport occurs under a capillary pressure gradient.

Mass transport in porous materials are based on water vapour and liquid water conservation equations given by Eqs. (1.6) and (1.7):

$$\frac{\partial w_v}{\partial t} = -\overrightarrow{\nabla}(\vec{g}_v) + S_v \tag{1.6}$$

$$\frac{\partial w_l}{\partial t} = -\overrightarrow{\nabla}(\vec{g}_l) + S_l \tag{1.7}$$

where w_v and w_l are the water vapour and the liquid content respectively (kg/m^3), g_v and g_l are the vapour and liquid fluxes (kg/s), S_v and S_l corresponds to the vapour and liquid sources (kg/s). The terms w_v and w_l can be added to consider the overall moisture content w (kg/m^3). By emitting that the liquid source corresponds to the water vapour condensation, meaning $S_l = -S_v$, Eq. (1.8) is deduced:

$$\frac{\partial w}{\partial t} = -\overrightarrow{\nabla}(\vec{g}_l + \vec{g}_v) \tag{1.8}$$

1.2.1.1 Humidity storage

A porous material has the ability to exchange humidity with the ambient air. Water molecules can fix themselves on the solid matrix. When the air relative

humidity increases, the mass of the material increases too: this is adsorption. In contrast, the material loses mass when the humidity decreases: this is desorption. The relative humidity Ψ is the ratio between the water vapour pressure and the saturated water vapour pressure at a given temperature, representing the maximum water vapour that the material can absorb:

$$\Psi = \frac{p_v(T)}{p_{v,sat}(T)} \tag{1.9}$$

The saturated vapour pressure is often expressed as an exponential function. Many equations coming from the analysis of experimental data are available in the literature. Figure 1.5 presents a comparison of the expressions from the British standard 5250 (British Standards Institution, 2002), the standard EN ISO 7730 (Afnor, 2005) and the ones used by Collet (2004), Berger (2014) and Peuhkuri (2003) for a temperature ranging from 0 to 50°C.

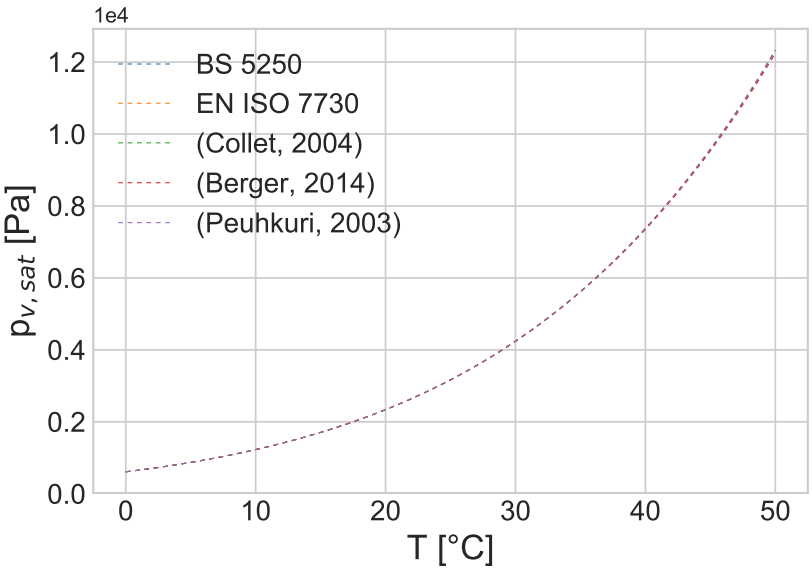

Figure 1.5 – Comparison of the saturated water vapour pressure expressions from the literature

Almost no deviations are observed between the curves. The expression from the standard EN ISO 7730 (Afnor, 2005) is selected here. Its expression is given by Eq.(1.10):

$$p_{v,sat}(T) = exp\left(16.6536 - \frac{4030.183}{T + 235}\right) \tag{1.10}$$

with T is the temperature (°C).

At microscopic scale, Künzel and Kiesel (1994) decomposed the behaviour of a

porous material during the adsorption phase in three regions (Figure 1.6).

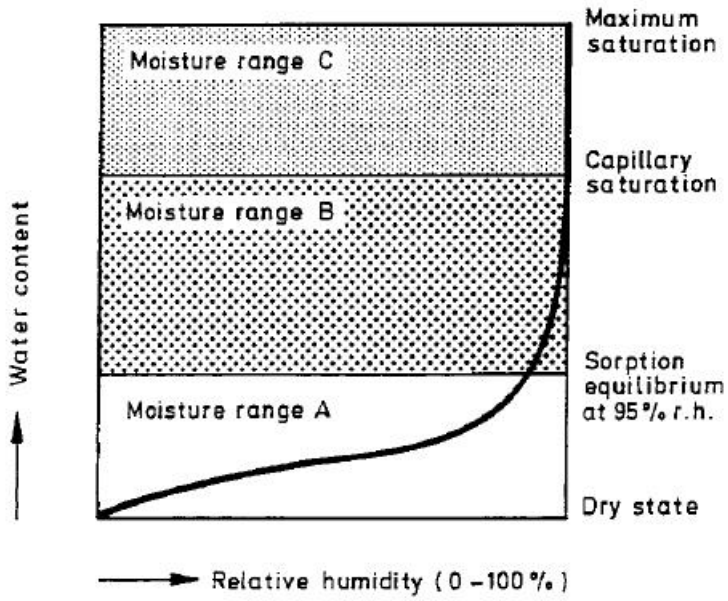

Figure 1.6 – Storage of humidity in a porous material (Künzel and Kiesel, 1994)

- Region A: hygroscopic region. When the material is subjected to low relative humidities (under 40%), water is adsorbed on the pores walls forming a single layer then a multilayer of water molecules. The capillary condensation appeared when the whole space of the pore is filled with water, hence the smaller pores are filled first. Until 90-95% of relative humidity, water is essentially transported under its vapour phase;
- Region B: super-hygroscopic region. Most of the poral space is occupied by liquid water, with small pockets transporting vapour. The material can absorbed water until it reached the capillary saturation;
- Region C: super-saturated region. If the material stays in contact with liquid water, the small pockets of air are dissolved and the material can reach the maximum saturation. Water vapour transport becomes negligible.

The curve represented in Figure 1.6 is called a sorption isotherm. It is usually measured by the saturated salt solutions technique detailed in the standard EN ISO 12571 (Afnor, 2013) . The material must be initially dried (see standard EN ISO 12570 (Afnor, 2000)). The experiment consists in subjecting a sample to relative humidity steps under constant conditions while recording its mass when steady state is reached. The International Union of Pure and Applied Chemistry (1985) (IUPAC) classifies the sorption isotherms into 6 types (Figure 1.7).

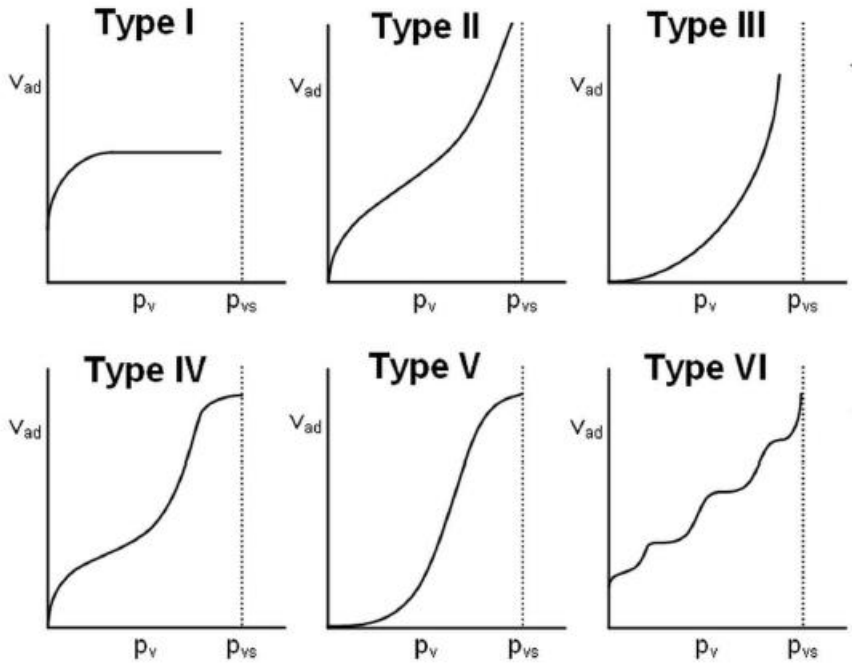

Figure 1.7 – Classification of the sorption isotherms (International Union of Pure and Applied Chemistry, 1985)

Building materials are usually characterized by a S-shape sorption isotherms corresponding to the type II in the IUPAC classification. This type is characteristic of multimolecular interactions, meaning that the adsborbed water layer thickness increases progressively (Langmuir, 1918).

In the literature, numerous models were developed to describe the sorption isotherms: Guggenheim-Anderson-DeBoer (cited by Chamoin (2013)), Brunauer-Emmet-Teller (Brunauer et al., 1940), Smith (1947), Kumaran (2009), Harkins and Jura (1944), Henderson (1952), Oswin (1946) and Langmuir (1918) among others. The equations of these models are not presented here, an exhaustive list can be find in Bui et al. (2017b). Additionally, it was highlighted that the GAB model gives the best accuracy (Labat et al., 2015; Bui et al., 2017b) for numerous building materials. Its equation is given here as it was implemented in the model developed in this work (see Chapter 2):

$$w = \frac{C_1 C_2 \Psi}{(1 - C_2\Psi)(1 - C_2\Psi + C_1 C_2 \Psi)} \cdot W_m \tag{1.11}$$

where C_1 and C_2 are fitting parameters. W_m is a physical parameter based on Langmuir (1918) formalism. It corresponds to the water content of the material when the water molecules covered the whole surface of the pores while forming a single layer of molecules.

1.2.1.2 Hysteresis

For building materials, it is common to observe a shift between the adsorption and desorption curve: this is the hysteresis. This phenomenon is illustrated in Figure 1.8) (Zhang et al., 2015).

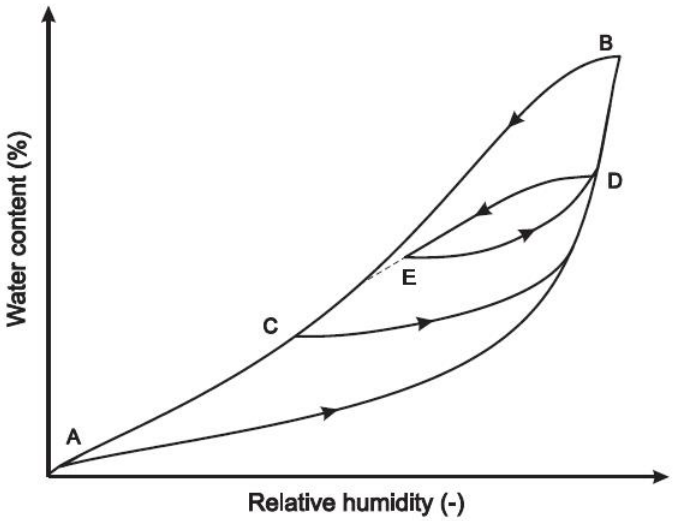

Figure 1.8 – Illustration of the hysteresis (Zhang et al., 2015)

The path from A to B corresponds to the main adsorption curve and the one from B to A to the main desorption curve. The shift does not only exist for the main curves, but also for intermediate curves. Indeed, when starting from a random point on the adsorption curve, a decrease in relative humidity before reaching the saturation point leads to a decrease of water content following an intermediate scanning curve (D-E). Similarly, an increase in relative humidity before reaching the dry state of the material lead to a water content following the path E-D.

Different modelling approaches described by numerous model exist in the literature; a state of the art done by Zhang et al. (2014) lists 10 models applied on cement materials. According to the authors, the first hysteresis models were developed after Haines (1939) work in soil science. The description of the models is not presented here, but further information can be found in Zhang et al. (2014). A physical theory of the hysteresis is presented in Mualem (1984). Additionally, Maqsoud et al. (2006) compared different hysteresis models applied to soils, and two models were compared on hemp concrete in Aït Oumeziane et al. (2014).

Influence of the hysteresis on HAM modelling

Kwiatkowski et al. (2009) affirm that only 2 among a list of 37 models take into account the hysteresis. It is usually considered that its influence on the hygrothermal behaviour of a material is rather limited.

From an experimental point of view, measuring the adsorption curve is time consuming because of the long mass stabilisation time while measuring it for building materials. Therefore, most of the authors measured only the main adsorption curve (Desta et al., 2011).

Carmeliet et al. (2005) studied the impact of the hysteresis on the relative humidity of a room with timber walls by comparing three models: one using the hysteresis, another one using the adsorption curve and the last one using the desorption curve. The simulation was done on a 2 years period and a 0.5 kg/h vapour source was added during the hours 8, 9, 13, 14, 18 and 19 each day. Figure 1.9 presents the relative humidity at the surface of the wall for five consecutive days.

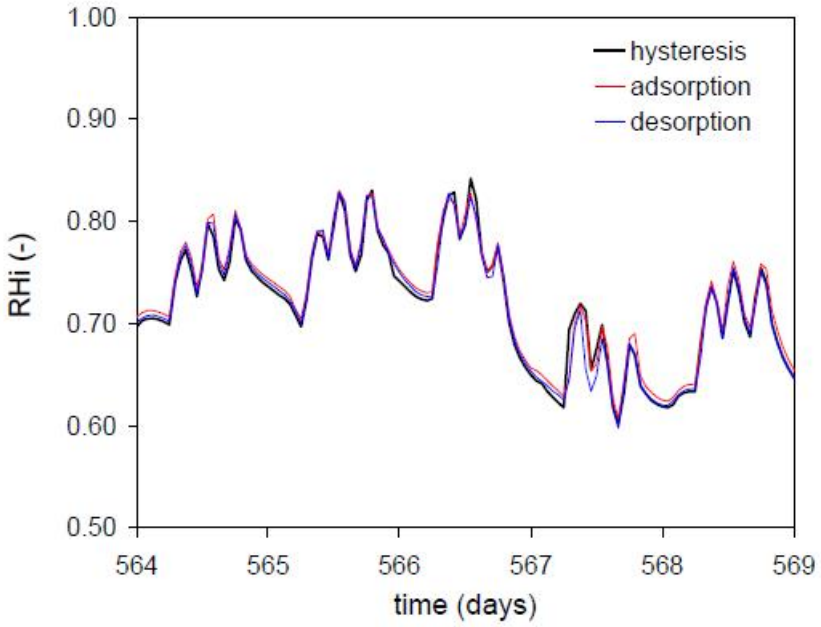

Figure 1.9 – Relative humidity calculated at the surface of a timber wall with three models: hysteresis, adsorption curve, desorption curve (Carmeliet et al., 2005)

The model taking into account only the adsorption curve gave a slightly higher relative humidity, but the difference was negligible. Carmeliet et al. (2005) explained this slight increase by the minor differences observed between the hygric capacity of the adsorption, desorption and intermediate scanning curves.

Additionally, Kwiatkowski et al. (2011) compared the water content of a room estimated by two mass transport models: one taking into account the hysteresis and another one taking into account the average water content between the adsorption and desorption curves. The simulation of a room made of gypsum board and subjected to realistic exterior conditions for 8 months led to an average difference of calculated water content of only 3.1%.

To summarise, the hysteresis has a marginal impact on the indoor air balance of a room. The moisture buffering capacity of a material is dependent on the hygric capacity corresponding to the slope of the sorption isotherm, but few deviations are observed between the adsorption and desorption curves (Carmeliet et al., 2005). It is hence safe to assume that the intermediate scanning curves would give deviations of the same order of magnitude. Therefore, the hysteresis was not taken into account in our approach.

1.2.1.3 Water vapour transport

Humid air can be assimilated as a mix of two ideal gases: dry air and water vapour. Based on the kinetic theory of gases and by neglecting the total pressure gradient, the water vapour fluxes $g_{v,diff}$ (kg/s) can be expressed as follows:

$$\vec{g}_{v,diff} = -(\delta_v \overrightarrow{\nabla} p_v + D_{v,T} \overrightarrow{\nabla} T) \tag{1.12}$$

where the terms $\delta_v \overrightarrow{\nabla} p_v$ and $D_{v,T} \overrightarrow{\nabla} T$ correspond to the Fick diffusion and the thermodiffusion respectively, and $D_{v,T}$ is the thermodiffusion coefficient $(kg/(m.s.K))$.

Thermodiffusion and effusion

When a temperature gradient is applied to the porous material, two vapour transport phenomenon occur: the thermodiffusion (or Soret effect) and the effusivity (Oumeziane, 2013). The thermodiffusion appears when the air is subjected to a temperature variation provoking the migration of the molecules from the cold areas to the hot ones. Mathematically, this phenomenon is translated by Eq. (1.13):

$$\vec{g}_{thermodiffusion} = D_{v,T} \overrightarrow{\nabla} T \tag{1.13}$$

where T is the temperature (K). The effusion is a diffusion under a concentration gradient in confined poral spaces. This phenomenon is function of the Knudsen number:

$$K_n = \frac{L_{pm}}{d} \tag{1.14}$$

where L_{pm} is the free mean path of the molecules (m) and d is the pore diameter (m). Depending of the value of the Knudsen number, three different transport phenomena may occur:

- $K_n \gg 1$ meaning $d \ll L_{pm}$: effusion (or Knudsen) transport. The number of collision of the molecules against the walls is largely superior to the number of inter-molecular collisions. The transport of the molecules is determined by

the number of collisions against the pores walls:

$$\vec{g}_{effusion} = -\frac{D_a}{K_n R_v T}\overrightarrow{\nabla} p_v \tag{1.15}$$

where R_v is the ideal gas constant of water vapour $(J/(kg.K))$;

- $K_n \ll 1$ meaning $d \gg L_{pm}$: transport by molecular diffusion. The collisions with the walls are negligible in front of the inter-molecular collisions. The flux is then given by Fick's law $(\delta_v \overrightarrow{\nabla} p_v)$;
- $K_n \approx 1$ meaning $d \approx L_{pm}$: mixed diffusion transport. The transport is determined by both the collisions with the walls and the inter-molecular collisions. It is described by Eq. (1.16):

$$\vec{g}_{mixte} = -\frac{D_a}{(1+K_n) R_v T}\overrightarrow{\nabla} p_v \tag{1.16}$$

Here, Knudsen diffusion is no taken into account as this work will not consider temperatures above 50°C, meaning that only Fick's diffusion happens. Additionally, it has been proven by numerous studies that the thermodiffusion can be neglected. Krus (1996) affirms that the thermodiffusion only contribute to 0.05% of the total water vapour pressure. This assumption was confirmed by Janssen (2011) who analysed a large amount of experimental data.

Convection

Convection is due to the humidity transport by the air flux. Its expression is given by Eq. (1.17) (Hens, 2015):

$$\vec{g}_{v,conv} = x_v \vec{g}_a \tag{1.17}$$

where $\vec{g}_a$ is the air flux, x_v is the mass ratio of the vapour given by Eq. (1.18):

$$x_v = \frac{m_v}{m_a} = \frac{\rho_v}{\rho_a} = \frac{M_v}{M_a} \cdot \frac{p_v}{p_{atm} - p_v} \tag{1.18}$$

where m is the mass (kg), M is the molar mass (kg/mol), subscripts v, a, and atm stand for *vapour*, *air* and *atmosphere* respectively. This term will not be taken into account in this study as it is assumed that the air transfer is negligible (no variation of the total pressure). The cracks in the walls or the defaults at the interfaces could provoke a variation of total pressure but they are not considered here (Schijndel, 2007).

1.2.1.4 Liquid water transport

Liquid water transport starts to occur when a continuous liquid phase is formed in the material. This phase is initiated when a critical water content w_{cr} is reached. Starting this value, vapour transport decreases progressively with the increase of water content of the material until they disappear at the saturation (Figure 1.10). The value of w_{cr} depends on the characteristics of the porous media (open porosity, pores size, tortuosity,...). Philip and De Vries (1957) stated that w_{cr} corresponds to a humidity of 60%, based on Carman (1951) work.

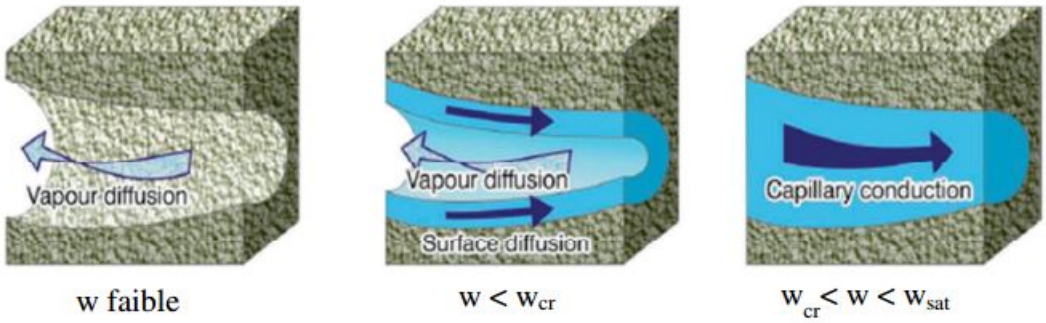

Figure 1.10 – Illustration of the liquid water transport (Evrard, 2008)

According to Scheffler and Plagge (2009), two approaches can be used to define the liquid transport: the capillarity driven by the capillary pressure and with Fick's law driven by the water content. Only the capillarity approach is developed here.

Capillarity

Liquid transport is based on Darcy's law (Darcy, 1856) and is mathematically translated by Eq. (1.19):

$$\vec{g}_{l,diff} = \delta_l \overrightarrow{\nabla} p_c \tag{1.19}$$

where δ_l is the liquid permeability ($kg/(m.s.Pa)$) and p_c the capillary pressure (Pa). At pore scale, when the relative humidity increases, this phenomenon is described by the capillary condensation during which a liquid bridge is formed. The liquid water is then in equilibrium with the ambient air. This is described by Gibbs' law:

$$p_c = \rho_l \cdot R_v \cdot T \cdot ln(\Psi) \tag{1.20}$$

where ρ_l is the liquid water density (kg/m^3).

Surface diffusion

Beyond the polymolecular adsoprtion, the interacting forces between the solid and the adsorbed water molecules decrease, permitting the mobility of the latter:

this is the surface diffusion which happens between the saturation of the pores (Krus, 1996). Brunauer et al. (1938) expressed this movement with a relative humidity gradient whereas Philip and De Vries (1957) used a water content gradient:

$$\begin{aligned} \vec{g}_{l,surf} &= -D_{\Psi,surf} \overrightarrow{\nabla} \Psi \\ or \quad &- D_{l,surf} \overrightarrow{\nabla} w \end{aligned} \tag{1.21}$$

where $D_{l,surf}$ is the surface diffusion coefficient (m^2/s) and $D_{\Psi,surf}$ is the liquid conduction ($kg/(m.s)$). As it is difficult to differentiate the capillarity from the surface diffusion, both phenomenon are merged, meaning that the liquid transport is described only by Darcy's law.

1.2.2 Heat transfer mechanisms

Heat transfer in porous media composed of a solid and liquid phases are described by numerous fluxes:

- Conduction in the solid phase under a temperature gradient;
- Radiation between the pores walls due to the electromagnetic waves;
- Evaporation-condensation of the water (latent heat);
- Enthalpy transport related to the water vapour diffusion under a vapour pressure gradient (sensible heat).

Conduction happens under a temperature gradient provoking the movement of gas molecules which may collide with each other. The heat transfer direction is from the hottest molecule to the coolest one. This phenomenon is described by Fourier's law (Eq.(1.22)):

$$\vec{q}_{h,cond} = -k_{mat} \cdot \overrightarrow{\nabla} T \tag{1.22}$$

where k_{mat} is the thermal conductivity of the material ($W/(m.K)$). This law implies that the conductive heat transfer is proportional to the temperature gradient. The thermal conductivity can be expressed as a function of the material water content and temperature. However, the temperature dependence can be neglected for the range of temperature which buildings are subjected to (Scheffler, 2008).

Radiative heat transfer is the energy emitted by a matter that has a non null temperature. The radiative energy is transported by electromagnetic waves. The radiative flux between two bodies is expressed as follows:

$$q_{h,ray} = \epsilon \sigma T^4 \tag{1.23}$$

where ϵ is the emissivity and σ is the Stefan-Boltzmann's constant equals to $5.67 \cdot$

$10^{-8}W/(m^2.K^4)$. The radiative heat transfer is usually incorporated to an equivalent thermal conductivity determined by experiments at macroscopic scale.

1.2.3 Driving potentials

For heat transfer, the temperature is the only driving potential. However, for mass transfer, many potentials can be used: the capillary pressure (Janssen et al., 2007; Li et al., 2009), the logarithm of the capillary pressure (Schellen et al., 2008), the water content (Künzel and Kiesel, 1994), the water vapour pressure (Janssens, 2001), the relative humidity (Tariku et al., 2010), the mass ratio (Steeman et al., 2009) can be quoted among others.

1.2.3.1 Water content

Philip and De Vries (1957) and Luikov (1975) models use the water content as driving potential but they present three main drawbacks. Firstly, the water content is discontinued at the interface between materials as highlighted by Freitas et al. (1996) and by Tariku et al. (2010) on a multilayer wall (Figure 1.11).

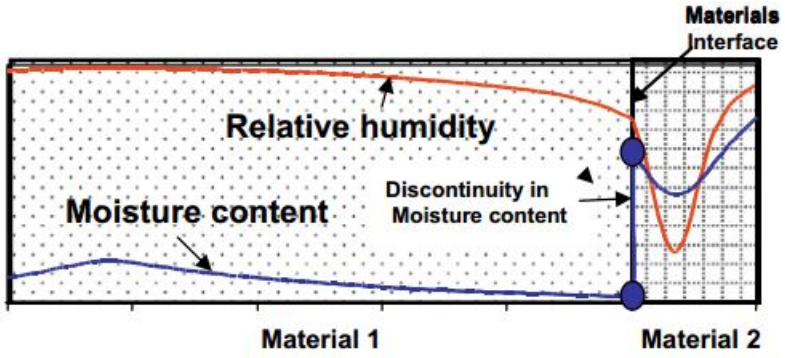

Figure 1.11 – Illustration of the discontinuity of water content at the interface between two materials (Tariku et al., 2010)

Secondly, heat and humidity diffusion coefficients depend upon each other which makes it difficult to experimentally measured them. Finally, from a mathematical point of view, Philip and De Vries (1957) and Luikov (1975) equations are difficult to manipulate. However, according to Mendes and Philippi (2005), it is the most interesting driving potential because its physical interpretation is relatively easy. It also seems to limit the hysteresis impact. To avoid the discontinuity at the interface between materials, Mendes and Philippi (2005) propose to switch to the capillary pressure at the interface, meaning to change the driving potential.

1.2.3.2 Water vapour pressure

A HAM model at building scale using the vapour pressure as driving potential was developed by Kalagasidis (2004) (HAM-Tools) and used by Piot (2009) and Labat (2012). This model was then validated with the IEA ECBS (Energy Conservation Buildings and Community System) Annex 41 "Whole Building Heat, Air and Moisture Response" benchmark (Kalagasidis et al., 2008).

This driving potential is particularly interesting as it can be defined as a "true" potential as it comes directly from Fick's law. Therefore, an advantage of using the vapour pressure is that both the mass and energy balance equations need limited mathematical adjustments to be expressed as a function of this potential. However, Williams Portal (2011) observed that the water vapour pressure does not have a good numerical convergence under steep boundary conditions variations. This can be explained by the fact that heat transfer is much faster than humidity transfer (with a 5×10^4 factor). As a consequence, Williams Portal (2011) suggests to use the relative humidity due to its lower variations.

1.2.3.3 Relative humidity

The relative humidity is used in one of the commercialized HAM model (WUFI (Künzel and Kiesel, 1994)). Künzel (1995) justifies its use with the fact that the relative humidity is easily measurable from an experimental standpoint. Additionally, Tariku et al. (2010) proved its continuity at the interface between materials. Alternatively Steeman et al. (2009) used the specific humidity defined as the mass of water over the mass of humid air. However, Van Belleghem et al. (2014) affirms that this choice is only applicable if liquid water transfer does not occur. As the specific humidity is directly linked to the relative humidity, this limitation is also applied to the latter.

1.2.3.4 Capillary pressure

As the water vapour pressure, the capillary pressure is also defined as a true potential by Janssen et al. (2007) and Hens (2015) because it comes directly from Darcy's law in the mass conservation equation. This potential was also used in the software HAM-BE developed by Li et al. (2009). Moreover, its use as a driving potential was deemed as a valid approach to describe the liquid transfer by Carmeliet et al. (2004). According to Janssen (2011), the capillary pressure is the potential performing the best numerically — in terms of accuracy and number of iterations — with the relative humidity on the whole range of relative humidity.

1.2.3.5 Logarithm of the capillary pressure

The logarithm of the capillary pressure was used in van Schijndel (2011) and Schellen et al. (2008) models. Originally, this potential was chosen to avoid the variations of capillary pressure between the dry and humid state of the materials. Both models were validated with the HAMSTAD (Heat, Air and Moisture STandarDization) benchmark (C-E. Hagentoft, 2004). However, Janssen (2011) showed that the logarithm of the capillary pressure suffers from a non-linearity of water contents close to saturation.

1.2.3.6 Choice of the driving potential

This literature review led to extract the relative humidity and the capillary pressure as the most performing driving potential. This conclusion is also in accordance with Janssen (2011) state of the art. His study compared the relative humidity, the capillary pressure and the logarithm of the capillary pressure. In the hygroscopic zone, the logarithm of the capillary pressure converged with a lower number of iteration than the capillary pressure. However, due to the non-linearity of this potential at high relative humidities, it is less interesting than the other two. Compared to the relative humidity, the capillary pressure is more straightforward to use since it intervenes directly in Darcy's law.

1.2.4 Summary

This section covered the heat and moisture transport mechanisms in a porous material. For modelling purposes, the major assumption are reminded here:

- The hysteresis is not taken into account;
- No air transfer ($\vec{g}_a = \vec{0}$);
- The vapour transfer relies on Fick's Law (no Knudsen diffusion);
- The thermodiffusion is neglected;
- The surface diffusion is merged with the capillary conduction.

Under these assumptions, the vapour transfer described by Eqs. (1.12) and Eq. (1.17), and the liquid transfer described by Eqs. (1.19) and (1.21) can be simplified as follows:

$$\vec{g}_v = -\delta_v \overrightarrow{\nabla} p_v \tag{1.24}$$

$$\vec{g}_l = \delta_l \overrightarrow{\nabla} p_c \tag{1.25}$$

Injecting Eqs. (1.24) and (1.25) in Eq. (1.8) yields:

$$\frac{\partial w}{\partial t} = -\overrightarrow{\nabla}\left(\delta_l \overrightarrow{\nabla} p_c - \delta_v \overrightarrow{\nabla} p_v\right) \tag{1.26}$$

As the driving potential selected for mass transport is the capillary pressure, Eq. (1.26) has to be modified to be expressed only as a function of the temperature and the capillary pressure. This development is presented in Chapter 2.

1.3 Metabolic heat and vapour sources: occupants' presence and activities in buildings

1.3.1 Introduction

In buildings, modelling the occupants' presence and activities is crucial because they not only generate heat, vapour, and pollutants, they also interact with their environment, greatly influencing the indoor air ambience. Their interactions with a building can be decomposed in several groups as illustrated by Robinson (2006) (Figure 1.12).

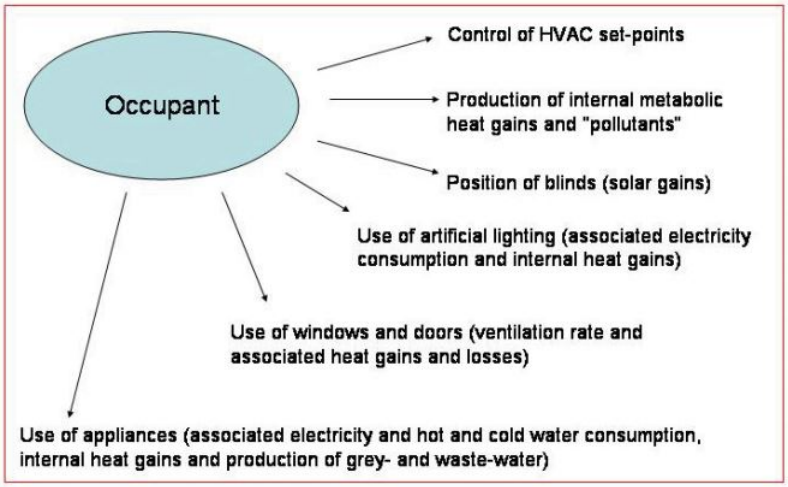

Figure 1.12 – Occupants' interactions with their environment (Robinson, 2006)

1.3.2 Modelling approaches

A wide range of approaches can be found in the literature to model the occupants' presence and activities. In the social sciences field, the agent-based modelling based on comfort is one of them. According to Macal and North (2010), an agent-based model is structured by a population of agents defined by attributes and behaviour,

a number of rules governing the relationships and the interactions between agents, and an environment with which the agents interact. This approach has been used by Kashif et al. (2011) to estimate the impact of the occupants on the energy consumption of a building. An agent has his own physiological and psychological characteristics and acts in accordance with other agents after a deliberation. For example, if an agent feels "too cold" he might wish to switch on the heating system. First he will ask his neighbours and if they agree after voting, the heating system is switched on. Obvious limitations comes from these models:

- This approach is theoretical and is not supported by experimental data;
- Comfort is specific to the physiological state of each agent. Hence, a difficulty lies in defining when an agent feels "too cold" and when he feels "cold enough" to turn on the heating system for example.

The agent-based approach is specific to social sciences field. To the best of our knowledge, only the platform No-MASS (Chapman et al., 2018) includes this approach in the energy performance field. Usually, the modelling of the occupants' presence and activities can be classified into three main groups:

- Constant indoor sources;
- Deterministic representation;
- Stochastic approach.

The most simple approach is to assume that the occupants are generating constant heat and water vapour throughout the day. This is exemplified by Hutcheon (1955) who used a constant production of 7.7 kg/day plus 1 kg/day on wash day. An other example can be found in TenWolde and Walker (2001), in which the average (on 4 houses) daily moisture release varied from 7.2 kg/day to 14.4 kg/day depending on the number of adults and children. Walker and Sherman (2007) used a constant production rate equal to 270 g/h for a family of four, after highlighting that this value was representative by reviewing 9 studies in the literature.

Still, the most common approach is the use of a deterministic scenario, meaning that the occupants are present at fixed hours every day. This scenario is widely used in the energy performance field as most of the building simulation tools rely on it: EnergyPlus (Crawkey et al., 2001) and ESP-r (Clarke, 2001) can be quoted among others. Other examples include the one in Künzel et al. (2005) who used a moisture production rate of 0.5 $g/(m^3.h)$ with peaks in the morning and the evening, i.e 8 $g/(m^3.h)$ from 6:00 to 8:00 am and 4 $g/(m^3.h)$ from 4:00 to 10:00 pm every day. Similarly, in Qin et al. (2011) an occupant was simulated at night in a residential

test house from 8:00 pm to 8:00 am with a metabolic heat gain equal to 500 W and a moisture production rate of 0.5 $g/(m^3.h)$.

While convenient to model, both of these scenarios differ widely from the occupants' real behaviour. Gill et al. (2010) showed that the occupants planned behaviour accounted for a variation 51% in heating demand between dwellings in UK. This conclusion was in accordance with the one from Seligman et al. (1978) who studied 28 identical houses. The deviations related to the diversity of behaviour between the occupants could double the energy demand of dwellings. The same factor was found by Maier et al. (2009) after comparing 22 identical residential houses in Germany. The discrepancies between the observed and modelled data are especially pronounced in residential houses due to the wide variety of activities performed by the occupants, as illustrated in Figure 1.13 (Wilke, 2013).

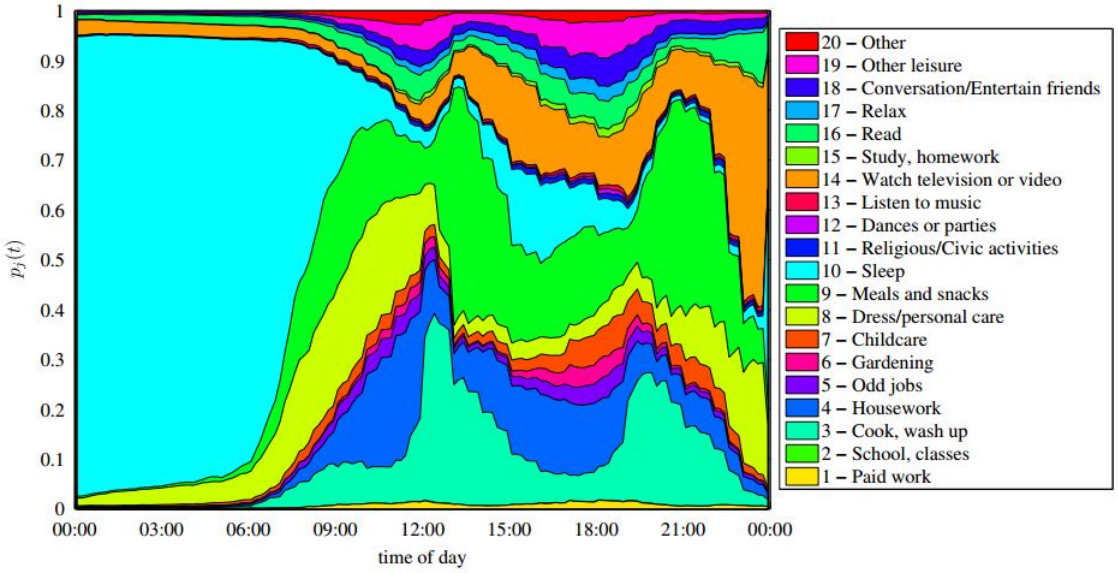

Figure 1.13 – Probability to perform an activity in dwellings (Wilke, 2013)

While not having the same amount of activities in offices, the occupants still interact with their environment: use of lighting, windows, blinds, ... influencing the indoor ambience.

Consequently, another alternative is to rely on a stochastic approach which is presented in next section. This is an emerging approach in the energy performance field but it is not yet favoured in the hygrothermal field.

1.3.3 Stochastic modelling of the occupants presence and activities

As defined by Page (2007), a stochastic (or probabilistic) process is "a variable that evolves with time in such a way that the values it takes on cannot be determined at each time step but only given a probability of appearing". Simply put, the estimation of an occupant state at a given time is not binary (absent or present) but is rather translated as "might be present with a probability of X%".

In the energy performance field, one of the first attempt to develop a stochastic model was proposed by Hunt (1980). His model focused on the use of lighting, based on field study data. He assumed that the lighting was switched on at the arrival of the occupants and switched off at their departure during weekdays. What differs from a deterministic model is that the switch on and switch off events were based on a probability function. Then, Newsham et al. (1995) improved Hunt (1980) model by taking into consideration a minimum illuminance level of 150 lux as a condition to switch off the lighting. Reinhart (2004) further adapted this model to develop the Lightswitch-2002 model. Real occupancy data with a 5 minutes time step were implemented in this model.

Later, Wang et al. (2011) used a Markov chain method to simulate the stochastic movement process between each zone of a building without any limitations on the number of occupants and zones. Their research focused on office buildings with the assumption that the occupants' movements had a Markovian processed. This was partially supported by experimental data from Wang et al. (2005). Chang and Hong (2013) instrumented a three floors office building with a total of 200 lighting-switch sensors. Sensors placed above the workstations detected the occupants movements and switched the lights on if they are occupied. After data collections, Chang and Hong (2013) did a statistical analysis on the occupancy status to provide it in energy models. More recently, Feng et al. (2015) regrouped 3 different models in an algorithm: occupancy scenarios from Chang and Hong (2013), transitions of occupants between rooms from Wang et al. (2011) and number of occupants in a room from Page et al. (2008). The latter is based on an inhomogeneous Markov process to calculate the probability of presence (or absence) of an occupant.

Stochastic models can also be applied to predict the occupants activities in building. Widen et al. (2015) proposed a modelling methodology for the use of electrical appliances and hot water based on Swedish time-use survey data. Wilke (2013) relied on a multinational time use database to developed a time-dependent Markov chain model which predicts the transition from one activity to another, while considering the duration of each activity. The main drawback of his model is that it

is computationally expensive. Finally Jaboob (2015) tested numerous modelling strategies (also based on time-use survey data) in order to find the one giving the better compromise between accuracy and calculation expense.

More recently, Chapman et al. (2017) regrouped empirically validated data, namely Page et al. (2008) presence model in offices based on data recorded by the instrumentation of an office building, and Jaboob (2015) activity model validated with time use survey data. He also added several other models characterising the interaction of the occupants with their environment: windows interactions model from Haldi and Robinson (2009), shading interactions (Haldi and Robinson, 2010), and lighting interactions with the Ligtswitch-2002 model (Reinhart, 2004). To evaluate the occupants' impact on the energy performance of buildings, No-MASS was coupled with the building performance simulation software EnergyPlus (Crawkey et al., 2001). The same approach was also proposed by Darakdjian et al. (2017).

1.3.4 Moisture scenarios used to estimate the walls moisture buffering

While the stochastic approach has been recently proposed in the energy performance field, it is not commonly used for hygrothermal modelling in order to estimate the walls moisture buffering effect. As presented in Section 1.1, many researches highlighted the walls moisture buffering, but most approaches relied on control environmental conditions by using constant and cyclic scenario to simulate the indoor moisture sources. Table 1.2 summarises the different scenarios from the studies presented in Section 1.1. Note that this table does not provide a state of the art on all of the existing hygrothermal methodologies accounting for the indoor moisture sources, but only on the ones focusing on the walls moisture buffering.

Authors	Methodology	Moisture production	
		Scenario	Production (g/h)
Hameury (2005)	Num.	Constant	[60;120]
Woloszyn et al. (2009)	Exp.	Cyclic	[200;400]
Yoshino et al. (2009)	Exp. and Num.	Constant	[0;20]
Vereecken et al. (2011)	Exp. and Num.	Cyclic	[0;57]
Li et al. (2012)	Exp.	Constant	[25;58]
Yang et al. (2012)	Exp.	Cyclic	[55.5;200.2]
Labat and Woloszyn (2015)	Num.	Variable	82 (average)

Table 1.2 – Moisture production scenarios extracted from the literature

First, this table highlights a non-consensus on the vapour production due to the occupants' presence and activities. Moreover, except for Labat and Woloszyn (2015), all of the other studies used a cyclic or constant moisture scenario. Labat and Woloszyn (2015) focused on a room configuration corresponding to a studio in which indoor moisture loads depended on the activity performed, and could attain as much as 2000 g/h. For tertiary buildings, such moisture productions are not reached. While highlighting the walls moisture buffering, the other studies did not estimate it under realistic indoor conditions.

1.4 Summary and research objectives

The walls moisture buffering capacity could have a significant impact on the indoor relative humidity. The indoor air humidity is strongly influenced by its interaction with the walls, the ventilation and the indoor moisture sources. This chapter presented the fundamental phenomena and their corresponding equations describing heat and moisture transfer through porous materials. The second part covered the different strategies applied to model the occupants' presence and activities in buildings.

The coupled heat and moisture transfer regroup complex phenomena and the major assumptions done in our research were detailed.

Various approaches to model the occupants presence and activities exist and it was shown that a stochastic method could lead to more consistent results. This approach has been recently used in the energy performance field. However, applying this method in the hygrothermal field is questioned as few studies relied on it.

Consequently, this work aims at fulfilling the following objectives:

- Developing a numerical hygrothermal model taking into account the coupled heat and moisture transfer in the walls and the indoor sources;
- Assessing the impact of the occupancy scenario on indoor air balance;
- Proposing an estimation of the walls moisture buffering effect.

The different modules of the numerical hygrothermal model at room scale are detailed in Chapter 2. Chapter 3 presents a case study to estimate the occupancy scenario impact on indoor air balance. Finally, Chapter 4 proposes an estimation of the walls moisture buffering of rooms exposed to different climate.

Chapter 2

Development of a hygrothermal model at room scale

Contents

2.1 Methodology

This chapter aims at presenting the numerical hygrothermal model developed in accordance with the methodology described in Figure 1.3. The three different modules of the model are detailed, namely: the coupled heat and moisture transfer at wall scale (Section 2.3), the modelling of the air-conditioning system (Section 2.4), and the modelling of the occupants' presence and activities (Section 2.5).

The keystone lies in the indoor air conditions as it results from the heat and vapour fluxes exchanged with every modules. The indoor air balance equations are presented in Section 2.2.

To assess the hygrothermal performance of a room, performance indicators related to each module of the model were defined: the air-conditioning system energy demand, the indoor hygric comfort, and the moisture related risks in the walls (Section 2.7).

2.2 Indoor air balance equations

The temperature and water vapour pressure of a room are described by the mass and energy balance equations on the indoor air. The model presented in this section assumed that the temperature and the water vapour pressure were uniform within the entire volume of the room (Figure 2.1)

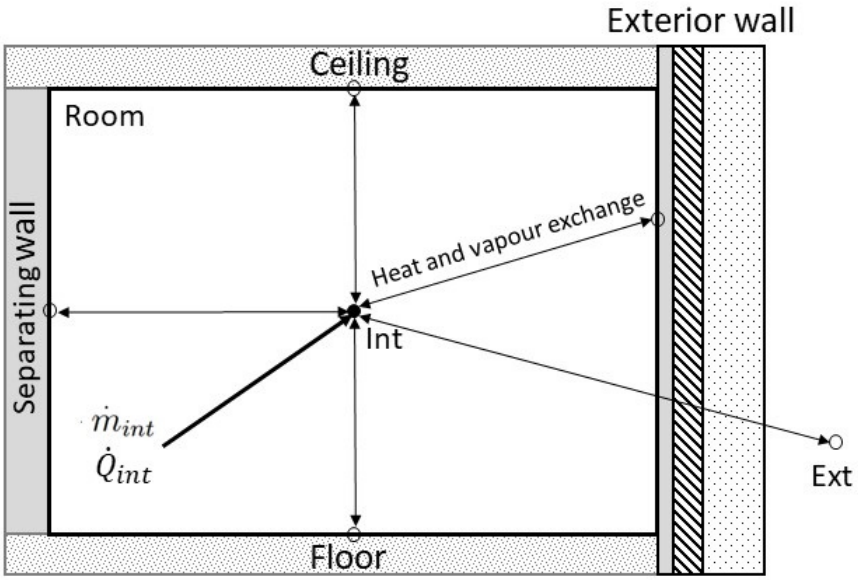

Figure 2.1 – Illustration of the exchanges with the indoor air

Mass conservation equation at room scale is given by Eq. (2.1):

$$\frac{R_a}{R_v} \cdot \frac{\rho_a V p_{atm}}{(p_{atm} - p_{v,int})^2} \frac{\partial p_{v,int}}{\partial t} = \sum_i \dot{m}_i = \dot{m}_{walls} + \dot{m}_{ventil} + \dot{m}_{int} \tag{2.1}$$

where V is the volume of the room (m^3) subscripts a, v and int stand for *air*, *vapour* and *interior* respectively, $\dot{m}_{walls}$ is the mass flow rate with the walls (kg/s), $\dot{m}_{ventil}$ is the mass flow rate due to the ventilation (kg/s) and $\dot{m}_{int}$ is the indoor vapour source/sink term (kg/s). The development of the right hand side of Eq. (2.1) is given by Eq. (2.2):

$$\begin{aligned} \dot{m}_{walls} &= \sum_j A_j h_{m,int} (p_{v,is,j} - p_{v,int}) \\ \dot{m}_{ventil} &= \frac{R_a}{R_v} \cdot \rho_a n V \left(\frac{p_{v,ext}}{p_{atm} - p_{v,ext}} - \frac{p_{v,int}}{p_{atm} - p_{v,int}} \right) \end{aligned} \tag{2.2}$$

where A_j is the surface of the wall j (m^2), h_m is the convective mass transfer coefficient ($kg/(m^2.s.Pa)$), n is the air change rate due to the ventilation (s^{-1}), and subscripts is and ext stand for *interior surface* and *exterior* respectively.

Similarly to the mass balance equation, the energy balance is given by Eq. (2.3). It accounts for the latent contribution:

$$\begin{aligned} &\rho_a V (c_{p,a} + \frac{R_a}{R_v} \cdot \frac{p_{v,int}}{p_{atm} - p_{v,int}} c_{p,v}) \frac{\partial T_{int}}{\partial t} \\ &= \dot{Q}_{walls} + \dot{Q}_{ventil} + \dot{Q}_{int} + (c_{p,v} T + L_v) \sum_i \dot{m}_i \end{aligned} \tag{2.3}$$

where c_p is the heat capacity ($J/(kg.K)$), $\dot{Q}_{walls}$ is the convective heat exchange with the walls (W), $\dot{Q}_{ventil}$ is the heat exchange with the exterior environment due to the ventilation (W), $\dot{Q}_{int}$ in the indoor heat source/sink term (W) and L_v is the latent heat of vaporization (J/kg). Eq. (2.4) details the right hand side of Eq. (2.3):

$$\begin{aligned} \dot{Q}_{walls} &= \sum_j A_j h_{h,int} (T_{is,j} - T_{int}) \\ \dot{Q}_{ventil} &= n V \rho_a c_{p,a} (T_{ext} - T_{int}) \end{aligned} \tag{2.4}$$

where h_h is the convective heat transfer coefficient ($W/(m^2.K)$). The exchanges between the indoor air and the walls, characterized by $\dot{m}_{walls}$ and $\dot{Q}_{walls}$, depend on the hygrothermal transfer through the walls. Hence, the coupled heat and moisture transfer at wall scale must be studied.

2.3 Coupled heat and moisture transfer at wall scale

2.3.1 Governing equations

Transfer in porous media is governed by mass and energy conservation equations. Heat transfer is driven by the temperature difference, and in this research case, mass transfer is driven by the capillary pressure difference (see Chapter 1). The governing equations presented in this section are the ones from Lorente (2017) and Seng et al. (2017). The demonstration is given below.

2.3.1.1 Mass conservation equation

As presented in Chapter 1, the mass conservation equation accounts for the liquid water and water vapour transfer described by Darcy's and Fick's law respectively (Eq. (1.26)). Eq. (1.26) must be expressed with only the temperature and capillary pressure as driving potentials. The capillary pressure is related to the relative humidity thanks to Gibbs' law given by Eq. (1.20), and expressed as a function of the vapour pressure through the definition of the relative humidity (see Eq. (1.9)).

By differentiating Eq. (1.9) and after some mathematics, the water vapour pressure can be expressed as a function of the relative humidity and the temperature:

$$\overrightarrow{\nabla} p_v = \Psi p_{v,sat} \overrightarrow{\nabla} ln(\Psi) + \Psi \frac{p_{v,sat}}{dT} \overrightarrow{\nabla} T \tag{2.5}$$

The logarithm of the relative humidity is expressed as a function of the temperature and capillary pressure gradients by differentiating Gibbs' law (given by Eq. (1.20)):

$$\overrightarrow{\nabla} ln(\Psi) = \frac{-1}{\rho_l R_v T^2} \left(T \overrightarrow{\nabla} p_c - p_c \overrightarrow{\nabla} T \right) \tag{2.6}$$

Finally combining Eqs. (2.5) and (2.6) and injecting them in Eq. (1.26), the mass conservation equation, expressed only with the temperature and the capillary pressure as driving potentials, is deduced:

$$\frac{\partial w}{\partial p_c} \cdot \frac{\partial p_c}{\partial t} = -\overrightarrow{\nabla} \left[\left(\delta_l + \delta_v \frac{\rho_v}{\rho_l} \right) \overrightarrow{\nabla} p_c - \delta_v \left(\Psi \frac{\partial p_{v,sat}}{\partial T} - p_v \frac{ln\Psi}{T} \right) \overrightarrow{\nabla} T \right] \tag{2.7}$$

2.3.1.2 Energy conservation equation

The energy conservation equation is governed by the first law of thermodynamics stating that the rate of energy accumulated within the control volume is equal to the net heat transfer of energy by conduction plus the net transfer of energy by fluid

flow, assuming no internal energy generation and no work transfer from the element to the environment (Bejan, 2013). Consequently, the energy conservation equation is described by Eq. (2.8):

$$\frac{\partial}{\partial t}\left(\rho_s e_s + \sum_i w_i e_i\right) + \sum_i \overrightarrow{V_i}\overrightarrow{\nabla}(w_i e_i) = -\overrightarrow{\nabla}\overrightarrow{q}'' \tag{2.8}$$

where the e is the specific internal energy (J) subscript s stands for solid, $i = v$ for vapour and $i = l$ for liquid, $\overrightarrow{V}$ is the velocity vector in the 3D Cartesian frame (which components are u, v and w towards the x, y and z axis respectively), and $\overrightarrow{q}''$ is the the heat transfer rate by conduction. For any component j:

$$\frac{\partial}{\partial t}(w_j e_j) + \sum_i \overrightarrow{\nabla}(w_i e_i) = w_j\left(\frac{\partial e_j}{\partial t} + \overrightarrow{V_j}\overrightarrow{\nabla} e_j\right) + e_j\left(\frac{\partial w_j}{\partial t} + \overrightarrow{\nabla}(w_j\overrightarrow{V_j})\right) \tag{2.9}$$

The last term between brackets corresponds to the continuity equation which is equal to the source term. Hence, Eq. (2.8) becomes:

$$\rho_s\frac{\partial e_s}{\partial t} + \sum_i w_i\frac{\partial e_i}{\partial t} = -\overrightarrow{\nabla}\overrightarrow{q}'' - \sum_i w_i\overrightarrow{V_i}\overrightarrow{\nabla} e_i - \sum_i e_i S_i \tag{2.10}$$

where $w_i V_i$ is the mass flow rate of the component i and S is the source term. The specific internal energy is related to the specific enthalpy through $e = h - p/\rho$ and in a general case without boundary displacement:

$$\frac{\partial e}{\partial t} = \frac{\partial h}{\partial t} - \frac{1}{\rho}\frac{\partial p}{\partial t} + \frac{p}{\rho^2}\frac{\partial \rho}{\partial t} \tag{2.11}$$

After some mathematics:

$$\frac{\partial e}{\partial t} = c_p\frac{\partial T}{\partial t} - \beta T\frac{\partial p}{\partial t} + \frac{p}{\rho^2} + \frac{\partial \rho}{\partial t} \tag{2.12}$$

where β is the thermal expansion coefficient $(1/K)$. It is assumed that the compressibility effects are negligible for water vapour as ideal gas, and that liquid water is incompressible. Therefore:

$$\frac{\partial e_i}{\partial t} = c_{p,i}\frac{\partial T}{\partial t} \tag{2.13}$$

$$\overrightarrow{\nabla} e_i = c_{p,i}\overrightarrow{\nabla} T \tag{2.14}$$

And:

$$\sum_i e_i S_i = [(c_{p,l} - c_{p,v})T - L_v]S_l \tag{2.15}$$

Because $S_v = -S_l$ here, L_v (J/kg) is the latent heat of vaporisation which comes from the definition of the vapour enthalpy at a reference state. Also, according to

Fourrier's law, heat transfer by conduction can be expressed as a function of the apparent thermal conductivity of the porous material, given by Eq. (1.22).

Injecting all of the above equations in Eq. (2.8) leads finally to:

$$\left(\rho_s c_s + \sum_i w_i c_{p,i}\right) \frac{\partial T}{\partial t} = k_{mat} \overrightarrow{\nabla}^2 T - \sum_i w_i \overrightarrow{V_i} c_{p,i} \overrightarrow{\nabla} T - [(c_{p,l} - c_{p,v})T - L_v]S_l \tag{2.16}$$

The liquid water content can be expressed as a function of the moisture content w and the solid content w_s:

$$w_s = \rho_s \left[1 - \frac{w}{\rho_v} + w_l \left(\frac{1}{\rho_v} - \frac{1}{\rho_l}\right)\right] \tag{2.17}$$

The source term is then obtained by writing the liquid conservation leading to:

$$\left(\frac{1}{1 - \frac{\rho_v}{\rho_l}}\right) \frac{\partial w}{\partial p_c} \frac{\partial p_c}{\partial t} = -\overrightarrow{\nabla}(\delta_l \overrightarrow{\nabla} p_c) + S_l \tag{2.18}$$

2.3.1.3 Summary

The coupled heat and moisture transfer model is characterized by Eqs. (2.7), (2.16) and (2.18). These equations are given below for a one dimensional case (towards the x axis):

$$\frac{\partial w}{\partial p_c} \cdot \frac{\partial p_c}{\partial t} = -\frac{\partial}{\partial x}\left[\left(\delta_l + \delta_v \frac{\rho_v}{\rho_l}\right) \frac{\partial p_c}{\partial x} - \delta_v \left(\Psi \frac{\partial p_{v,sat}}{\partial T} - p_v \frac{ln\Psi}{T}\right) \frac{\partial T}{\partial x}\right]$$

$$\left(\rho_s c_s + \sum_i w_i c_{p,i}\right) \frac{\partial T}{\partial t} = k_{mat} \frac{\partial^2 T}{\partial x^2} - \sum_i w_i u_i c_{p,i} \frac{\partial T}{\partial x} - [(c_{p,l} - c_{p,v})T - L_v]S_l$$

$$\left(\frac{1}{1 - \frac{\rho_v}{\rho_l}}\right) \frac{\partial w}{\partial p_c} \frac{\partial p_c}{\partial t} = -\frac{\partial}{\partial x}(\delta_l \frac{\partial p_c}{\partial x}) + S_l$$

This set of equations is coupled and non-linear, and must be solved with numerical methods. For one dimensional problems, finite volumes and finite elements methods lead to the same discretised equations than the ones obtained with the finite difference method. Therefore, the formalism of the latter was chosen. Among the finite difference method, two discretisation schemes exist: explicit or implicit (Grossman and Roos, 2007). The explicit scheme is numerically the most simple and straightforward but it is not stable for large time steps which make it compu-

tationally expensive. The implicit schemes regroup the fully implicit scheme and the Crank-Nicolson scheme (Crank and Nicolson, 1947) (which is actually obtained by averaging the explicit and the fully implicit schemes). Both of these schemes are consistent and unconditionally stable, making them a better choice. Moreover, according to Lax's theorem (Lax and Ritchmyer, 1956), as long as a scheme is consistent and stable it converges. Hence, what differentiate the fully implicit and the Crank-Nicolson schemes are their order of convergence (or in other word their speed of convergence). The fully implicit scheme has a first order of convergence in time while the Crank-Nicolson scheme has a quadratic convergence (second order) which seems to make it more appealing. However, according to Patankar (1980), for large time steps, the Crank-Nicolson scheme may lead to oscillatory solutions (at least for heat transfer problems). Even if it converges it does not guarantee physically plausible solutions. For a more detailed explanation, refer to Patankar and Baliga (1978) and Patankar (1980). Consequently, the fully implicit scheme was selected here.

The model was computed in *Python* (van Rossum, 1995) with a non-uniform spatial discretisation, meaning that the mesh size was refined at the interfaces between the wall materials, as well as between the wall and the exterior and interior ambience (more details given in Section 2.3.4). The spatial and temporal discretisation of this set of equations are presented in Appendix A. This model will be referred as *Room model* in the rest of the manuscript. An adaptive time stepping method was used for the temporal discretisation. It is described by Figure 2.2.

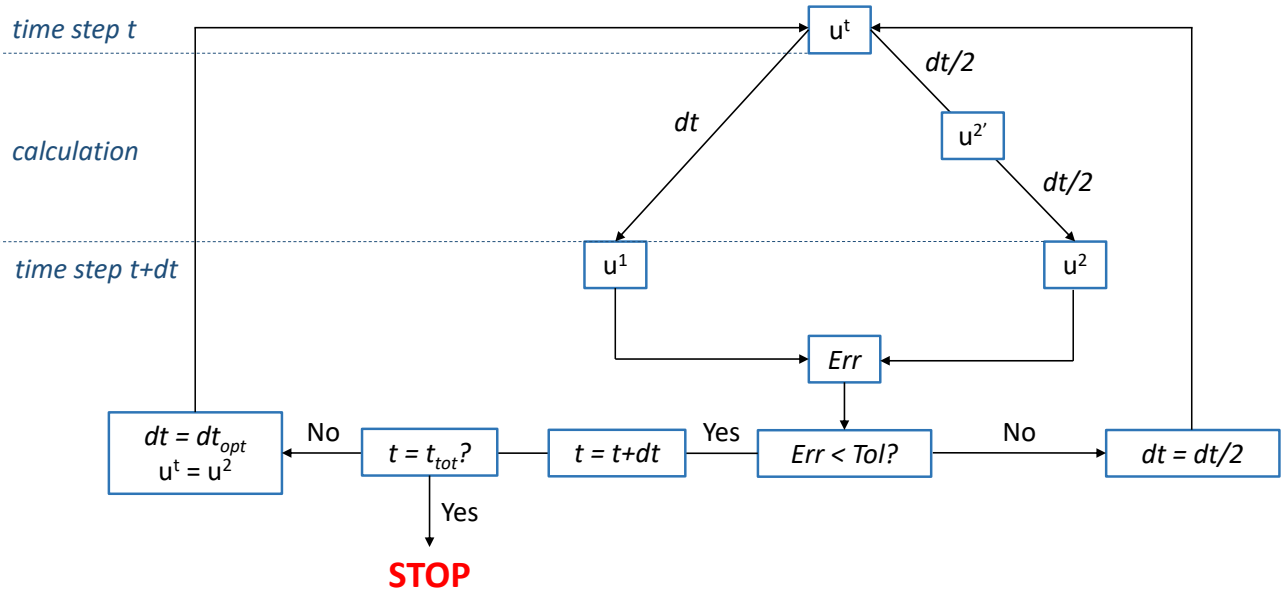

Figure 2.2 – Adaptive time-stepping method

The driving potentials at the time step $t + dt$ were calculated from the ones at

the time step t (u^t with $u = T$ or $u = p_c$ at each node of the mesh grid) in two ways: by doing one step from t to $t + dt$, and two steps with the first one from t to $t + dt/2$ and the second one from $t + dt/2$ to $t + dt$. This led to two results at the time $t + dt$: u^1 and u^2 respectively. The relative difference Err between u^1 and u^2 must respect a tolerance criterion Tol. This is translated by Eq. (2.19):

$$Err = \max\left(\left|\frac{u^1 - u^2}{u^2}\right|\right) < Tol \tag{2.19}$$

The tolerance criterion chosen was $Tol = 10^{-4}$. If it is respected, the time step was optimized for the next calculation thanks to Eq. (2.20) (Soderlind and Wang, 2003):

$$dt_{opt} = dt \cdot \left(\frac{Tol}{Err}\right)^{0.5} \tag{2.20}$$

where dt_{opt} is the optimized time step (s) and dt the simulation time step (s). Otherwise, the time step was divided by two, until the tolerance criterion is satisfied.

2.3.2 Exterior boundary conditions

The exterior boundary conditions accounted for the convective heat and mass transfer between the wall and the exterior environment, and the radiative heat transfer. These phenomena are illustrated in Figure 2.3.

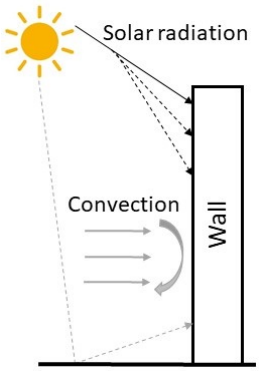

Figure 2.3 – Exterior boundary conditions

No wind-driven rain was simulated in this work. Its impact is strongly dependent on the building typology and on the localisation of the room in the building, as some façades are not directly exposed to rain (Carmeliet et al., 2004). Wind-driven rain could significantly increases moisture content at inside wall surfaces as shown by Abuku et al. (2009) on a tower made of only bricks. However, this configuration is theoretical and highly unusual. Walls are generally protected by a overhanging roof and waterproof coatings preventing water from penetrating.

2.3.2.1 Vapour exchange between the exterior surface and the air

The vapour exchange between the exterior surface of a wall and the atmosphere was described by means of a convective surface transfer coefficient $h_{m,ext}$:

$$g_{conv} = h_{m,ext}(p_{v,ext} - p_{v,es}) \tag{2.21}$$

As the driving potential is the capillary pressure p_c, expressing $p_{v,es}$ as a function of $p_{c,es}$ by using Gibbs' law leads to equation (2.22):

$$g_{conv} = h_{m,ext}\left[p_{v,ext} - p_{sat}(T_{es})exp\left(-\frac{p_{c,es}}{\rho_l R_v T_{es}}\right)\right] \tag{2.22}$$

As the capillary pressure is included in an exponential function, it was linearised thanks to a Taylor development at the first order. The demonstration is given in Appendix A.

2.3.2.2 Convective heat exchange

Similarly, the convective heat exchange between the exterior surface of the wall and the atmosphere was expressed by using a convective heat transfer coefficient $h_{h,ext}$:

$$q_{conv} = h_{h,ext}(T_{ext} - T_{es}) \tag{2.23}$$

2.3.2.3 Radiative heat transfer

Radiative heat transfer in buildings accounts for a large part of the heat exchange with the environment. The radiative heat transfer included two types of radiation:

- Long-wave radiation between the surface of the wall and its environment (ground, other buildings, vegetation...);
- Short-wave radiation from the sun composed of direct and diffuse radiation. The latter combines the radiative diffusion by the atmosphere and by the environment.

The radiative flux on a surface is dependent upon the intensity of the radiation and its angle with the surface. Many parameters intervene:

- The time;
- The state of the atmosphere (clear sky, cloudy...);
- The sun position in the sky;
- The wall surface orientation relative to the sun and the horizontal.

From solar hour to legal hour

Due to the ellipticity of the Earth's orbit and the tilt of the Earth's axis, the sun crosses the sky at different rate and times of the year. To track the motion of the sun, the *apparent solar time* (AST) is defined. On the other hand, the *mean solar time* (MST) is defined to create a uniform time scale for practical use. It describes the motion of a theoretical "mean sun" with noons 24 hours apart. Consequently, to have an accurate measurement of the radiative heat flux, it is necessary to consider the real position of the sun in the sky.

The time difference between the AST and the MST can reach as much as 16 minutes. This difference is given by the equation of time E_T:

$$MST = AST + E_T \tag{2.24}$$

It is common to find tables giving the correction to be applied by the equation of time for each day. Alternatively, the National Oceanic and Atmospheric Administration (NOAA) proposes a calculation method based on equations from astronomical algorithms (Meeus, 1998). First, the fractional year (γ) is calculated (in radians):

$$\gamma = \frac{2\pi}{365}(\text{day-of-year} - 1 + \frac{hour - 12}{24}) \tag{2.25}$$

For leap years, 366 is used instead of 365 in the denominator. From (2.25) the equation of time (in minutes) can be estimated Spencer (1971):

$$\begin{aligned} E_T = 229.18(&0.000075 + 0.001868cos(\gamma) - 0.032077sin(\gamma) \\ &- 0.014615cos(2\gamma) - 0.040849sin(2\gamma) \end{aligned} \tag{2.26}$$

Calculating the MST leads to the universal time (UT), which is the mean solar time at the Greenwich meridian, by adding or subtracting 4 minutes per degree of longitude (L) (+ in the East direction and - in the West direction):

$$UT = MST + \frac{4L}{60} \tag{2.27}$$

From the UT, the legal hour (LH) (or local time) is determined by applying a correction C. This correction is specific to the country: for example in France $C = 1$ hour in winter and 2 hour in summer:

$$LH = UT + C \tag{2.28}$$

Finally, the MST can be expressed as a function of the LH thanks to (2.27) and

(2.28); injecting it in (2.24) yields:

$$AST = LH - E_T - \frac{4L}{60} - C \tag{2.29}$$

Long-wave radiation

The total long-wave radiation q_{LWR} (W/m^2) can be defined as the sum of the radiative exchange of the surface with the ground q_{gro} and the sky q_{sky}:

$$q_{LWR} = q_{gro} + q_{sky} \tag{2.30}$$

Applying the Stefan-Boltzmann law to each component yields:

$$q_{LWR} = \sigma\epsilon F_{gro}(T_{gro}^4 - T_{es}^4) + \sigma\epsilon F_{sky}(T_{sky}^4 - T_{es}^4) \tag{2.31}$$

where F is the view factor and subscript gro stands for *ground*. This equation was then linearised to make it compatible with the energy conservation equation:

$$q_{LWR} = h_{r,gro}(T_{gro} - T_{es}) + h_{r,sky}(T_{sky} - T_{es}) \tag{2.32}$$

where:

$$h_{r,gro} = F_{gro}\frac{\epsilon\sigma(T_{es}^4 - T_{gro}^4)}{(T_{es} - T_{gro})}$$
$$h_{r,sky} = F_{sky}\frac{\epsilon\sigma(T_{es}^4 - T_{sky}^4)}{(T_{es} - T_{sky})}$$

Here, the view factors F were taken equal to 0.5 each and the ground temperature was taken equal to the air temperature (Janssen et al., 2007).

The sky temperature can be calculated with numerous equations. For example, the approximation of Loveday and Taki (1996):

$$T_{sky} = T_a - 6°\text{C} \tag{2.33}$$

or Cole (1976) expressed the sky temperature as a function of the cloud coverage:

$$\begin{aligned} T_{sky} &= 9.365574 \times 10^{-6}(1 - cf)T_a^6 + cf[(1 - 0.84cf) \\ &(0.527 + 0.161e^{8.45(1-273.15/T_a)}) + 0.84cf]T_a^4 \end{aligned} \tag{2.34}$$

where cf is the cloud covering factor in fraction of 1. This equation was also more recently used by Gan (2014). Janssen et al. (2007) implemented the following ex-

pression in their exterior boundary conditions model:

$$T_{sky} = T_a - (23.8 - 0.2025(T_a - 273.15))(1 - 0.87cf) \tag{2.35}$$

According to Janssen et al. (2007), few deviations were noticed between the different expressions of the sky temperature. Consequently Eq. (2.35) was selected due to its simplicity.

Short-wave radiation

The short-wave radiation is composed of the direct (Dir), diffuse (Dif), and reflected (Ref) radiation. The radiative exchange was then expressed as follows:

$$q_{SWR} = \kappa(Dir + Dif + Ref) \tag{2.36}$$

where κ is the absorptivity of the surface material.

The direct radiation depends on (Figure 2.4):

- The angle between the incident radiation and the wall surface normal vector θ_i;
- The angle between the incident radiation and the vertical vector (Zenith) θ_z.

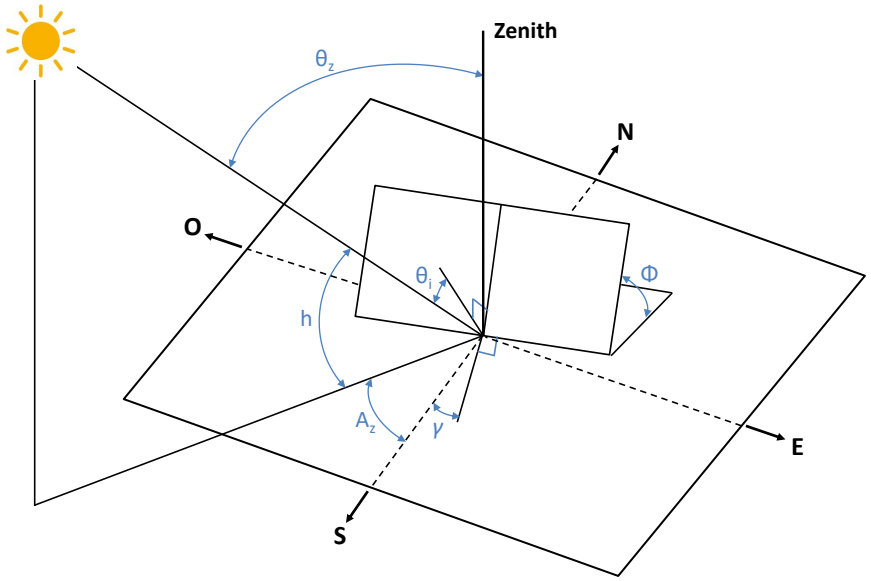

Figure 2.4 – Direct radiation on an inclined surface

θ_z and θ_i are key parameters to define the short-wave radiation. θ_z is equal to $\pi/2 - h$ where Z is the sun altitude. θ_i can be calculated by using the following equation

(Raoui et al., 2011):

$$cos(\theta_i) = cos(\theta_z) \cdot cos(\Phi) + sin(\theta_z) \cdot sin(\Phi) \cdot cos(A_z - \gamma) \tag{2.37}$$

where Φ is the angle of inclination of the surface against the horizontal (°), A_z is the azimuth considered negative in the East direction, and γ the orientation of the surface against the South.

The direct radiation on the wall surface can be expressed as a function of the direct horizontal or normal radiation:

$$Dir = \frac{cos(\theta_i)}{cos(\theta_z)} Dir_H = cos(\theta_i) Dir_N \tag{2.38}$$

The diffuse radiation corresponds to the diffusion of the solar beams by the atmosphere:

$$Dif = \frac{1 + cos(\Phi)}{2} Dif_H \tag{2.39}$$

The reflected radiation consists of the reflexion of the solar beams by the environment. The property of the environment to reflect the radiation is called *albedo* (Alb) which is a dimensionless coefficient defined as the ratio between the reflected and incident radiation. It varies with the material: from 0 for a blackbody to 1 for a perfect mirror. Consequently, the reflected radiation is calculated as follows:

$$Ref = \frac{1 - cos(\beta)}{2} Alb(Dir_H + Dif_H) \tag{2.40}$$

where the direct horizontal radiation is derived from (2.38):

$$Dir_H = \frac{cos(\theta_z)}{cos(\theta_i)} Dir \tag{2.41}$$

2.3.2.4 Latent and sensible heat exchange

The latent and sensible heat transfer due to vapour exchange corresponds to the convective vapour exchange (2.22) weighted by the energy of water vapour:

$$q_{m,conv} = (c_{p,v} T_{es} + L_v) g_{conv} = h_{eq,ext}[p_{v,ext} - p_{v,es}] \tag{2.42}$$

where $h_{eq,ext}$ is the equivalent exterior surface transfer coefficient defined as:

$$h_{eq,ext} = (c_{p,v} T_{es} + L_v) h_{m,ext}$$

2.3.2.5 Calculation of the convective surface transfer coefficients

The convective heat transfer coefficient (CHTC) at the exterior surface is dominated by forced convection due to the wind. Hence, it depends of the measured local air velocity. Numerous empirical relationship linking the CHTC to the local air velocity exist ((Loveday and Taki, 1996) and (Hagashima et al., 2005) for example). The one from Sharples (1984) is selected here:

$$\begin{aligned} h_{h,ext} &= 1.7V_{loc} + 5.1 \\ V_{loc} &= 1.8V + 0.2 \quad \text{(windward)} \\ V_{loc} &= 0.4V + 1.7 \quad \text{(leeward)} \end{aligned} \tag{2.43}$$

where V is the wind speed (m/s) and V_{loc} is the local wind speed (m/s).

To calculate the convective mass transfer coefficient (CMTC), the Lewis' analogy (quoted by Janssen et al. (2007)) was used:

$$h_{m,ext} = 7.7 \cdot 10^{-9} h_{h,ext} \tag{2.44}$$

2.3.3 Interior boundary conditions

Convective mass and heat transfer were considered for the interior boundary conditions. These phenomena are described by Eqs. (2.22) and (2.23) respectively, and by replacing subscripts ext by int and es by is. The CHTC was taken equal to 4 $W/(m^2.K)$ as this value was deemed representative of the convective exchange between indoor air and vertical walls according to Miranville (2002). As for the exterior boundary conditions, the Lewis' analogy was used to calculate the CMTC.

2.3.4 Validation of the heat and moisture transfer module

The coupled heat and moisture transfer model was validated with the standard EN 15026 (Afnor, 2007). A semi-infinite wall initially at $T = 20°C$ and $\Psi = 50\%$ was subjected to Dirichlet boundary conditions $T = 30°C$ and $\Psi = 95\%$, applied on its left surface. The wall was made of one material which properties — corresponding to a load-bearing material — were specified in the standard and are given below:

- Water content of the material (kg/m^3):

$$w = \frac{146}{\left[1 + (8 \times 10^{-8} p_c)^{1.6}\right]^{0.375}} \tag{2.45}$$

- Water vapour permeability (s):

$$\delta_v = \frac{M_w}{RT} \cdot \frac{26.1 \times 10^{-6}}{200} \cdot \frac{1 - \frac{w}{146}}{0.503\left(1 - \frac{w}{146}\right)^2 + 0.497} \tag{2.46}$$

where M_w is the molar mass of water (kg/mol).

- Liquid permeability (s):

$$\begin{aligned}\delta_l =& exp(-39.2619 + 0.0704 \cdot (w - 73) - 1.7420 \times 10^{-4} \cdot (w - 73)^2 \\ & - 2.7953 \times 10^{-6} \cdot (w - 73)^3 - 1.1566 \times 10^{-7} \cdot (w + 73)^4 \\ & + 2.5969 \times 10^{-9} \cdot (w - 73)^5)\end{aligned} \tag{2.47}$$

- Thermal conductivity (W/(m.K)):

$$k_{mat} = 1.5 + \frac{15.8}{1000} w \tag{2.48}$$

- Thermal capacity of the dry material ($J/(m^3.K)$):

$$\rho_{mat} c_{p,mat} = 1.824 \times 10^6 \tag{2.49}$$

To pass this standard, the water content and temperature profiles at different time, namely 7, 30 and 365 days, must be between ±2.5% of an analytical solution. The semi-infinite wall was simulated by adopting a 20 m thickness as it led to a negligible 0.2°C increase of temperature on the right surface, while the water content evolution is limited to the first 20 cm. The profiles are plotted in Figure 2.5 and Figure 2.6 where the ±2.5% intervals are represented by the dots.

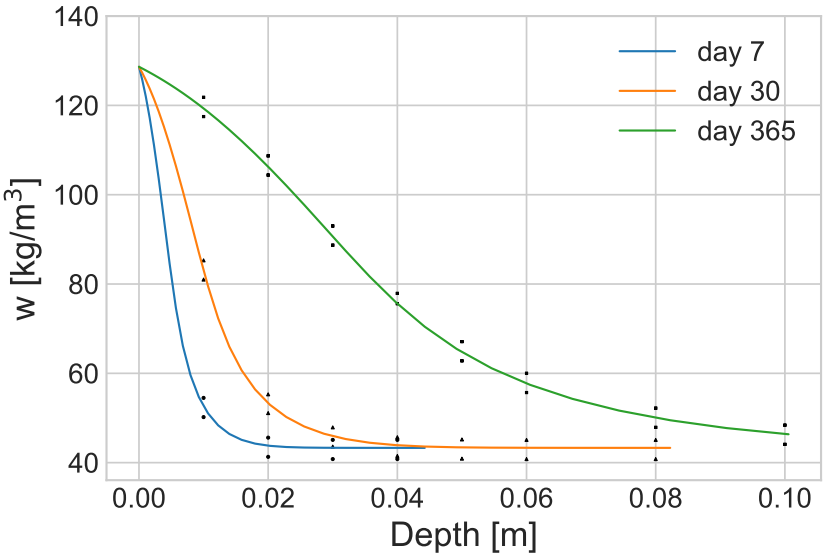

Figure 2.5 – Water content profiles at 7, 30 and 365 days

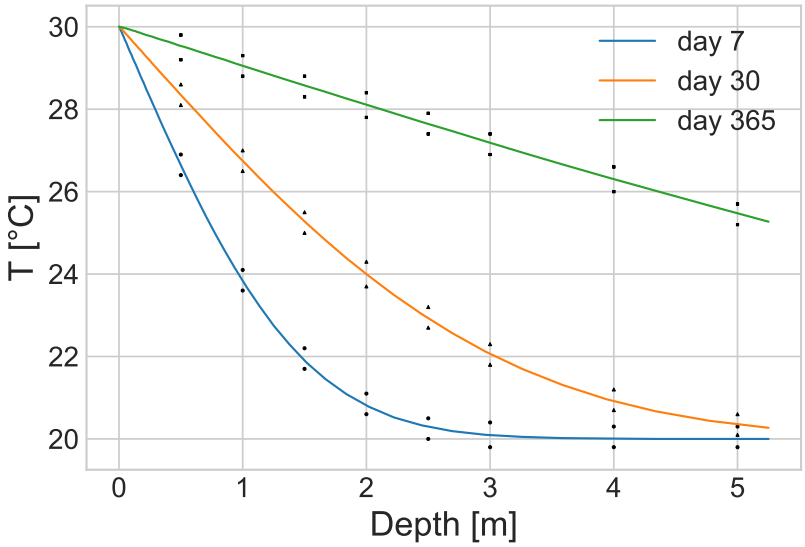

Figure 2.6 – Temperature profiles at 7, 30 and 365 days

All of the profiles presented in Figures 2.5 and 2.6 are between ±2.5% of the analytical solution, meaning that the model passed the standard. Additionally, the maximum difference between the calculated profiles and the standard was 0.83 kg/m^3 for the water content and 0.05°C for the temperature, leading to a satisfactory accuracy.

The simulations were done with a non-uniform mesh grid (refined at the interfaces, see Section 2.3.1.3). This grid is defined by the size of the first mesh, chosen arbitrarily equal to $5 \cdot 10^{-4}$ m, and a progressive factor characterizing the size of the

adjacent meshes:

$$dx_{i+1} = q \cdot dx_i \tag{2.50}$$

where dx is the mesh size (m), i is the position of the mesh and q is the progressive factor. A mesh grid sensitivity study led to tune the progressive factor to $q = 1.10$ as it gave the best compromise between the model accuracy and the calculation time.

2.4 Modelling of the air-conditioning system

Indoor air conditions are usually regulated by Heating, Ventilation and Air-Conditioning (HVAC) system. They are the most energy consuming equipments in buildings as they contribute to approximately 50% of the global energy consumption of buildings according to Pérez-Lombard et al. (2008) (around 45% in France (Dixit et al., 2010)). To support this statement, IDAE (2006) compared the energy consumption in households in Spain, Europe, USA and United-Kingdom (Table 2.1).

Energy consumption in households (%)	Spain	UE	USA	UK
Space conditioning	42	68	53	62
Domestic hot water	26	14	17	22
Lighting and appliances	32	18	30	16

Table 2.1 – Energy consumption in households in 2003 (IDAE, 2006)

Regulating properly these systems is then a crucial task to limit the energy consumption of buildings. Numerous approaches were investigated in the literature from a simple ON/OFF system to a regulation relying on machine learning algorithms. A review of different predictive control method can be found in Afram and Janabi-Sharifi (2014). However, the research presented here does not focus on an advance regulation method of the HVAC system. Consequently, each component of the HVAC was modelled independently and relied on a ON/OFF regulation. The four systems modelled were: a ventilation system, a heater, a humidifier and a split-type air-conditioner.

The ventilation rate was fixed and taken equal to 25 m^3/h per occupant as it corresponds to the minimum hygienic rate requirement indicated in the French labour law (Arrêté du 24 Mars 1982, 1982). The simulated room was supposed to always be ventilated.

For heating purposes, a heater was designed to provide a constant heating power

$\dot{Q}_{heat}$ (W). Daytime and nigh-time set point temperatures were selected, with a hysteresis of 0.5°C. Figure 2.7 illustrates the regulation of the temperature in a room for set point temperatures equal to 19°C for the night and 21°C for the day. The thermostat switched to the day temperature one hour before the arrival of an occupant in the room, and to the night temperature one hour before his departure to take advantage of the room inertia.

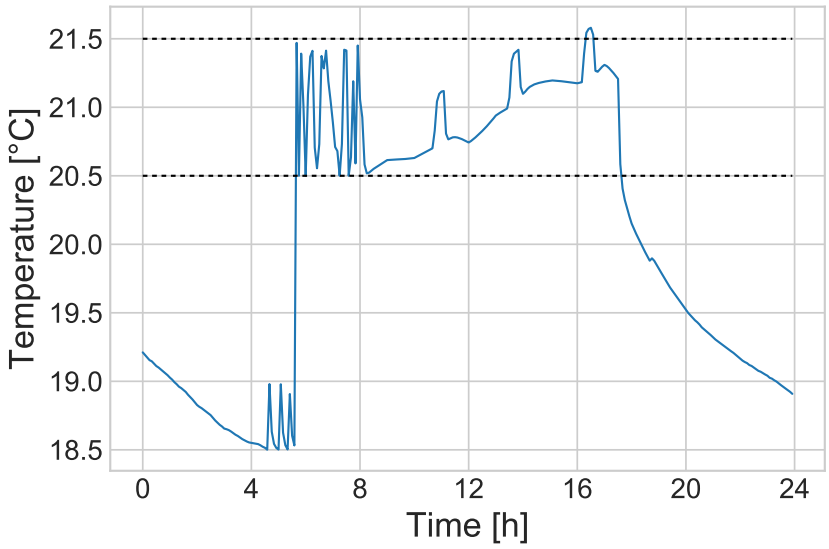

Figure 2.7 – Regulation of the temperature throughout a day with a hysteresis of 0.5°C. Set point temperatures equal to 21°C for the day and 19°C for the night

The humidifier also provided a constant water vapour production $\dot{m}_{humid}$ (kg/s). Its hysteresis was 2%. The humidifier was only turned on during the working hours.

For air cooling, a split-type air-conditioner was modelled under the assumption that the rate of the split $\dot{m}_{AC}$ was constant, and the temperature of the refrigerant fluid was equal to 2 °C. Like the heater, its hysteresis was 0.5°C. The air-conditioner was only turned on during working hours. The air dehumidification was a consequence of cooling it since the split type air-conditioner also removed water vapour. The dehumidification rate $\dot{m}_{dehumid}$ is calculated as follows:

$$\dot{m}_{dehumid} = \dot{m}_{AC}(x_{AC} - x_{int}) \tag{2.51}$$

where $\dot{m}_{AC}$ is the split flow rate (kg_a/s), and x_{AC} is the mass ratio of the split.

2.5 No-MASS platform: stochastic modelling of the occupants presence and activities

As presented in Chapter 1, the occupants' presence and activities in buildings may be modelled in three different ways:

- A constant heat and water vapour production throughout the day;
- A deterministic scenario;
- A stochastic approach.

Here, a stochastic approach was favoured as it is the most faithful in describing the real behaviour of the occupants in buildings. A platform called Nottingham Multi-Agent Stochastic Simulation (No-MASS) was chosen since it includes validated presence (Page et al., 2008) and activities models (Jaboob, 2015). This section aims at presenting No-MASS, and how the coupling with the *Room model* was done. As this research focused on offices, the activity model for non-residential buildings is not presented here.

2.5.1 Occupants' presence and activities in offices

Within No-MASS, the modelling of the occupants' presence (or absence) depends on the type of building. For residential buildings, absences were predicted by the activity model (Jaboob, 2015). For non-residential building (assimilated to offices in No-MASS), the occupants' presence was modelled in accordance with the model developed by Page et al. (2008). This model focuses on estimating whether an occupant is present within a zone of the building or not, under the assumption that the probability of presence at a time step depends only on the state of presence at the previous time step; meaning that the whole presence history was not considered. Mathematically this statement corresponds to considering the state of occupancy as a Markov chain (Bremaud, 1999):

$$P(X_{t+1} = i | X_t = j, X_{t-1} = k, ..., X_{t-N} = l) = P(X_{t+1} = i | X_t = j) =: T_{ij}(t) \quad (2.52)$$

where X_t is the random variable "state of presence at time step t" and i, j, k and l taking on values 0 (absent) or 1 (present). As the probability of an occupant arriving or leaving an office is not the same depending on the time of the day, the probability of transition $T_{ij}(t)$ had to be time-dependent, which corresponds to the general formulation of an inhomogeneous (or time-dependent) Markov chain. To determine the time dependence of these transition probabilities, the model needed the following input: the probability profile of presence over a typical week, and a

parameter of mobility that gives an idea on how much people move in and out in the zone. This model generates a sequence of zeros (absence) or ones (presence) characterizing each occupant arrivals or departures from a zone. It does not simply reproduce the pattern given as an input, but create a pattern that never repeats itself. To do so, it relies on the inverse function method that generates a time series of events from a given probability distribution function. These functions are the probabilities of transition T_{00}, T_{01}, T_{10} and T_{11}. If we want to know an occupants' change of state of presence, a random value between 0 and 1 is selected and then compared to the probabilities of transition. If this value is smaller or equal to the probability of transition characterising a change of state event, the event takes place ; if it is greater it does not take place (see Page (2007) for more details). The probability of presence at the time step $t+1$ was then deduced from the one at the time step t from these probabilities of transition:

$$P(t+1) = P(t) \cdot T_{11}(t) + (1 - P(t)) \cdot T_{01}(t) \tag{2.53}$$

From this equation, we can deduced:

$$T_{11}(t) = \frac{P(t) - 1}{P(t)} \cdot T_{01}(t) + \frac{P(t+1)}{P(t)} \tag{2.54}$$

To avoid the dependence between T_{11} and T_{01}, a parameter of mobility was defined as the ratio between the probability of change of presence that of no change:

$$\mu(t) = \frac{T_{01}(t) + T_{10}(t)}{T_{00}(t) + T_{11}(t)} \tag{2.55}$$

Note that in No-MASS, this parameter is constant and equal to 0.11 based on Page et al. (2008) to simplify the input data. Consequently, the probabilities of transition become (from absent to present):

$$T_{01}(t) = \frac{\mu - 1}{\mu + 1} P(t) + P(t+1) \tag{2.56}$$

Or when the occupant remains in the room (from present to present, 1 to 1):

$$T_{11}(t) = \frac{P(t) - 1}{P(t)} \left[\frac{\mu - 1}{\mu + 1} P(t) + P(t+1) \right] + \frac{P(t+1)}{P(t)} \tag{2.57}$$

The other two probabilities of transition were then deduced: $T_{10} = 1 - T_{11}$ (from present to absent) and $T_{00} = 1 - T_{01}$ (from absent to absent). The model was then calibrated and validated thanks to data provided by the monitoring of a twenty zones office building (located in Lausanne) for five years where people worked mainly on research and teaching. The model was conceived to be independent on the charac-

teristics of the occupants (gender, age, social category, etc...) as the input is only the probability profile of presence over a week. Hence, it should be applicable for any occupant's archetype. For example, Vorger (2014) based his work on this model and generalized it to French survey data. He was also able to predict long term absences based on statistical data from social sciences survey.

In offices, the only considered activity was working on a computer (information technology: IT).

2.5.2 Heat and vapour sources

Heat and vapour sources related to the occupants presence and activities may be decomposed into two categories:

- Metabolic heat and vapour sources;
- Heat generation from equipments (other than the air-conditioning system).

The metabolic heat gains calculation was done in No-MASS. The calculation method can be found in the Annex D of the standard EN ISO 7730 (Afnor, 2005). Each occupant was inferred a state, a location, a clothing level and a metabolic rate. For the IT activity, the clothing level is set to 1 *clo* and the metabolic rate to 116 W/m^2 in accordance with the standard EN ISO 7730 (Afnor, 2005). It accounts for the heat diffusion through skin, sweating, latent and dry respiration, radiation and convection. The calculation of the metabolic heat gains depends on the indoor environmental conditions (i.e the temperature and relative humidity of air), the air velocity was assumed constant and equal to 0.1 m/s, and the external work was taken null; the latter corresponding to the metabolic free energy while performing an activity.

As there is no standard dedicated to the calculation the metabolic water vapour production, a value of 48 g/h per occupant as selected from Johansson et al. (2010a). This study was based on a literature review on the type of activity and its duration. In our work, the duration of an activity is irrelevant as it was already pre-processed within No-MASS. The value of 48 g/h is also in accordance with the one from ASHRAE (2005) for a full grown man. Note that according to ASHRAE (2005), it has to be reduced by 15% for a woman.

Heat sources from the equipments included the use of computers and lighting. No-MASS presence module generated only the occupants presence, hence the equipments were included in the *Room model*. To be in agreement with No-MASS, a

constant heat generation of 150 W per computer was selected as it corresponds to the value in No-MASS activity module (Jaboob, 2015). As there is no way of differentiating one occupant from another in No-MASS, it was assumed that all the computers were turned on at the arrival of the first occupant, and turned off at the departure of the last one. For the lighting, a production of 10 W/m^2 from Steeman et al. (2009) was selected. It was assumed that the lights would be turned on between 1 hour before sunset and 1 hour after sunrise if an occupant is present in the room.

2.6 Coupling of the *Room model* and No-MASS

The *Room model* and No-MASS are both simulation tools written in different programming language (the former in *Python* and the latter in $C++$). To make them work together, one has to rely on the Functional Mock-up Interface (FMI) standard which is the result of the Information Technology for European Advancement (ITEA2) project MODELISAR (Nouidui et al., 2014). The FMI standards consists of two parts:

- FMI for model exchange: this standard explains how a modelling environment can generate a C-code that can be utilized by other modelling and simulation environments;
- FMI for co-simulation: it is an interface standard for coupling two or more simulation programs in a co-simulation environment.

The communication between the simulation programs was done through shared libraries which contain the implementation of the FMI functions (defining the input and return arguments) and a XML file (also called the model description file) which contains the variable definitions and the informations on the model.

Some examples on the use of a FMI can be found in the literature: Djedjig et al. (2015) coupled a green envelope model in *Python* with the building simulation software TRNSYS in order to investigate the impact of the envelope on the thermal, aeraulic and hydric phenomena at building scale. Additionally, Gobakis and Kolokotsa (2017) coupled a building energy simulation software with microclimate models in order to assess the impact of urban outdoor conditions on the energy consumption and indoor environmental quality.

The coupling of No-MASS and the *Room model* is given in Figure 2.8.

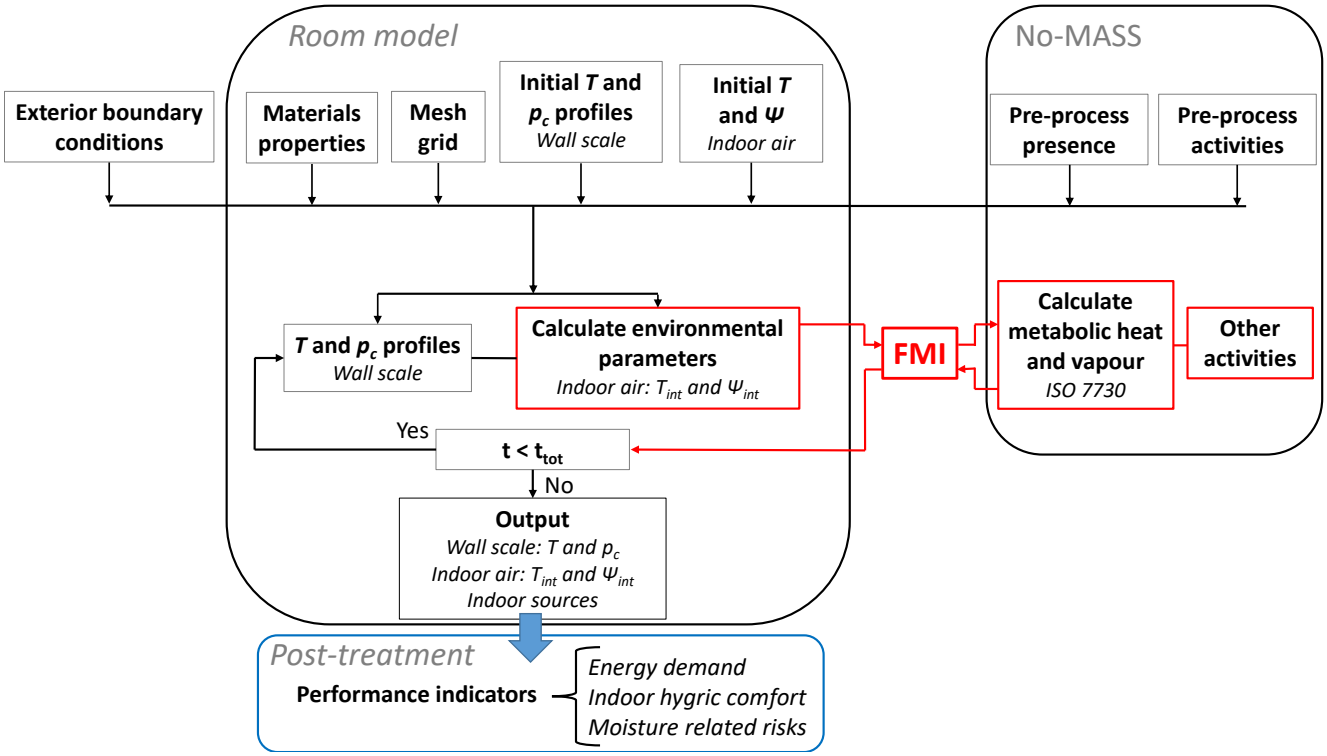

Figure 2.8 – Scheme of the coupling between No-MASS and the *Room model*

At the start of a simulation, the occupants' presence and activities were pre-processed in No-MASS as they are independent on the indoor environmental parameters (temperature and relative humidity). The *Room model* initialised the temperature and capillary pressure profiles in the wall, and the indoor temperature and relative humidity. At the next time step, these parameters were firstly calculated by the *Room model* before being communicated to No-MASS. No-MASS then determined the metabolic heat gains and vapour production. At this stage, No-MASS can parsed the indoor environmental parameters to estimate the occupants' probability of performing other activities. They include the use of windows estimated by Haldi and Robinson (2009) model, and households related activities from Jaboob (2015) model. The coupling of these modules was not done in our approach yet. Finally, the process continues until the end of the simulation.

A time step sensitivity study led to choose a 5 minutes simulation time step for No-MASS (Chapman et al., 2017) (the *Room model* uses an adaptive time-stepping method). As the exterior boundary conditions were given with a 1 hour time step, a linear interpolation was done to match the interior ones.

The simulation results were the temperature and capillary pressure in the walls, the indoor conditions, as well as the power and vapour production of the air-conditioning system obtained with a 5 minutes time step. These parameters can be used when the simulation is completed to compute performance indicators. They

are defined in the next section.

Depending on the computer specifications, a simulation on one year of data lasted between two and four days.

2.7 Definition of the performance indicators

The *Room model* is composed of three modules: the coupled heat and moisture transfer at wall scale, the stochastic modelling of the occupants presence and activities (via No-MASS platform) and the modelling of the air-conditioning system. In order to assess the hygrothermal performance of a room, one indicator associated to each module was defined:

- The energy demand of the air-conditioning system;
- The indoor hygric comfort;
- The moisture related risks in the room envelope.

2.7.1 Energy demand

The estimation of the energy demand of a room is straightforward as it corresponds directly to the demand of the air-conditioning system, namely the heater, the humidifier and the air-conditioner.

For the heater, the energy demand was directly given by its power $\dot{Q}_{heat}$.

The humidifier generated constant water vapour $\dot{m}_{humid}$. To deduce its demand $\dot{Q}_{humid}$ (in W), the following equation was used:

$$\dot{Q}_{humid} = \dot{m}_{humid} \left(c_{p,v} T + L_v \right) \tag{2.58}$$

where T corresponds to the temperature needed to produce water vapour (100°C).

The air-conditioner power $\dot{Q}_{AC}$ (W) was calculated at each time step thanks to Eq. (2.59) based on a thermodynamic balance:

$$\dot{Q}_{AC} = \dot{m}_{AC}(h_{AC} - h_{int}) \tag{2.59}$$

where h_{AC} is the specific total enthalpy of the air in the air-conditioner (J/kg). This power varies at each time step as the specific enthalpy of the indoor air varies with the temperature. The efficiency of all the equipments was not considered.

2.7.2 Indoor hygric comfort

The occupants' comfort is a subjective notion which might differs widely from one individual to another. Factors influencing it can be personal (metabolic rate, clothing type, thermal sensitivity, ...) and environmental (room temperature and relative humidity, air velocity, ...). One of the most used comfort criterion is the Predicted Mean Vote (PMV) which is governed by the standard EN ISO 7730 (Afnor, 2005). It relies on a seven points scale from -3 to +3 where -3 corresponds to the occupant feeling cold, +3 feeling warm and 0 feeling comfortable. The PMV can be directly calculated from the indoor temperature and relative humidity making it convenient to use. However, it relies on an energy balance equation, meaning that the relative humidity has a limited impact on its value. This conclusion is also in adequacy with the one reached by Fermanel and Miriel (1999) and Bui et al. (2017b). Therefore, another criterion focusing on humidity needed to be selected.

According to Sulaiman and Olsina (2014), the most used comfort criterion is the one from the ASHRAE standard 55 (ASHRAE, 2005). It has been developed thanks to surveys carried on individuals placed in controlled chambers. This led to define a comfort region constrained by threshold values on the air temperature and the relative humidity (Figure 2.9)

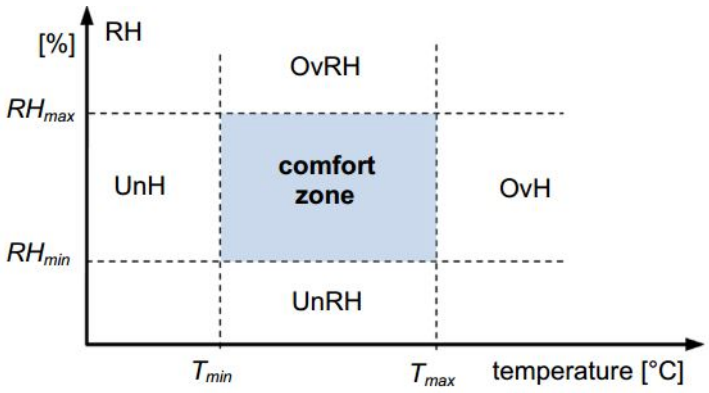

Figure 2.9 – Hygrothermal region for human comfort (Sulaiman and Olsina, 2014)

The threshold values defined to respect the comfort zone are (ASHRAE, 2005):

$$T_{min} = 19°\text{C}$$
$$T_{max} = 26°\text{C}$$
$$RH_{min} = 30\%$$
$$RH_{max} = 70\%$$

where RH is the relative humidity. For controlled environmental conditions however,

the wide range of temperature and relative humidity covered by these intervals might lead to inconsistent results. Consequently, a more restrictive criterion was chosen: the one of Wolkoff and Soren (2007), defining the comfort region for a relative humidity between 40 and 50%. The air is then defined as "comfortable" for a humidity between 40 and 50%, "too dry" under 40% and "too humid" above 50%.

2.7.3 Moisture related risks

High relative humidity might lead to mould growth on the surface and/or inside the walls assemblies. The proliferation on fungi on a wall can provoke the spread of pathogens in the air which impact the occupants' health. Within the wall, mould may deteriorate the wall assemblies affecting directly the hygrothermal and the mechanical performance of the structure. This is especially true for wall assemblies made of biobased materials as they are more sensitive to moisture.

In the literature, different models were developed to predict mould growth: the IEA-Annex 14 model (IEA-Annex 14, 1990), the Time-of-wetness (Adan, 1994), Johannson's mould growth indices (Johansson et al., 2010b), the Fungal index (Abe et al., 1996), the VTT model (Hukka and Viitanen, 1994), the Isopleth model and the Biohygrothermal model (Sedlbauer, 2001). A brief review of each of these models can be found in Vereecken and Roels (2012). In this work, two models were chosen: the isopleth model and the VTT model. They are described below.

Isopleth model

An isopleth is a curve describing the proliferation of bacteria risk in dependence on temperature and relative humidity. Temperature and relative humidity couples are represented at each time on a scatter plot (as illustrated in Figure 2.10). A hyperbolic limit curve is also plotted, determining the threshold value of temperature and relative humidity couples for which mould growth may happen.

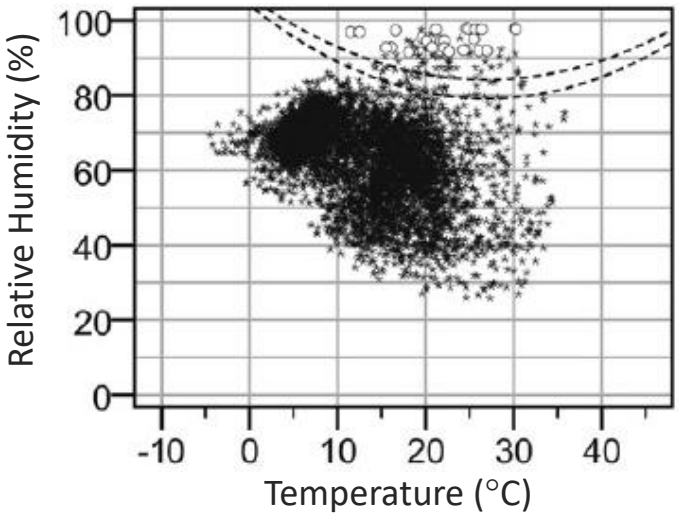

Figure 2.10 – Example of an isopleth (Johansson et al., 2013)

Different equations can be used to determine the limit curve. Johansson et al. (2013) used a parabolic equation described by Eq. (2.60):

$$\Psi = a + c(T^2 - 54T) \tag{2.60}$$

with Ψ in (%), a and c are given by Eq. (2.61):

$$\begin{aligned} c &= (\Psi_{crit1} - \Psi_{crit2}) / \left[T_1^2 - T_2^2 - 54(T_1 - T_2)\right] \\ a &= \Psi_{crit1/2} - c(T_1^2 - 54T_1) \end{aligned} \tag{2.61}$$

where $T_1 = 22$°C and $T_2 = 10$°C define the range in which a critical moisture level is expected (Johansson et al., 2013). To determine Ψ_{crit1} and Ψ_{crit2}, Johansson et al. (2014) put samples of different materials in humidity-controlled chambers, with humidity changes at intervals of 5%. Therefore, two curves were defined corresponding to the humidity for which mould appears, and the next-lowest humidity (see Figure 2.10). To be on the safe side, it was assumed that mould appears if the temperature and humidity couples are above the lowest curve. As Johansson et al. (2013) seem to cover the widest range of materials, their model was implemented in the *Room model*.

VTT model

While the isopleths give the mould growth risk for every temperature and relative humidity couples, the time of exposure of the material to high relative humidities is not considered. Thus, the second mould fungi prediction model used was a dynamic

model called VTT (named after the VTT Technical Research Centre of Finland Ltd) (Hukka and Viitanen, 1994). Initially, the VTT model was an empirical prediction model based on laboratory experiments on pine and spruce sapwood. It was then extended other building materials, leading to the updated VTT model (Ojanen et al., 2010).

First, the mould index MI is defined and given in Table 2.2. It is often considered that $MI = 1$ is the maximum tolerable value.

Mould index MI	**Growth rate**	**Description**
0	No mould growth	Spores not activated
1	Small amounts of mould on surface	Initial stages of growth
2	<10% coverage of mould on surface	
3	10-30% coverage mould on surface, or <50% coverage of mould (microscopic)	New spores produced
4	30-70% coverage mould on surface; or >50% coverage of mould (microscopic)	Moderate growth
5	>70% coverage mould on surface	Plenty of growth
6	Very heavy, dense mould growth covers nearly 100% of the surface	Coverage around 100%

Table 2.2 – Mould index MI (Ojanen et al., 2010)

The change in mould index is given by Eq. (2.62)

$$\frac{dMI}{dt} = \frac{k_1 k_2}{7 \cdot t_{MI=1}} \tag{2.62}$$

where k_1 is the intensity of the mould growth under favourable conditions and k_2 represents the growth intensity when MI approaches the maximum peak value in the range $4 < MI < 6$.

k_1 is calculated by Eq. (2.63):

$$k_1 = \begin{cases} 1, & \text{when } MI \leq 1 \\ \frac{2}{t_{MI=3}/t_{MI=1}-1}, & \text{when } MI > 1 \end{cases} \tag{2.63}$$

where $t_{MI=1}$ and $t_{MI=3}$ are respectively the time needed to reach $MI = 1$ and $MI = 3$. In the original model (for wood), these parameters are given by Eqs. (2.64) and (2.65) (Hukka and Viitanen, 1994) in case of constant temperature and

relative humidity:

$$t_{MI=1} = exp[-0.68ln(T) - 13.9ln(\Psi) + 0.14W - 0.33SQ + 66.02] \tag{2.64}$$

$$t_{MI=3} = exp[-0.74ln(T) - 112.72ln(\Psi) + 0.06W + 61.50] \tag{2.65}$$

where W is the timber species (0 = pine, 1 = spruce), SQ is the surface quality equal to 0 for other materials than wood (else it is equal to 0 for sawn surface or 1 for kiln-dried quality). k_2 is described by:

$$k_2 = max[1 - exp(2.6 \cdot (MI - MI_{max})), 0] \tag{2.66}$$

with MI_{max} the maximum mould index level:

$$MI_{max} = 1 + 7\frac{\Psi_{crit} - \Psi}{\Psi_{crit} - 100} - 2\left(\frac{\Psi_{crit} - \Psi}{\Psi_{crit} - 100}\right)^2 \tag{2.67}$$

where Ψ_{crit} is defined as the lowest relative humidity under which mould growth may occur:

$$\Psi_{crit} = \begin{cases} -0.00267T^3 + 0.160T^2 - 3.13T + 100.0, & \text{when } T \leq 20°\text{C} \\ \Psi_{min}, & \text{when } T > 20°\text{C} \end{cases} \tag{2.68}$$

Additionally, the dynamic behaviour of the model is described by a decrease on the mould index when the material is not subjected to favourable conditions leading to mould growth. This decrease is given by Eq. (2.69):

$$\frac{dMI}{dt} = \begin{cases} -0.00133, & \text{when } t - t_1 \leq 6h \\ 0, & \text{when } 6h < t - t_1 \leq 24h \\ -0.000667, & \text{when } t - t_1 > 24h \end{cases} \tag{2.69}$$

where $t - t_1$ (in h) is the time passed since the start of the unfavourable period.

To cover a wider range of materials, the VTT model was updated by Ojanen et al. (2010). Other laboratory experiments than the ones done for wood were conducted with different kind of materials. This led to modify the factors k_1, k_2 and MI_{max} in the previous equations as well as changing the Ψ_{min} value. MI_{max} is now dependent on three coefficients: A, B and C (Eq.(2.70)):

$$MI_{max} = A + B\frac{\Psi_{crit} - \Psi}{\Psi_{crit} - 100} - C \cdot \left(\frac{\Psi_{crit} - \Psi}{\Psi_{crit} - 100}\right)^2 \tag{2.70}$$

Values of the coefficients are given in Table 2.3 Ojanen et al. (2010).

Sensitivity class	Material groups	k_1 $MI < 1$	k_1 $MI \geq 1$	MI_{max}			Ψ_{min} (%)
				A	B	C	
Very sensitive	Untreated wood; includes lots of nutrients for biological growth	1	2	1	7	2	80
Sensitive	Planed wood, paper-coated products, wood-based boards	0.578	0.386	0.3	6	1	80
Medium resistant	Cement or plastic based materials, mineral fibers	0.072	0.097	0	5	1.5	85
Resistant	Glass and metal products, materials with efficient protective compound treatments	0.033	0.014	0	3	1	85

Table 2.3 – VTT coefficients depending on the material sensitivity class (Ojanen et al., 2010)

2.8 Summary

This chapter presented the development of a room model aiming at investigating the impact of the occupancy scenario and the walls moisture buffering.

The model is composed of three modules: the coupled heat and moisture transfer at wall scale, the air-conditioning system, and No-MASS platform generating stochastic occupancy scenarios. The coupled heat and moisture transfer equations were solved with the finite differences method (with an implicit scheme) in *Python*, and validated with the standard EN 15026 (Afnor, 2007). Though not being the focus of this research, the exterior boundary conditions were modelled, but no wind-driven rain was simulated. For the indoor boundary conditions, the air-conditioning system depicted by a ventilation system, a heater, a humidifier and a split-type air-conditioner were modelled.

The originality of this work comes from the modelling of the occupants' presence and activities in a stochastic way. This approach is used in the energy performance field and was imported in our work thanks to No-MASS platform developed by Chapman et al. (2017). As No-MASS is written in C++ and the *Room model* in *Python*, both models were coupled by using a Functional Mockup Interface. Table 2.4 on next page summarises the different module of the model and also lists the major parameters.

Finally, three performance indicators were defined to estimate the impact of the occupancy scenario and the walls moisture buffering effect:

- The energy demand of the air-conditioning system;
- The indoor hygric comfort estimated with Wolkoff and Soren (2007) criterion;
- The moisture related risks in the building envelope estimated with the isopleths (Johansson et al., 2013) and the VTT model (Hukka and Viitanen, 1994; Ojanen et al., 2010).

	Room model (Python)	No-MASS ($C++$)
Major assumptions	• No air transfer • No wind-driven rain • No window or shading device	• Same profile of presence for every occupant
Time step	Adaptive	5 minutes
Boundary conditions	• Convective heat and moisture transfer • Long-wave and short-wave radiation • Latent and sensible heat transfer due to vapour exchange	
Metabolic sources		• Heat: variable • Vapour: $48g/h/occupant$
Equipments	• Lighting: 10 W/m^2 • Computers: 150 $W/computer$	
Air-conditioning system	• Ventilation system: 25 $m^3/h/occupant$ • Heater • Humidifier • Split-type air-conditioner	

Table 2.4 – Listing of the major parameters of the simulations

Chapter 3

Influence of the occupancy scenario on the hygrothermal performance of a room

Contents

3.1 Introduction

As shown in Chapter 1, few hygrothermal model use a stochastic approach to model the occupants' presence and activities in buildings. Our approach to combine a room model with a stochastic occupancy model was presented in Chapter 2. This chapter aims to answer the second objective established in Chapter 1, namely the influence of the occupancy scenario on the hygrothermal performance of a room.

Therefore, the *Room model* sensitivity to different profiles of presence is investigated. Four different scenarios were applied to only one room configuration described in Section 3.2. The scenarios are presented in Section 3.5. The influence of the occupancy scenarios on the hygrothermal performance of the room was assessed through the performance indicators introduced in Chapter 2. Results are given in Section 3.6.

3.2 Case study

This chapter focuses on the configuration of only one room. The case study is an office of dimensions 5 m × 5 m × 2.5 m. One wall, made of 20 cm of concrete, 13 cm of gypsum board and 1.3 cm of plaster, was facing the South. The office was supposed to be surrounded by other offices which indoor temperature and relative humidity evolved in the same way as the ones from the simulated office. A symmetry condition was hence applied. The separating walls were made of two 1.3 cm thick gypsum boards with 6 cm of polystyrene in between. The floor and ceiling were made of 20 cm of concrete. To simulate a conventional interior coating acting as a vapour barrier, a vapour resistance Sd equal to 0.5 m was added to all the walls. Its thermal properties were considered negligible. No coating were added on the exterior surface. The materials properties are given in Section 3.3. The 3D representation of the office is presented in Figure 3.1 and the 2D one in Figure 3.2.

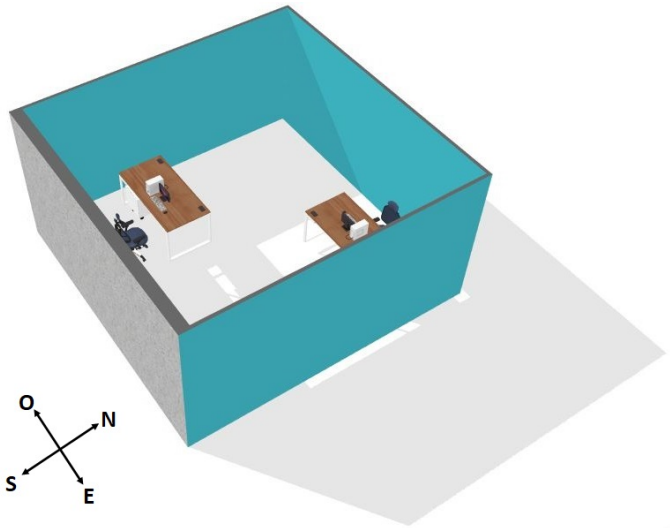

Figure 3.1 – 3D representation of the simulated office

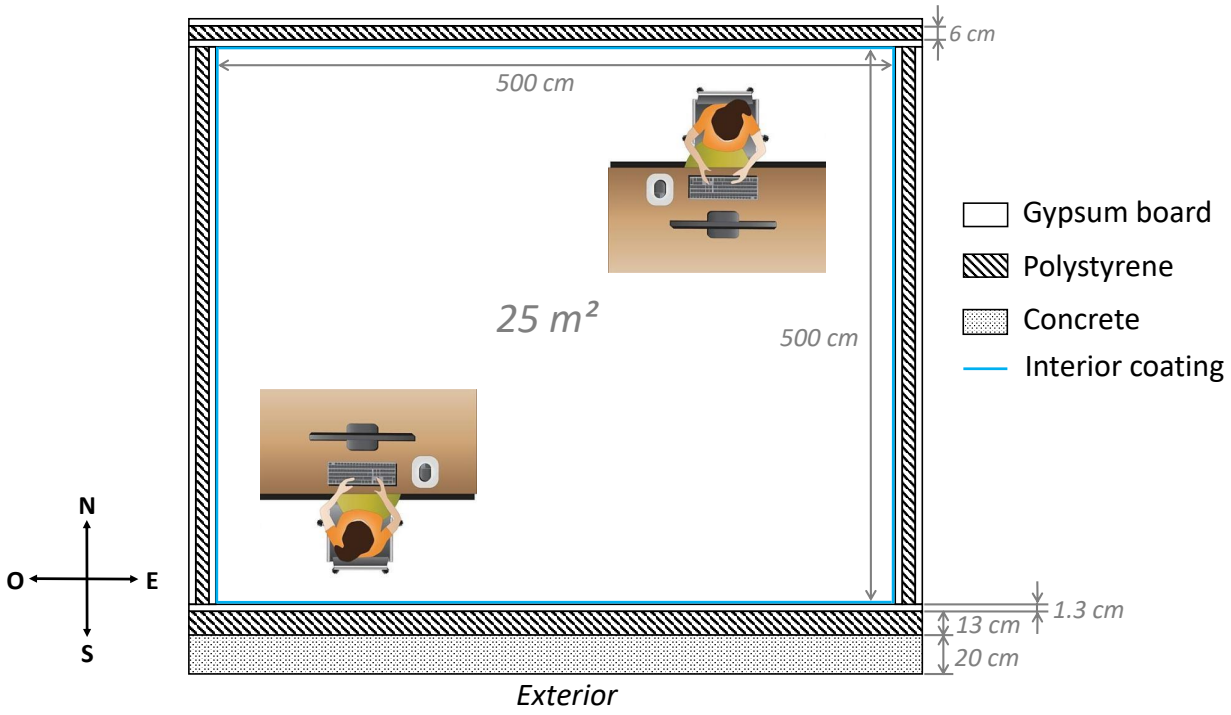

Figure 3.2 – 2D representation of the simulated office

Two male occupants were present in this office. Their sole activity, consisted in working on a computer. The use of lighting and computers were simulated in accordance with the method described in Chapter 2.

The exterior boundary conditions were the ones from Trappes (France) as it is considered to be representative of the French climate (temperate climate). They were given by the French code overseeing new buildings construction (RT Bâtiment,

2012). The simulations were run on one year of weather data starting on the first of January, assuming it was a Monday for the occupancy scenario. The evolution of the air temperature and relative humidity over the year are plotted in Appendix B.

The initial conditions were obtained by repeating the simulated year until the relative difference in capillary pressure and temperature fields in the walls between two consecutive year was below 2%. This was obtained after repeating the simulation for 5 years. The initial indoor air temperature and vapour pressure were the ones obtained after these 5 years.

3.3 Materials

The walls materials hygrothermal properties were extracted from the literature and are given in Tables 3.1, 3.3 and 3.3.

	ρ (kg/m^3)	k $(W/(m.K))$	C_p $(J/(kg.K)))$	$\delta_v \cdot 10^{-11}$ (s) dry cup	$\delta_v \cdot 10^{-11}$ (s)	$\delta_v \cdot 10^{-11}$ (s) wet cup
Concrete (1)	2300	1.6	850		0.11 *	
Polystyrene (2)	50	0.04	1450		0.32 *	
Gypsum board (3)	850	0.32	1000	2.6		3.5

Table 3.1 – Materials properties extracted from the literature

Concrete (1)	Ψ (%)	20	40	60	80	95	97
	w (kg/m^3)	24.5	34.1	40.4	64.6	108.6	126.1
Polystyrene (2)	Ψ (%)	20	40	60	80	95	97
	w (kg/m^3) $\cdot 10^{-2}$	1.3	1.8	2.6	5.2	20.3	32.9
Gypsum board (3)	Ψ (%)	20	40	60	80	95	97
	w (kg/m^3)	1.5	2.2	3.2	4.4	5.5	6.7

Table 3.2 – Sorption properties

Concrete [4]	$\delta_l(s)$	10^{-17}		
Polystyrene **	w (kg/m^3) $\cdot 10^{-2}$	2.6	5.2	32.9
	δ_l (s)	10^{-17}	10^{-15}	10^{-14}
Gypsum board **	w (kg/m^3)	3.2	4.4	6.7
	δ_l (s)	10^{-17}	10^{-15}	10^{-14}

Table 3.3 – Liquid water permeability

[1] Künzel et al. (2008)
[2] Labat et al. (2016)
[3] Delgado et al. (2013)
[4] Claisse et al. (2009)
* single value given
** assumption — no value available

For the polystyrene and the gypsum board, no liquid permeability values were available in the literature. Consequently, the ones corresponding to a highly porous material were selected in (Evrard, 2008). This permeability corresponds to a hemp concrete one.

3.4 Air-conditioning system

First, set point temperatures and relative humidities were selected for the air-conditioning system. For the heater, the set point temperatures were equal to 21°C for the day and 19°C for the night. The set point relative humidity of the humidifier was equal to 40% as it corresponds to the lower boundary of the interval of comfort defined by Wolkoff and Soren (2007) (see Section 2.7.2). It was only turned on during working hours. For air cooling, the set point temperature for the air-conditioner was equal to 24°C. Similarly to the humidifier, it was only turned on during working hours. As the air dehumidification was considered a consequence of cooling it, no set point relative humidity was selected for the air-conditioner.

The sizing of the air-conditioning system was done thanks to a mass and energy balance under constant conditions. For the heater and the humidifier, the exterior temperature and relative humidity of reference were equal to -5 °C and 60% respectively. These values were given by the French regulation code (RT Bâtiment, 2012). The sizing of the split type air-conditioner was done by considering the maximum indoor heat load (two occupants, two computers and lights turned on). This led to choose the following power and water vapour production for the air-conditioning system:

- The heater power was equal to 1500 W;
- The humidifier rate was equal to 0.35 kg_v/h;
- The split air flow rate was equal to 0.1 kg_a/s.

Note that the air-conditioner power varied over time as it was calculated as a function of the indoor air specific enthalpy which varied itself with the temperature (see Chapter 2.4).

3.5 Occupancy scenarios

Four different occupancy scenarios were simulated: stochastic, averaged, constant and deterministic; they are detailed in this section.

3.5.1 Scenario 1: SC1 — No-MASS scenario

The first scenario was stochastic, and was generated by No-MASS as described in Chapter 2.5. This means that the coupling was enabled to take into consideration the impact of the indoor air environmental conditions variation on the metabolic heat gains. The evolution of the metabolic heat produced by the occupants over one year was in the range [60;75] W per person . The water vapour production was kept equal to 48 g/h because it did not depend on the indoor environmental conditions (justification in Chapter 2.5). The occupancy profiles were representative of university teachers/researchers, see Figure 3.6.

In No-Mass, a seasonal effect on occupancy was implemented. This is exemplified by Figure 3.3 presenting the total heat generated per month by the occupants and the lighting throughout a year.

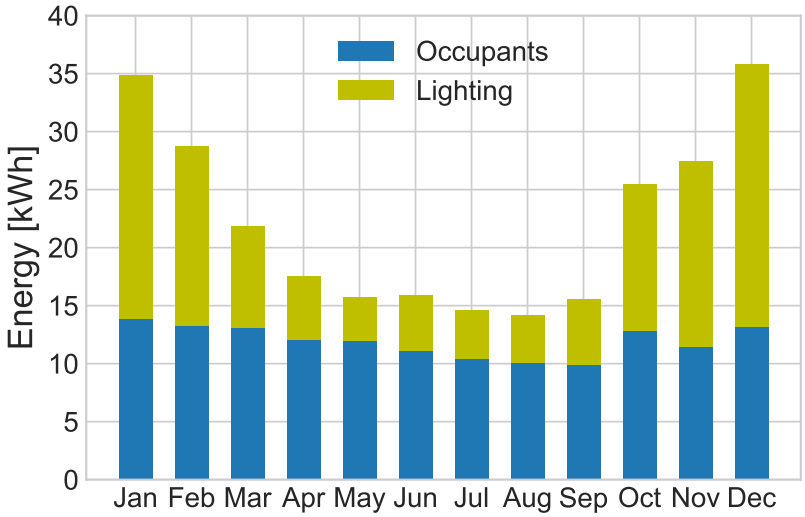

Figure 3.3 – Energy generated by the occupants and the lights over a year

First, the metabolic heat gains is lower in summer than in winter. The average energy generated by the occupants was 40.4 kWh in winter, and 30.5 kWh in summer, corresponding to a difference of approximately 32%. As the metabolic heat calculated in the standard ISO 7730 (Afnor, 2005) is a function of the temperature and the relative humidity, a higher temperature and relative humidity in summer than in winter leads to a lower overall lower heat gains.

The energy generated by the lights were approximately 4.2 times superior in winter than in summer, with an average value of 59.0 kWh for the former period and 13.9 kWh for the latter one. This was expected as we looked at sunrise and sunset hours as well as the occupants' arrival and departure hours to model the use of lights.

For this scenario, the start and stop hours of the air-conditioning system and of the computers were governed by the occupants arrival and departure hours in the office. This is illustrated in Figure 3.4.

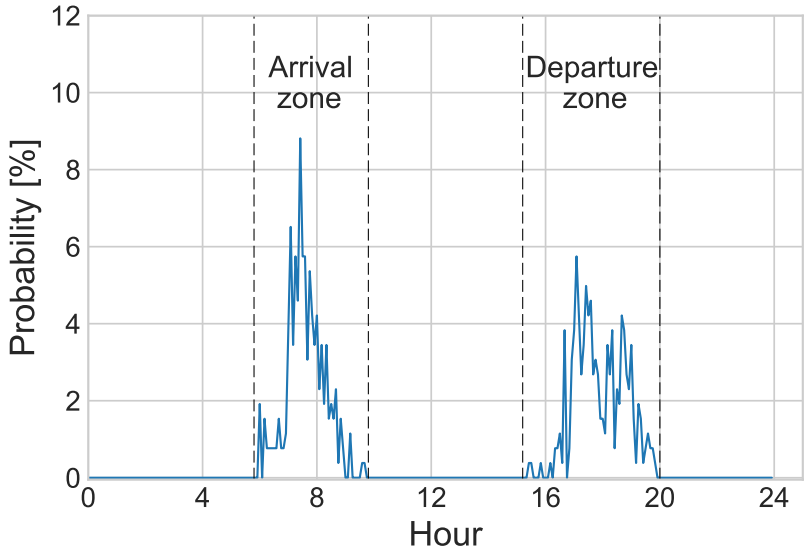

Figure 3.4 – Occupants' arrival and departure times in the office over one year

As this scenario is stochastic, the arrival hours were spread between 6:05 am and 9.55 am, with the higher probability of arrival (9%) at 7:45am. The departure hours were ranging from 3:00 pm to 7:55 pm.

3.5.2 Scenario 2: SC2 — Averaged scenario

No-MASS was run independently 850 times from the *Room model* to generate a different occupancy scenario each time. An averaged scenario was then deduced and repeated every day, except for the weekends. A high number of simulations was chosen because we wanted the scenario to follow a normal distribution. The average metabolic heat gains was then deduced by verifying the following equation at each time t:

$$\dot{Q}^{t}_{occ,SC2} = \frac{\sum_{i=0}^{N} \dot{Q}^{t}_{occ,i}}{N} \tag{3.1}$$

where $Q^{t}_{occ,SC2}$ and $Q^{t}_{occ,i}$ are the metabolic heat gains from SC2 and the i-th stochastic simulation respectively at the time t, and N corresponds to the number of stochastic simulations (850). As the metabolic heat was integrated over a year, the seasonal effect was not taken into account. The average gain was 68 W for the two occupants. The lighting and the use of computers were implemented in a similar fashion than in SC1.

For the air-conditioning system, the start and stop hours were fixed at 7:35 am and 5:25 pm respectively. These values corresponded to the average arrival and departure hours. They were deduced from Figure 3.4.

Such scenario can be labelled as a deterministic scenario derived from No-MASS.

3.5.3 Scenario 3: SC3 — Constant scenario

The constant scenario was obtained by integrating over one year the occupants' metabolic heat gains and vapour production, and the computers and lighting powers. The heat gains were obtained thanks to the following equation:

$$\dot{Q}_{SC3} = \frac{1}{t_{max}} \int_0^{t_{max}} \dot{Q}_{SC2} dt \tag{3.2}$$

where t_{max} corresponds to one year. The seasonal effect was therefore not implemented. This led to a constant 131 W heat source. The occupants represented approximately 24% of this power, meaning 31 W. The vapour production was 22 g/h. Note that the heat and vapour were continuous on every day, even during the weekends.

The start and stop hours of the air-conditioning system were the ones from SC2.

3.5.4 Scenario 4: SC4 — French code scenario

The deterministic scenario simulated is the one from the Th-BCE method proposed in the French regulation code (RT Bâtiment, 2012). This scenario is significantly different than the other three as the objective was to highlight the differences between the scenarios derived from No-MASS and the one used to size new building constructions in France. The differences with the other scenarios are listed below:

- The occupants were present from 8:00 am to 6:00 pm every day except during the weekends;
- The set point temperature for the heater were 19°C for the day and 16°C for the night;
- The set point temperature for the air-conditioner were 26°C for the day and 30°C for the night
- The lights were turned on continuously from 9:00 am to 6:00 pm (meaning when the occupant is present);
- No computers were simulated, but a heat load corresponding to the use of electrical devices was added (Figure 3.5).

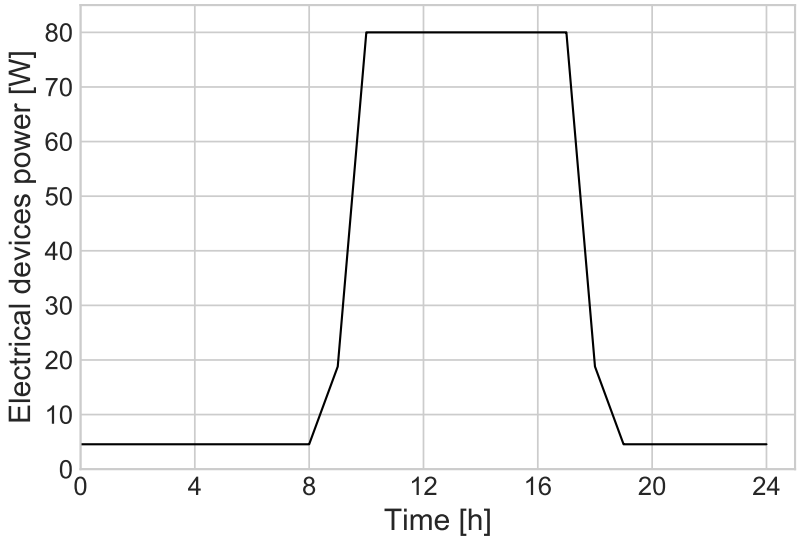

Figure 3.5 – Electrical devices heat load for the deterministic scenario

In the Th-BCE method, no humidifier is simulated. But to be homogeneous with the other scenarios, it was added here (see Table 3.4). Its set point humidity and its hysteresis were the same as the ones for SC1-3. Note that the set point temperatures for the heater and the air-conditioner were different than the ones initially put in the *Room model*. We believe that the set point temperatures indicated in the RT are not representative of a realistic regulation of offices. Temperatures of 21°C (day) and 19°C (night) for the heater and 24°C (day) for the air-conditioner seemed more plausible.

3.5.5 Summary

For illustration purpose, the four different occupancy scenario are plotted in Figure 3.6, with the metabolic heat gains corresponding to two occupants reported in the y-axis. For the stochastic scenario (top left), the graph corresponds to the occupancy profile for a random day. For SC1-3, the total metabolic gains over the year were the same. Table 3.4 lists the air-conditioning system parameters.

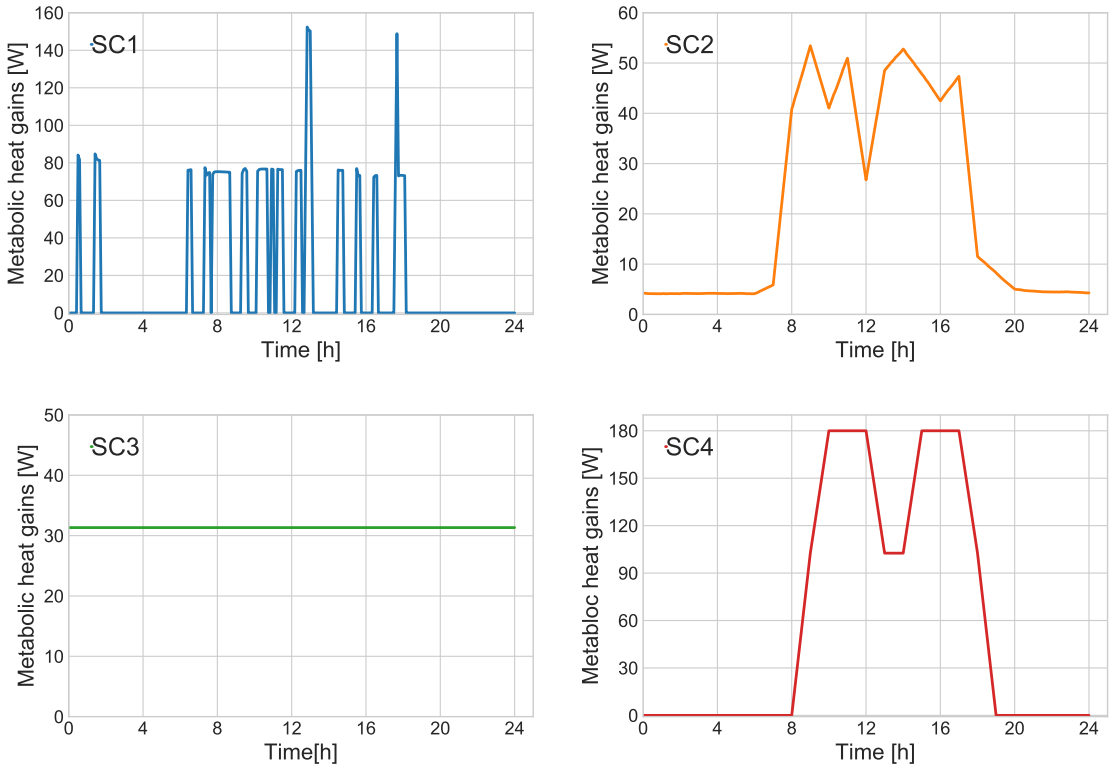

Figure 3.6 – Stochastic (top left), averaged (top right), constant (bottom left) and French code (bottom right) occupancy scenarios

		SC1-3	SC4
Set point *day/night*	Heater	21/19 ± 0.5°C	19/16 ± 0.5°C
	Humidifier	40%/OFF ± 2%	40%/OFF ± 2%
	Air-conditioner	24/OFF ± 0.5°C	26/30 ± 0.5°C
	Electrical devices (W)	300	80
	Lighting (W/m^2)	10 (at night, if occupant)	10 (working hours)
	Metabolic heat (W)	Variable (average: 68)	90
	Metabolic vapour (g/h)	48	60

Table 3.4 – Indoor sources for SC1-4

Note that the metabolic heat gain was never null for SC2. Indeed, in No-MASS, the probability of presence at night-time was implemented (while low) because the office worker or the cleaning service, for example, might work. This is also noticed in SC1 graph where an occupant was present for a short time between 12:00 am and 3:00 am. Consequently, averaging the vapour production on 850 simulations led to non-null heat and vapour productions during the night.

Since Figure 3.6 presents only the metabolic heat gains, it does not give any information on the total heat generated by the occupants, the lighting and the computers. Therefore, Figure 3.7 provides an example of the total heat gains over a random day for the stochastic scenario.

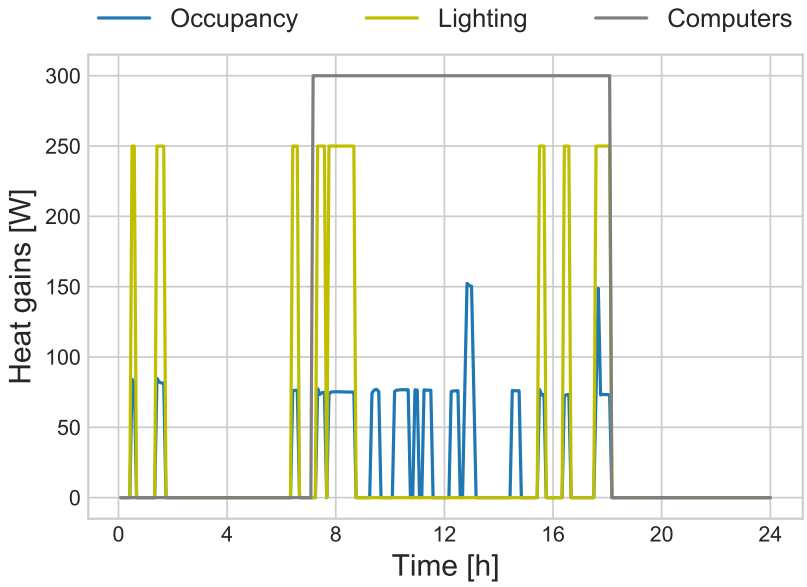

Figure 3.7 – Heat gains over a random day for the stochastic scenario

3.6 Impact on the performance indicators

This section presents a comparison of the performance indicators values for the four scenarios detailed previously.

3.6.1 Energy demand

The energy demand of the room corresponds to the one of the air-conditioning system. Details on the calculation of their power can be found in Chapter 2.4. Figure 3.8 presents the energy consumption integrated over each month for one year, and Table 3.5 summarises the energy demand in February and August for each scenario.

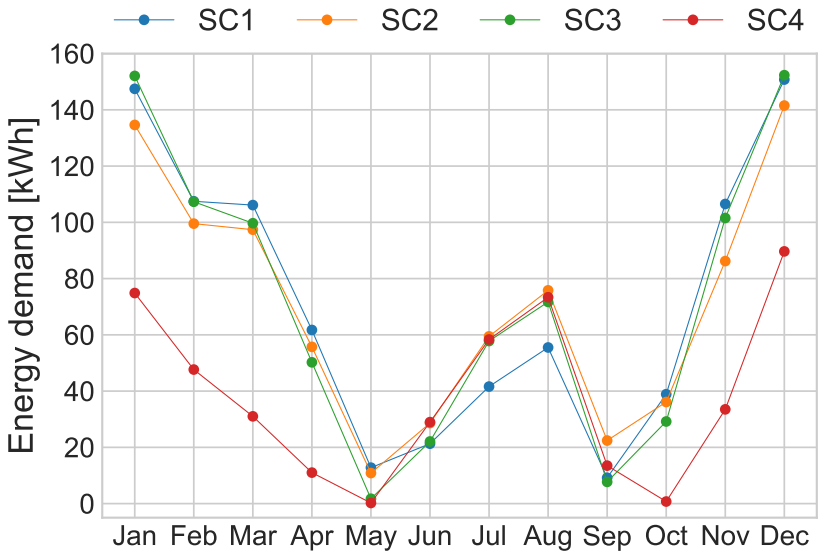

Figure 3.8 – Energy demand of the room for each occupancy scenario

		Energy demand (kWh)		
		Heater	Humidifier	Air-conditioner
SC1	*February*	101	6	—
	August	—	—	55
SC2	*February*	100	7	—
	August	—	—	76
SC3	*February*	96	4	—
	August	—	—	72
SC4	*February*	47	1	—
	August	—	—	73

Table 3.5 – Energy demand in February and in August for SC1-4

First, the simulation of Trappes climate led to a high energy demand in February (101 kWh for SC1 for example) and in August (55 kWh for SC1) due to heating and cooling needs respectively. Most of the energy demand came from the heater in February as the humidifier represented between 2 and 7% of the total energy demand during this month for SC1-3. Only the air-conditioner was turned on in August.

SC2 gave a lower energy demand than SC1 in February, but a higher one in August (+32%). While the air-conditioning system, the use of the computers and

of the lights were modelled in the same way for SC1 and SC2, the latter did not take into account the seasonal effect on occupancy. Indeed, the same occupancy scenario was repeated every day. For SC1, the occupants were slightly less present in summer than in winter, and the metabolic heat generated was lower (see Figure 3.3). Therefore, the cooling demand for SC2 was higher than the one for SC1 in summer.

For SC3, the same energy demand than for SC1 is observed in February. This scenario also led to a higher energy demand than SC1 in August. SC3 integrated the computers, the lights and the metabolic heat gains under a constant heat source. This means that the seasonal effect on occupancy was not considered. Moreover, the lighting power was smoothed throughout the year. Contrarily, SC1 lighting power was described by Figure 3.3 which highlighted an energy increase by 3.8 times in February compared to in August.

For SC4, because the set point temperatures were set to lower values compared to the ones of the other scenarios, less energy demand in February and more in August were expected. SC4 underestimated by 54% the yearly energy demand compared to SC1. Chapman et al. (2018) compared a deterministic scenario (implemented in DesignBuilder (2014) software) and No-MASS stochastic scenario for an office located in Nottingham and one in Geneva. They highlighted an underestimation of approximately 20% of the energy demand with the deterministic scenario. This comparison was similar to the one between SC1 and SC4 in our case.

Finally, the yearly energy demand is summarised in Table 3.6.

	Energy demand (kWh)				
	Heater	Humidifier	Air-conditioner		Total
			sensible	*latent*	
SC1	692	45	79	44	860
SC2	640	30	116	64	850
SC3	645	52	99	58	854
SC4	282	9	110	62	463

Table 3.6 – Yearly energy demand for SC1-4

The latent contribution of the air-conditioner corresponds to the amount of air dehumidified.

SC2 led to 7% less heating demand, 33% less humidifying demand, but 46% more

cooling demand. The same trend is observed for the heating and cooling needs of SC3 as it led to 7% less heating demand and 28% more cooling demand than SC1. The humidifying demand was however 16% higher. These results are in adequacy with the seasonal effect as SC2 and SC3 required more heating in winter and less cooling in summer than SC1. The higher humidifying demand for SC3 is discussed in the next section.

If we consider the total energy demand, SC2 and SC3 underestimated the energy demand by less than 1.5% each compared to SC1, but the seasonal effect was masked. As shown in Table 3.6, significant differences were observed between the heater, the humidifier and the air-conditioner from one case to another, but these differences are compensated when the energy demand of each system are summed. In this case, using a deterministic or a constant scenario compared to a stochastic one have almost no influence on the energy demand as long as the integrated indoor load (apart from the air-conditioning system) over the total simulation time is equal for every scenario.

3.6.2 Indoor hygric comfort

Wolkoff and Soren (2007) criterion was used for the hygric comfort of the occupants. As presented in Chapter 2.7.2, the comfort region is defined for a relative humidity between 40 and 50%. For a lower humidity the air is deemed "too dry", and for a higher one "too humid". Figure 3.9 shows the indoor relative humidity distribution over one year for each scenario in 2% humidity intervals where the abscissa represents the mean value of each interval (for example the abscissa 41 corresponds to the interval [40;42]%). Only the humidity recorded during working hours is presented in this figure as it was maintained above 38% (set point relative humidity equals to 40% with a hysteresis of 2%, see Table 3.4). Note that the humidities below 38% were not null because of the time lag when the humidifier was turned on.

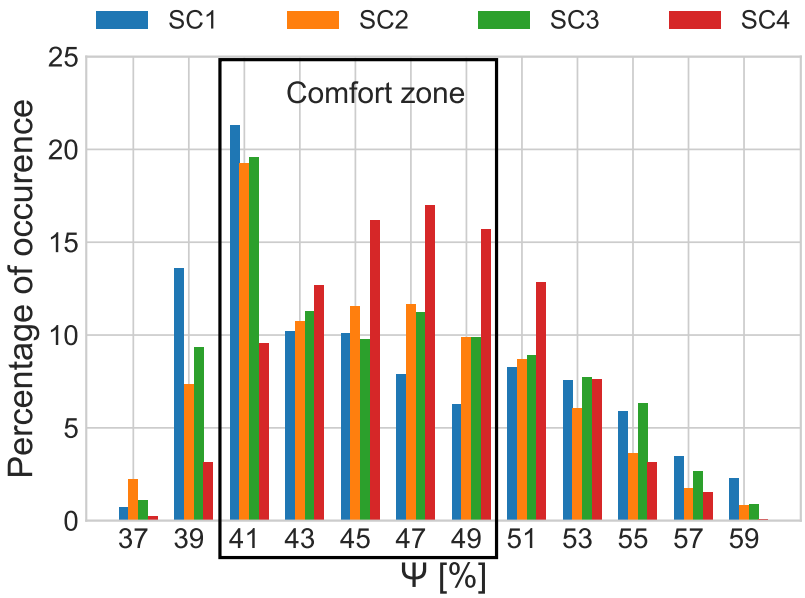

Figure 3.9 – Indoor relative humidity distribution over one year for each occupancy scenario

The time spent in the comfort zone are summarised in Table 3.7.

	[40;50]%
SC1	56.6
SC2	68.4
SC3	62.7
SC4	71.4

Table 3.7 – Time spent in the comfort zone for SC1-4

Overall, SC1 led to the lower amount of time spent in the comfort zone compared to SC2-4.

First a comparison between SC1 and SC2 is done. More time was spent in the interval [40;42]% for SC1 than for SC2, but less time in the interval [42;50]%. The humidifier energy demand was also higher for SC1 than for SC2 (see Table 3.6), and it was turned on for 104 days during the year against 91 days for SC2. The air was hence more dry for SC1, meaning that more time was spent in the interval [40;42]%. Moreover, a seasonal effect on occupancy was noticed. As the occupants were less present in summer for SC1 than for SC2, the indoor load was more significant for the latter. It engenders a higher cooling need and air dehumidification. This is noticed in Table 3.6 with a 45% higher latent energy demand. Moreover, in Figure 3.9, SC1 led to 28% time spent above 50% against 20% for SC2. Hence, SC2 led to 17%

more time spent in the comfort zone than for SC1 in summer. All in all, because of the seasonal effect on occupancy, SC2 indoor humidity distribution was smoothed throughout the year leading to almost 12% more time spent in the comfort zone than SC1.

Now SC3 and SC1 are compared. While the energy demand of the humidifier was 16% higher for SC3 than for SC1, it led to a higher prediction of the comfort range. As SC3 smoothed the metabolic vapour production, the seasonal effect on occupancy was not taken into account. Consequently, the indoor vapour load of SC3 was inferior to the SC1 one in winter, requiring more use of the humidifier. This is also translated by the fact that the humidifier was turned on 127 days for SC3 against 101 days for SC1. Finally, as for SC2, the seasonal effect on occupancy also led to 21% more time spent in the comfort zone than SC1 in summer.

SC4 led to an overall higher indoor relative humidity than SC1-3. This can be explained by two factors. Firstly, the set point temperatures for SC4 were lower in winter than the ones for SC1-3. For the same amount of water vapour produced, a lower temperature leads to a higher relative humidity. Secondly, the vapour generated by the occupants was higher (60 g/h per occupant against 48 g/h for SC1-3). This led to 71.4% of the time spent in the comfort zone.

Labat and Woloszyn (2015) compared a stochastic scenario to a constant one in a simulated dwelling where one occupant was living. They observed that using a constant moisture production scenario could lead to an increase of 10 to 20% of the comfort range (using the same comfort criterion as Wolkoff and Soren (2007)). While not of the same order of magnitude, this trend was also observed here between SC1 and SC3, as SC3 led to an increase of approximately 6% of the comfort range. In Labat and Woloszyn (2015), due to the occupant's various activities (cooking, showering, use of washing machine, ...) the water vapour production was not only metabolic, leading to an average moisture production of 82 g/h over one year. The average vapour production for the stochastic scenario in our simulated office is 22 g/h, which is approximately 3.7 times lower. This could explain the difference on indoor comfort between their case study and ours.

3.6.3 Moisture related risks

The moisture related risks were estimated by the isopleths representing the temperature and humidity couples at each time step. Limit curves defining the risk of mould growth were also added (see Chapter 2.7.3). Two isopleths were plotted for each scenario. The first one is at the interior surface of the exterior wall, because if mould growth were to appear, it could impact the occupants' health. The other one

is at the interface between the insulation material (polystyrene) and the concrete because humidity is more subjected to be accumulated here, which could lead to thermal and/or structural issues.

The equations of the plaster limit curves are given below. For the polystyrene, it was assumed that mould growth would appear only for a relative humidity above 95% (Johansson et al., 2013).

$$\Psi = a + c(T^2 - 54T) \tag{3.3}$$

with:

$$c = (0.89 - 0.95) / \left[T_1^2 - T_2^2 - 54(T_1 - T_2)\right] \tag{3.4}$$

and:

$$\begin{aligned} a &= \begin{cases} 0.89, & \text{lower curve} \\ 0.95, & \text{upper curve} \end{cases} \\ T_1 &= 22°\text{C} \\ T_2 &= 10°\text{C} \end{aligned} \tag{3.5}$$

The results are presented in Figure 3.10 and 3.11. For clarity sake, SC4 was plotted separately from SC1-3.

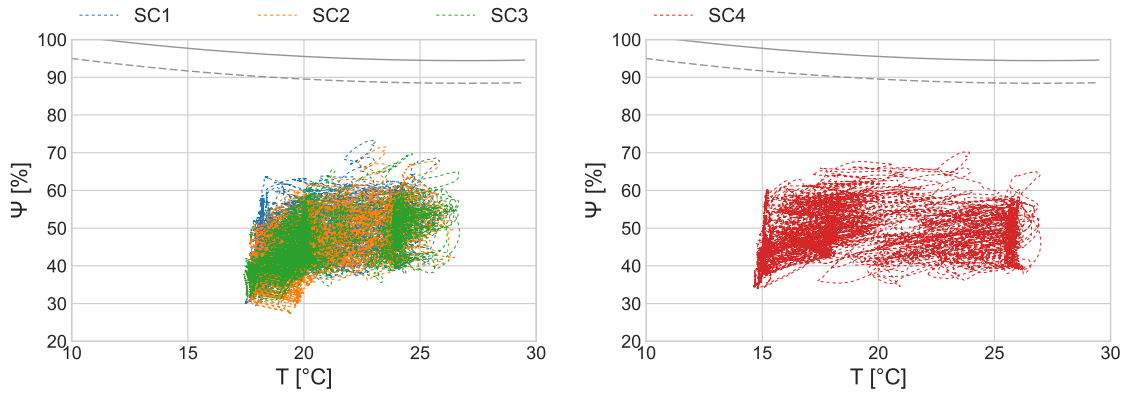

Figure 3.10 – Isopleth at the surface of the exterior wall for SC1-3 (left) and SC4 (right)

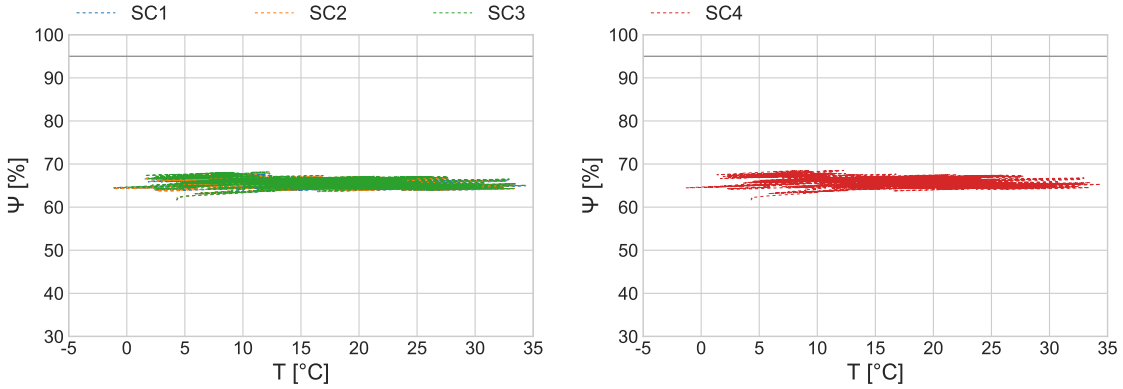

Figure 3.11 – Isopleth at the interface between the polystyrene and the concrete for SC1-3 (left) and SC4 (right)

All of the scatter plots are well below the limit curves, meaning that no risk of mould growth exists for any scenario. Additionally, SC1-3 isopleths are very close to each other. Note that because of these small deviations, SC1 plot is masked by SC2-3 in Figure 3.11. Figure 3.10 also confirmed the results from Figure 3.9 which presented a similar humidity distribution for SC1-3. For SC4, the larger spread of the isopleth at the surface was due to the different set point temperatures defined.

At the interface between the polystyrene and the concrete, the temperature is spread from -1°C to 33°C. Because of the relatively high thermal conductivity of concrete (2 $W/(m.K)$), this zone was largely influenced by the exterior environmental conditions. This also explained why SC4 gives similar results than SC1-3. The humidity did not vary much since the concrete has a relatively low vapour permeability, most of the vapour flux was compensated by the first centimetres of the material.

Additionally, another way to verify if condensation were to happen within the exterior wall is to look at the evolution of the water vapour pressure compared to the saturated water vapour pressure. At each node, the minimum pressure difference over one year was calculated, and is reported in Figure 3.12.

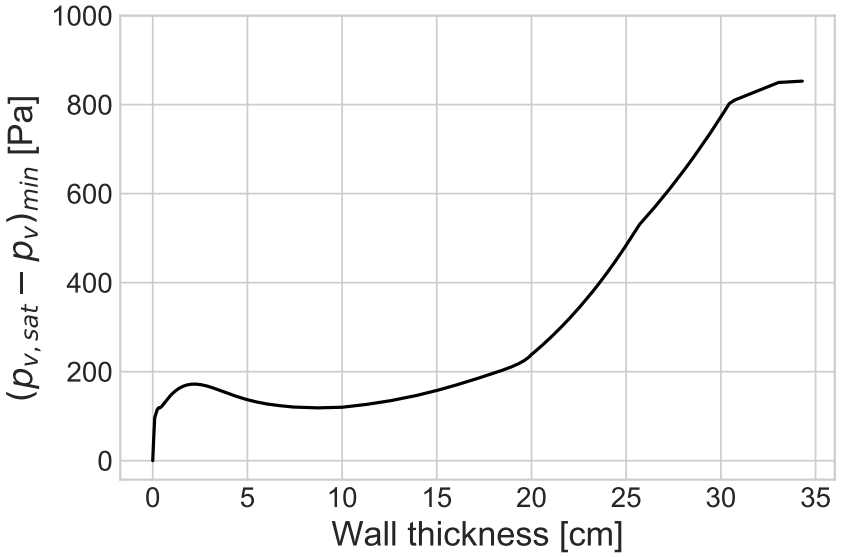

Figure 3.12 – Difference between $p_{v,sat}$ and p_v through the exterior wall

The difference is always positive meaning that no condensation occurred in the wall. The same results were obtained for SC2-4 (not presented here).

Finally, because the humidity was well below the limit curves, the threshold value initiating mould growth was not reached. Therefore, it was not deemed necessary to use the VTT model (presented in Chapter 2.7.3).

3.7 Summary and conclusion

Global performance indicators on the energy demand and the hygric comfort were already discussed in their related section. They are summarised in Table 3.8.

Scenario	Energy demand (kWh)				Hygric comfort (%)
	Heater	Humidifier	Air-conditioner	Total	
SC1	692	45	123	860	56.6
SC2	640	30	180	850	68.4
SC3	645	52	157	854	62.7
SC4	282	9	172	463	71.4

Table 3.8 – Yearly performance indicators

This chapter aimed at proposing an estimation of the occupancy scenario influence on the hygrothermal performance of a room. To do so, 4 scenarios representative of the modelling approaches available in the literature were simulated: a

stochastic occupancy scenario, an averaged one (similar to a deterministic scenario), a constant one and additionally the French regulation code scenario (RT Bâtiment, 2012). The hygrothermal performance of the room was defined by the three performance indicators introduced in Chapter 2.7: the energy demand, the indoor hygric comfort and the moisture related risks.

It was shown that the occupancy scenario had almost no influence on the global energy demand. However, deviations were observed on the energy demand on each system from one scenario to another. While the differences were not very pronounced on the heating demand (maximum of 7%), they were more significant on the humidifying and the cooling needs, reaching as much as 46%, and highlighting a non negligible impact of the occupancy scenario.

On the indoor hygric comfort, the constant scenario and the averaged one led to an overestimation of the comfort range of approximately 12% and 6% respectively compared to the stochastic scenario. These differences were explained by a seasonal effect engendering a different regulation on the air-conditioning system.

The French regulation code (RT Bâtiment, 2012) scenario was considered to be separate from the other three because the set point temperature and the simulation of equipments were different. Still, it gave a comparison with the code overseeing new building constructions in France. It led to an underestimation of the energy demand of approximately 54% and a overestimation of the hygric comfort prediction of 15% for this specific case.

No moisture related risks were observed, but Trappes climate is temperate. The indoor relative humidity was almost always inferior to 70% throughout the year.

To conclude, the occupancy scenario impact on the performance indicators (except for the moisture related risks) is strongly dependent on the scale at which we analyse the results. At year scale, its influence on the energy demand was negligible and the indoor hygric comfort was moderately impacted. But at seasonal scale, the impact was much more pronounced: the seasonal effect was smoothed by the averaged and constant scenarios compared to the stochastic one. For example differences up to 46% on the cooling demand and up to 21% on the time spent in the comfort zone in summer exist from one scenario to another. We are interested in seasonal scales ; therefore, we favoured the stochastic occupancy scenario to estimate the walls moisture buffering capacity.

Chapter 4

Impact of the walls moisture buffering on the performance indicators

Contents

4.1 Methodology

This chapter aims at answering the third objective established in Chapter 1: proposing an estimation of the walls moisture buffering effect on the hygrothermal performance of a room.

To do so, a room was simulated and exposed to three different climate: a temperate climate (in Trappes), a sub-tropical one (in Hong Kong) and a continental one (in Toronto). To emphasise the moisture buffering effect, a hygroscopic plaster was selected and applied on the interior surface of the walls, covering a part of their surface. A comparison with a reference case study (without hygroscopic plaster applied) gave an estimation of the capacity of a hygroscopic plaster to dampen the humidity in a room subjected to realistic solicitations.

Details on the cases studied are presented in Section 4.1.1. Section 4.1.2 lists the hygroscopic plaster hygrothermal properties. Results on the performance indicators are presented in Section 4.2.

4.1.1 Case study

Three configurations corresponding to an office were studied. For all of these configurations, two occupants were working in the office.

The first configuration was the one simulated in Chapter 3.2 and is reminded here. It corresponded to an office of dimensions 5 $m\times$ 5 $m\times$ 2.5 m. One wall made of 200 mm of concrete, 13 cm of polystyrene and 1.3 cm of gypsum board faced the South. The office was surrounded by other offices which indoor temperature and relative humidity evolved in the same way as the ones in the simulated office. The separating walls were made of two 1.3 cm thick gypsum boards with 6 cm of polystyrene in between. The floor and ceiling were made of 20 cm of concrete. A vapour resistance $Sd = 0.5\ m$ was added to all the walls to simulate a conventional interior coating. No coating was added on the exterior surface. It is reminded that no window was simulated in this work. Since no plaster was added on the interior surface of the walls, this case study will be referred to P_0.

The second room configuration was similar to the first one except that an earth plaster was added on the wall facing the South. The surface covered by the earth plaster corresponded to 12.5% of the total surface of the walls. The thickness of the plaster was 2 cm. This case study will be referred to $P_{12.5}$.

The third room configuration was also similar to the first one, but this time the 2 cm thick earth plaster was added to all of the separating walls. The surface covered by the earth plaster corresponded to 37.5% of the total surface of the walls. This

case study will be referred to $P_{37.5}$.

P_0 was previously described in Chapter 3 (see Figure 3.2). Figure 4.1 illustrates $P_{12.5}$ and $P_{37.5}$.

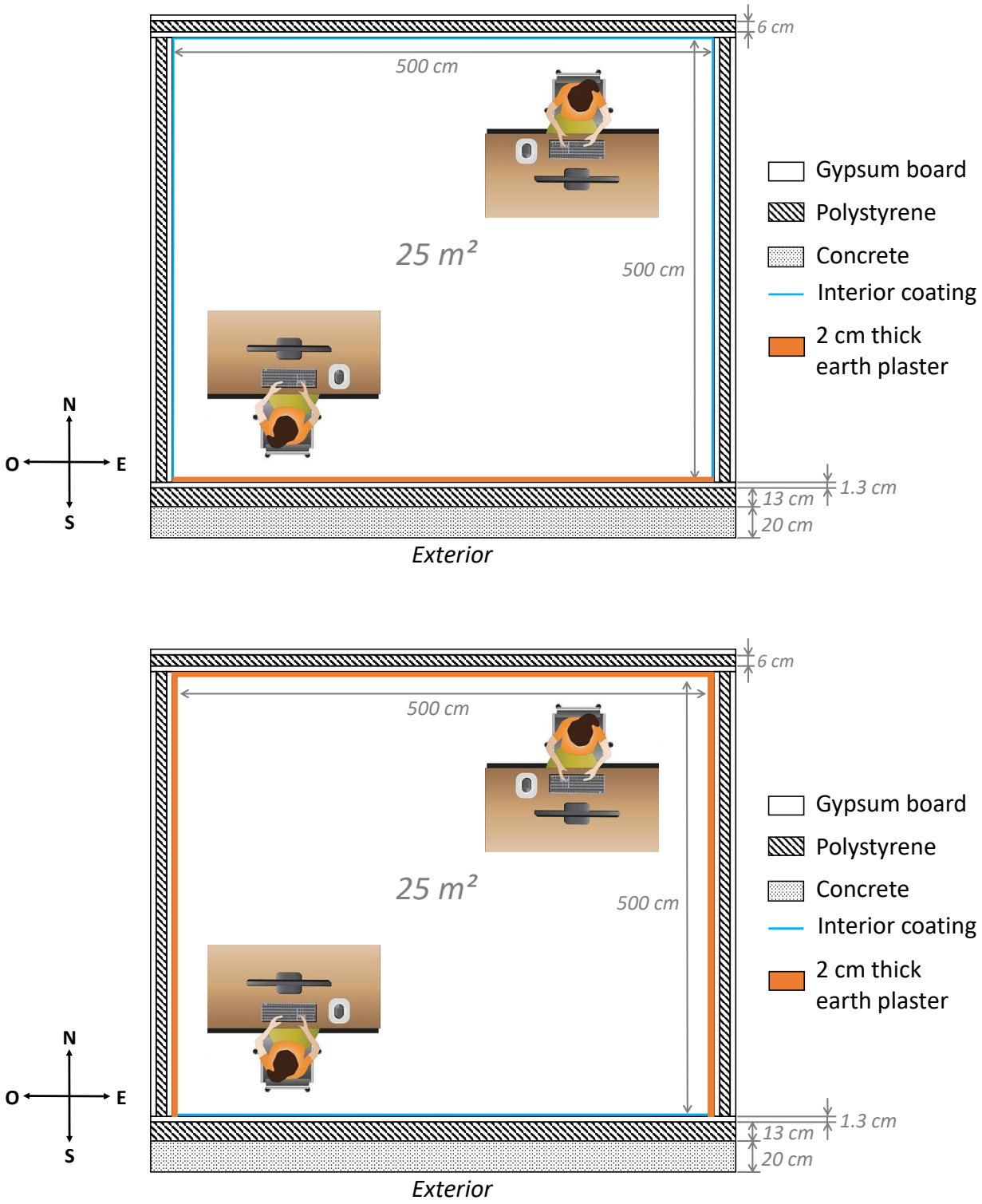

Figure 4.1 – 2D representation of $P_{12.5}$ (top) and $P_{37.5}$ (bottom)

In order to assess the behaviour of the walls towards humidity under mild and more extreme environmental conditions, three different climates were selected:

- Temperate climate in Trappes (France);
- Humid subtropical in Hong Kong (China);
- Continental in Toronto (Canada).

Table 4.1 presents the average temperature and vapour pressure in summer and winter for each climate. Additionally, Appendix B gives the temperature and vapour pressure evolution over one year.

	T (°C)		p_v (Pa)	
City	*summer*	*winter*	*summer*	*winter*
Trappes	19.1	6.1	1510	859
Hong Kong	28.4	16.5	3153	1413
Toronto	19.4	-4.7	1583	378

Table 4.1 – Average temperature and vapour pressure in summer and winter for the climate of Trappes, Hong Kong and Toronto

Trappes climate is characterised by mild temperatures and average vapour pressure. In comparison, Hong Kong climate is warmer and much more humid, especially in summer when the vapour pressure is more than twice the one in Trappes. Toronto summer is similar to the one in Trappes, but has much colder and dryer winter as the vapour pressure was more than 2 times inferior to the one in Trappes.

4.1.2 Materials

As this work does not focus on evaluating the performance of different plasters toward the indoor humidity, only one hygroscopic plaster was selected, which hygrothermal properties are given in given in Tables 4.2, 4.3 and 4.4. They are representative of a 2 *cm* thick earth plaster (Mcgregor et al., 2009).

ρ	k	C_p	$\delta_v \cdot 10^{-11}$
(kg/m^3)	$(W/(m.K))$	$(J/(kg.K)))$	(s)
1660 [(1)]	0.57 [(2)]	800 [(2)]	1.97 [(1)]

Table 4.2 – Earth plaster hygrothermal properties

[(1)] (Mcgregor et al., 2009)
[(2)] (Laborel-Préneron et al., 2018a)

Ψ (%)	23	43	59	75	85	97
w (kg/m^3)	3.77	5.74	7.42	10.20	13.70	31.76

Table 4.3 – Earth plaster sorption properties (Mcgregor et al., 2009)

w (kg/m^3)	12	28	32
δ_l (s)	10^{-17}	10^{-15}	10^{-14}

Table 4.4 – Earth plaster liquid water permeability (assumption — no value available)

No liquid permeability values were available in the literature. Consequently, the one corresponding to a highly porous material was selected in (Evrard, 2008). This permeability corresponds to a hemp concrete one.

The properties of the other materials subjected to the indoor ambience (namely the gypsum board and the concrete) were already given in Chapter 3.

In order to get a first estimation of the behaviour of each materials towards humidity, the calculation of the theoretical MBV (MBV_{ideal}) based on Eq. (1.1) is given in Table 4.5. The theoretical moisture penetration depth $d_{p,1\%}$ calculated in accord with Eq. (1.4) is also added.

Material	ξ (kg_v/kg_{mat})	b_m $(kg/(m^2.Pa.s^{1/2}))$	MBV_{ideal} $(g/(m^2.\%))$	$d_{p,1\%}$ (cm)
Concrete	$2.44 \cdot 10^{-2}$	$1.48 \cdot 10^{-7}$	0.69	0.6
Gypsum board	$5.96 \cdot 10^{-3}$	$2.32 \cdot 10^{-7}$	1.09	9.8
Earth plaster	$7.81 \cdot 10^{-3}$	$3.02 \cdot 10^{-7}$	1.41	5.0

Table 4.5 – Theoretical MBV and moisture penetration depth of the concrete wall, the gypsum board and the earth plaster

Compared to the other two materials, the moisture buffering capacity of the earth plaster is higher. According to the MBV classification defining the performance of a material (Rode et al., 2005), it belongs to the "good" class like the gypsum board, while the concrete wall belong to the "moderate" class. Therefore, it was expected that the earth plaster would have an impact on the room indoor humidity.

The moisture penetration depth of concrete is relatively low compared to the other two materials, meaning that most of vapour transfer happens in the first millimetres of the wall. The ratio penetration depth over thickness is equal to 7.5 for the gypsum board and 2.5 for the earth plaster. It is therefore expected that the 1.3 *cm* thick gypsum board would dampen less humidity than the 2 *cm* thick earth plaster.

4.1.3 Indoor sources

The indoor sources were depicted by the occupants' presence and activities and the air-conditioning system. The occupants' presence and activities were simulated in a stochastic way by using No-MASS (see Chapter 3 for justification) in accord with the methodology presented in Chapter 2.

A mass and energy balance under constant conditions led to the power, vapour production and air flow rate presented in Table 4.6. Note that an air-conditioner in Toronto and a humidifier in Hong Kong are usually not needed because of their relatively cold and humid climate respectively. These equipments were still modelled in our approach to be homogeneous between the three case studies.

City	Heater (W)	Humidifier (kg_v/h)	Air-conditioner (kg_a/s)
Trappes/Toronto	1500	0.35	0.1
Hong Kong	1000	0.35	0.1

Table 4.6 – Sizing of the air-conditioning system for the Trappes, Hong Kong and Toronto climates

The same heating power and humidifier vapour production than the ones for Trappes climate were used for Toronto climate. The simulations results showed that these values were sufficient to regulate the indoor temperature and relative humidity at the selected set points. Hong Kong led to a lower heating power because of its relatively warm climate.

4.2 Results and discussion

The three climates studied in this chapter are significantly different. Hence, results on the performance indicators are presented for each climate separately while paying a particular attention to walls the moisture buffering capacity.

4.2.1 Temperate climate (Trappes)

4.2.1.1 Energy demand

Results on the energy demand for Trappes climate are presented in Figure 4.2.

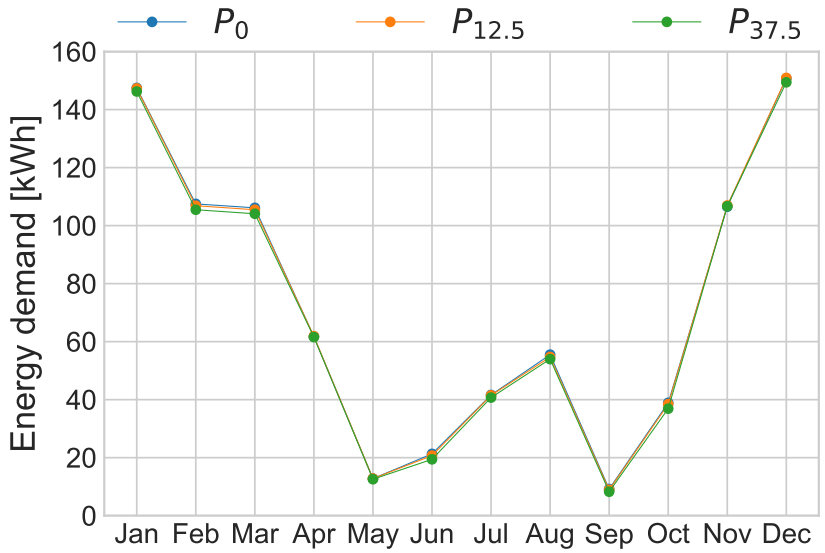

Figure 4.2 – Energy demand of the room for Trappes climate

Few deviations were observed between P_0, $P_{12.5}$ and $P_{37.5}$ (see Table 4.7), meaning that the earth plaster had a negligible influence on the energy demand of the room.

	Energy demand (kWh)				
	Heater	Humidifier	Air-conditioner		Total
			sensible	*latent*	
P_0	692	45	79	44	860
$P_{12.5}$	690	45	77	44	856
$P_{37.5}$	682	45	75	43	845

Table 4.7 – Energy demand of the room decomposed by equipment for Trappes climate

As shown in Chapter 3, most of the energy demand came from the heater and the air-conditioner. For each case, the heater represented approximately 80% of the total energy demand, the humidifier 5% and the air-conditioner 15%. As the humidifier energy demand was identical for each case, the slight decrease in energy demand for $P_{12.5}$ and $P_{37.5}$ was due to the earth plaster adding a thermal resistance to the walls.

4.2.1.2 Moisture buffering effect of the walls

In order to highlight the moisture buffering effect of the walls, we chose to focus on only one week. For Trappes climate, the first week of June was selected as signifi-

cant variations of the exterior water vapour pressure were observed. Its evolution in the room is presented in Figure 4.3 for each case (P_0, $P_{12.5}$ and $P_{37.5}$). The exterior water vapour pressure variations were also added.

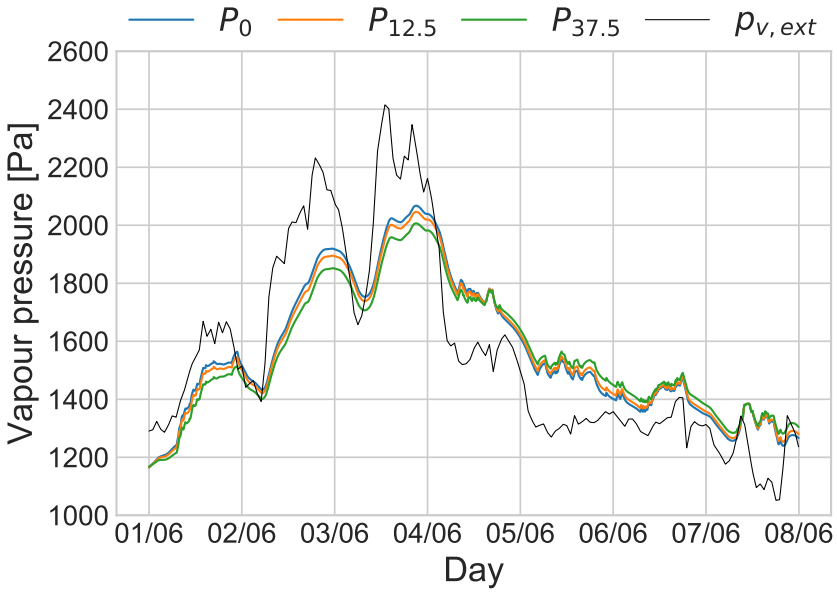

Figure 4.3 – Exterior and interior vapour pressure evolution during the first week of June for Trappes climate

Additionally, Figure 4.4 gives the relative humidity variations related to the differences in water vapour pressure observed in Figure 4.3.

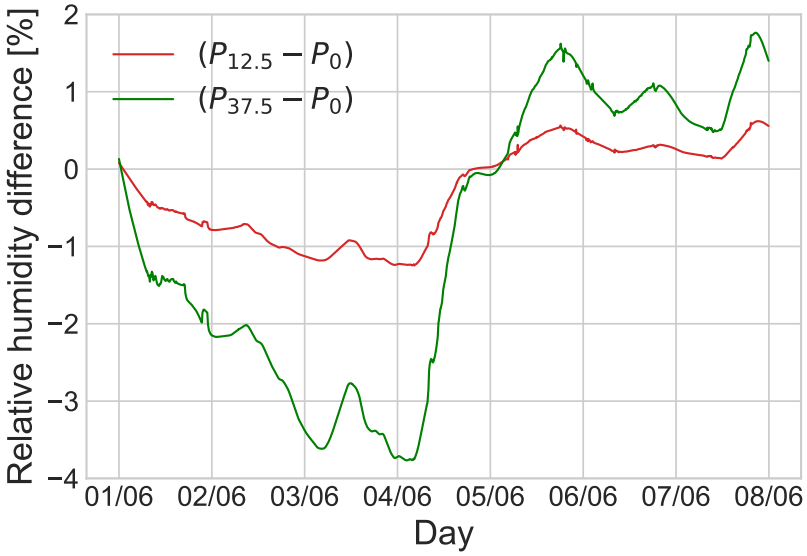

Figure 4.4 – Evolution of the indoor relative humidity difference between $P_{12.5}$ and P_0, and $P_{37.5}$ and P_0 for the first week of June for Trappes climate

The first general observation is that the more the surface is covered by the earth plaster, the more the vapour pressure is dampened. This is especially true on June 3 when the maximum vapour pressure reduction was 26 and 69 Pa compared to the reference case, for $P_{12.5}$ and $P_{37.5}$ respectively. This corresponds to a dampening of 1.2% and 3.8% of relative humidity respectively. This trend is in adequacy with the MBV of the earth plaster being higher than the gypsum board one.

Moreover, after midday on June 4, the indoor vapour pressure and relative humidity of $P_{12.5}$ and $P_{37.5}$ became higher than ones of P_0, leading to an increase of relative humidity by 0.6 and 1.6% respectively. This was due to the exterior vapour pressure being lower than the interior one. The ventilation hence removed humidity which was compensated by desorption in the walls.

Additionally, the water vapour fluxes were integrated on each day. Results are presented in Figure 4.5. It is reminded that the indoor air balance is composed of four terms: the vapour exchange with the walls $\dot{m}_{walls}$, the vapour transfer due to the ventilation $\dot{m}_{ventil}$, the indoor sources $\dot{m}_{so}$ and the hygric capacity of the air ξ_{air}:

$$\dot{m}_{walls} + \dot{m}_{ventil} + \dot{m}_{so} - \xi_{air} = 0 \tag{4.1}$$

A distinction was done between the positive and negative fluxes. This is translated by Eq.(4.2) for a flux $\dot{m}_i$ integrated on one day:

$$\dot{m}_{d,i} = \begin{cases} \frac{1}{t_{max}} \int \dot{m}_i H(\dot{m}_i) dt & \text{if } \dot{m}_i > 0 \\ \frac{1}{t_{max}} \int \dot{m}_i H(-\dot{m}_i) dt & \text{else.} \end{cases} \tag{4.2}$$

where $\dot{m}_{d,i}$ is the integrated flux i on one day (g/h), t_{max} is equal to 24 hours, and H is the Heaviside step function. It is defined by Eq. (4.3):

$$H(x) = \begin{cases} 1 & \text{if } x > 0 \\ 0 & \text{if } x < 0 \end{cases} \tag{4.3}$$

In Figure 4.5, the integrated fluxes are presented for P_0. As no significant differences were noticed for $P_{12.5}$ and $P_{37.5}$ compared to P_0, their associated graphs are given in Appendix C.1. Note that the hygric capacity of the air is pondered by a negative sign in Eq. (4.1), meaning that it is plotted as a negative value in Figure 4.5, so that the positive and negative fluxes are balanced.

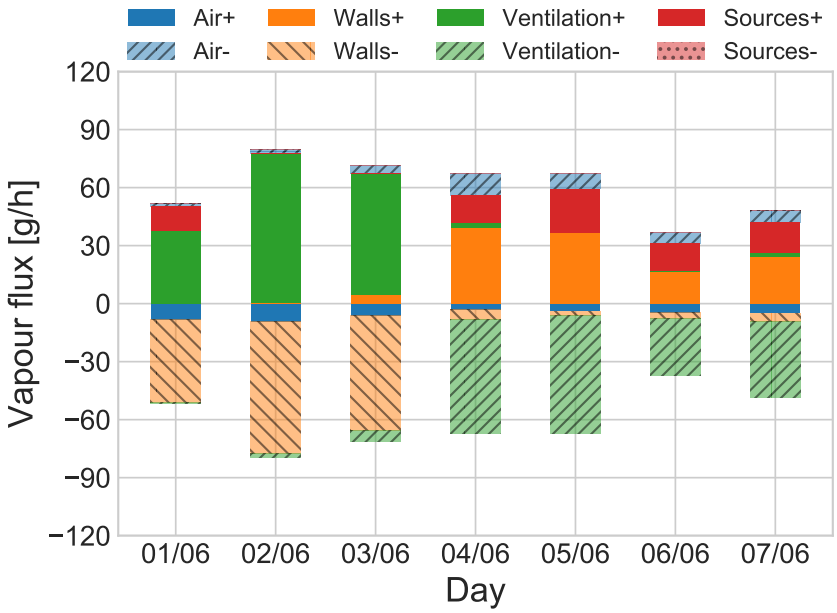

Figure 4.5 – Vapour fluxes representation for P_0 for Trappes climate

From June 1 to the June 3, the exterior vapour pressure was higher than the interior one, meaning that the ventilation brought moisture into the indoor environment, which was partially absorbed by the walls. Moreover, moisture was also generated by the occupants on June 1 (June 2 and June 3 corresponded to a weekend). This moisture intake was absorbed by the walls and contributed to the increase of humidity in the room. For example on June 2, 90% of the vapour was absorbed by the walls and 10% contributed to increase the indoor humidity.

Starting from June 4, the exterior vapour pressure became lower than the interior one. This led to a removal of moisture through the ventilation system. Therefore, the walls released moisture in the air due to desorption. For example, in June 5, 54% of the vapour was released from the walls, the sources brought 34% and approximately 12% contributed to the decrease of humidity.

Now the influence of the earth plaster is discussed. The water vapour exchanged with the walls for each case is presented in Figure 4.6. The fluxes were calculated in accord with Eq. (4.2).

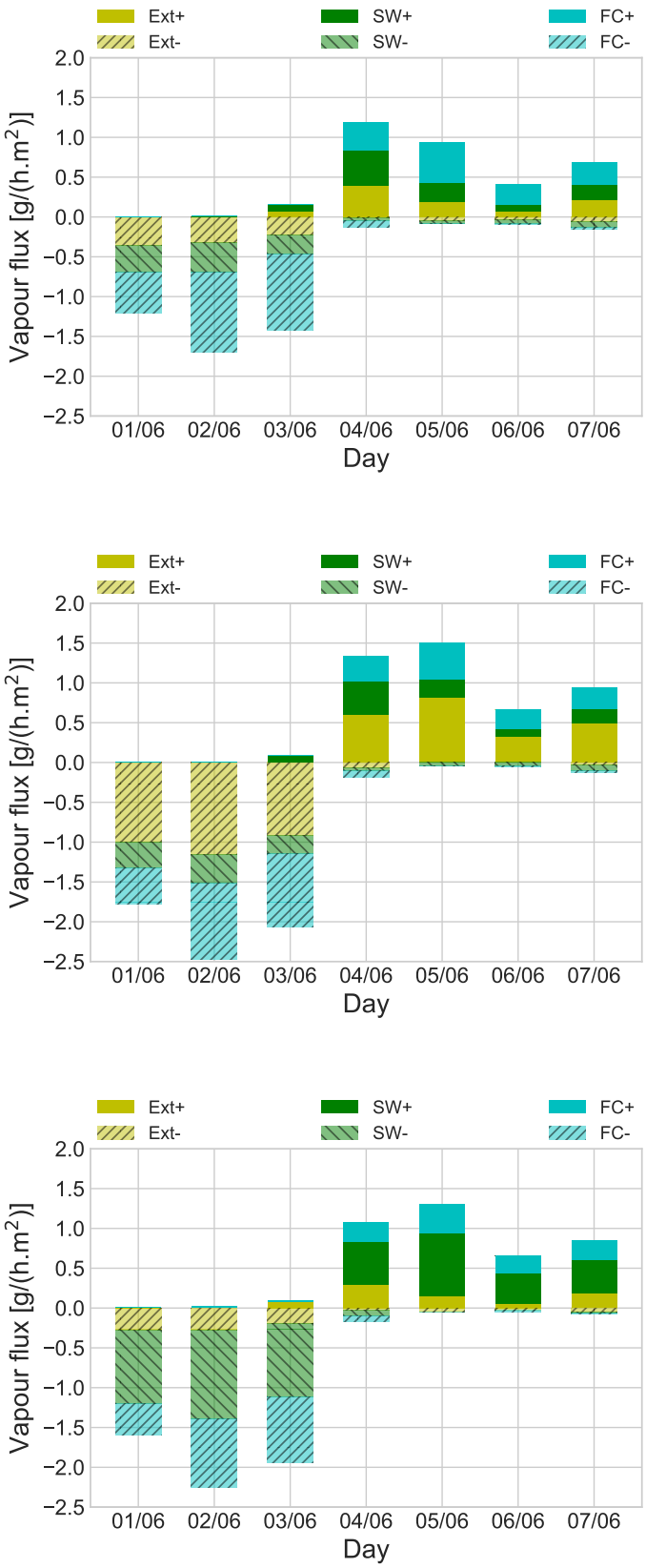

Figure 4.6 – Vapour exchanged with the walls for P_0, $P_{12.5}$ and $P_{37.5}$ (from top to bottom) for Trappes climate

Table 4.8 gives the positive and negative amount of vapour exchanged with the walls divided by the surface of the corresponding wall for each case, $\phi_{tot,i}$ (g/m^2). The calculation relied on Eq. (4.4):

$$\phi_{tot,i} = \frac{1}{A_i} \int_0^{t_{max}} |\dot{m}_{d,i}| dt \tag{4.4}$$

where A_i is the surface of the wall i (m^2), subscripts i corresponds to the exterior wall, the separating walls, or the floor and ceiling, $\dot{m}_{d,i}$ is calculated with Eq. (4.2) and t_{max} is equal to 168 hours (1 week). The amount of vapour is also given. It is calculated with Eq. (4.5):

$$m_{tot,i} = A_i \cdot \phi_{tot,i} \tag{4.5}$$

In Table 4.8, only the total masses exchanged over the whole week are presented for clarity sake. Subscripts + and − refers to a positive and negative masses respectively.

	ϕ_{tot} $(g/(m^2))$			m_{tot} (kg)
	Exterior wall	*Separating walls*	*Floor and ceiling*	
P_{0+}	22.4	25.2	34.0	2.9
P_{0-}	25.1	27.6	61.9	4.4
Total	**47.5**	**52.8**	95.9	**7.3**
$P_{12.5+}$	54.1	23.8	31.5	3.1
$P_{12.5-}$	75.9	26.5	58.8	4.9
Total	**130.0**	50.3	90.3	**8.0**
$P_{37.5+}$	18.7	50.8	26.8	3.5
$P_{37.5-}$	21.7	72.7	52.9	5.6
Total	40.4	**123.5**	79.7	**9.1**

Table 4.8 – Vapour exchanged with the walls for P_0, $P_{12.5}$ and $P_{37.5}$

First, it is observed that the mass exchanged with the walls for $P_{12.5}$ and $P_{37.5}$ was more significant than for P_0 by 9 and 24% respectively. These results can also be noticed if we look at the exchanges between the indoor air and each wall.

The differences in vapour exchanged with the exterior wall between P_0 and $P_{12.5}$ are firstly discussed. Because a plaster was applied on the exterior wall, the total mass exchanged with its surface was 47.5 g/m^2 for P_0 and 130.0 g/m^2 for $P_{12.5}$, meaning 2.7 times more. The same trend is observed when comparing the mass exchanged with the separating walls between P_0 and $P_{37.5}$ as it was multiplied by

2.3 for the latter. This is explained by the 30% higher hygric capacity of the earth plaster compared to the gypsum board one (see Table 4.5). This means that the earth plaster absorbs or desorbs more humidity when it is subjected to humidity variations.

A slight decrease in the total flux exchanged with the floor and ceiling is observed for $P_{12.5}$ and $P_{37.5}$ compared to P_0 because most of the exchange happened between the indoor air and the earth plaster.

Note that for each case, the vapour exchanged with the floor and ceiling (in concrete) was always higher than with the wall in gypsum board. The concrete has a moisture penetration depth of 0.6 cm (see Table 4.5) while the gypsum board one is 9.8 cm. Because the gypsum boards were only 1.3 cm thick, most of the moisture went through it, whereas the concrete absorbed it as it was 20 cm thick. Moreover, for the case study simulated, no high moisture production due to the indoor sources occurred in the room as the occupants only generated 48 g/h per occupant (see Chapter 2). Therefore, under long solicitations, the high hygric capacity of the concrete was predominant. Figure 4.6 confirms this result: during the June 2 and 3 when no moisture sources occurred, most of the vapour was exchanged with the floor and the ceiling for P_0.

4.2.1.3 Indoor hygric comfort

As in Chapter 3, the comfort zone is presented in Figure 4.7 with the percentage of occurrence of 2% relative humidity intervals over a year. The indoor comfort zone is defined by the [40;50]% relative humidity interval based on Wolkoff and Soren (2007) criterion. Only the values of indoor relative humidities obtained when the occupants were present were used to plot Figure 4.7.

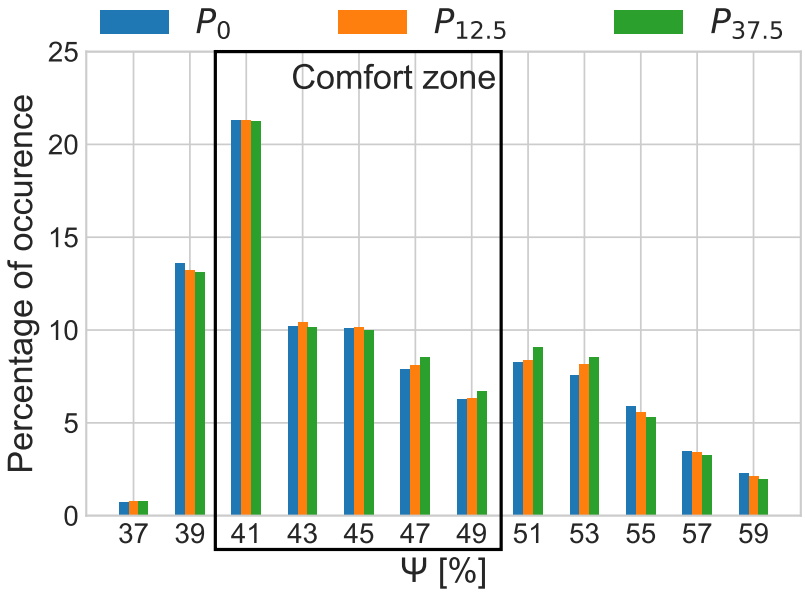

Figure 4.7 – Yearly indoor relative humidity distribution for Trappes climate

Slight differences are observed between P_0, $P_{12.5}$ and $P_{37.5}$ despite the fact that we previously showed the influence of the earth plaster buffering capacity on the indoor relative humidity. For the three cases, the time spent in the comfort zone was respectively 56.6%, 57.2% and 57.5%.

However, while the differences were not significant at year scale, the previous section still highlighted the earth plaster impact on the vapour fluxes. Therefore, the indoor comfort might be improved at smaller time scales. The months of February and May were hence investigated as they are representative of a typical cold and dry, and hot and humid months respectively. Results are shown in Figure 4.8.

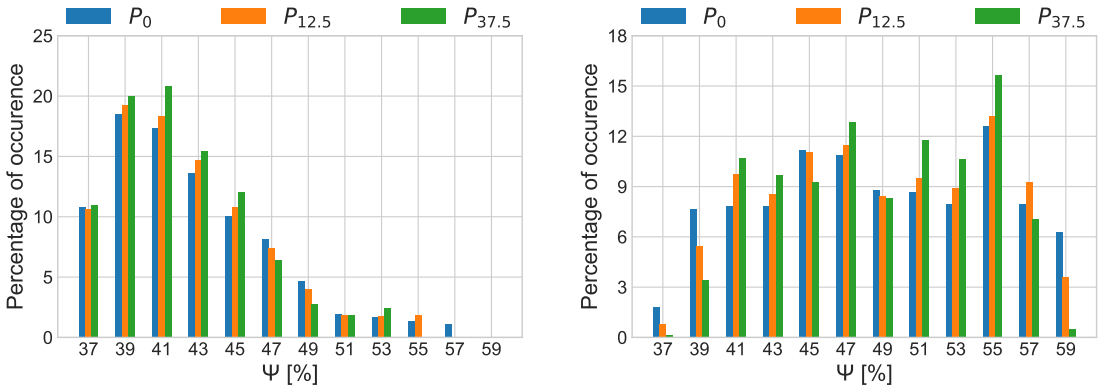

Figure 4.8 – Indoor relative humidity distribution for Trappes climate — months of February (left) and May (right)

In February, $P_{12.5}$ and $P_{37.5}$ led to more comfortable indoor conditions compared to P_0. As this month is relatively dry, the earth plaster released moisture in the

indoor environment leading to an increase of humidity.

In May, the moisture released by the walls was also highlighted for humidities ranging from 40 to 55%. Significant differences between the three case studies are noticed for the interval [58,60]% in which P_0 led to 6.3% of the time spent in this interval while $P_{37.5}$ led to 0.5%.

Table 4.9 presents the prediction of the comfort range for each case in February and May.

	[40;50]%	
	February	May
P_0	53.8	46.6
$P_{12.5}$	55.1	49.2
$P_{37.5}$	57.4	50.8

Table 4.9 – Prediction of the indoor relative humidity distribution in the comfort interval for P_0, $P_{12.5}$ and $P_{37.5}$ in February and May

The overall trend is that $P_{12.5}$ and $P_{37.5}$ improved the indoor hygric comfort, with a maximum of 4.2% more time spent in the comfort zone for $P_{37.5}$ in May, compared to P_0. However, this improvement is not significant. One has to keep in mind that Trappes climate is temperate and the metabolic vapour production was relatively small compared to what is usually found in the literature (see Chapter 1, Table 1.2). More solicitations in terms of humidity might lead to bigger discrepancies between the case studies.

4.2.1.4 Moisture related risks

The moisture related risks were already investigated in Chapter 3 for P_0. The isopleths at the surface of the exterior wall and at the interface between the concrete were plotted (Figures 3.10 and 3.11). No mould growth was predicted for this case. Moreover, the threshold relative humidity which triggers mould growth is 80% according to Nielsen (2003) and Ojanen et al. (2010). As the relative humidity of the walls surface for $P_{12.5}$ and $P_{37.5}$ was always below 75%, it was not deemed necessary to investigate the moisture related risks for these cases.

4.2.2 Sub-tropical climate (Hong Kong)

4.2.2.1 Energy demand

The energy demand of the room located in Hong Kong is presented in Figure 4.9.

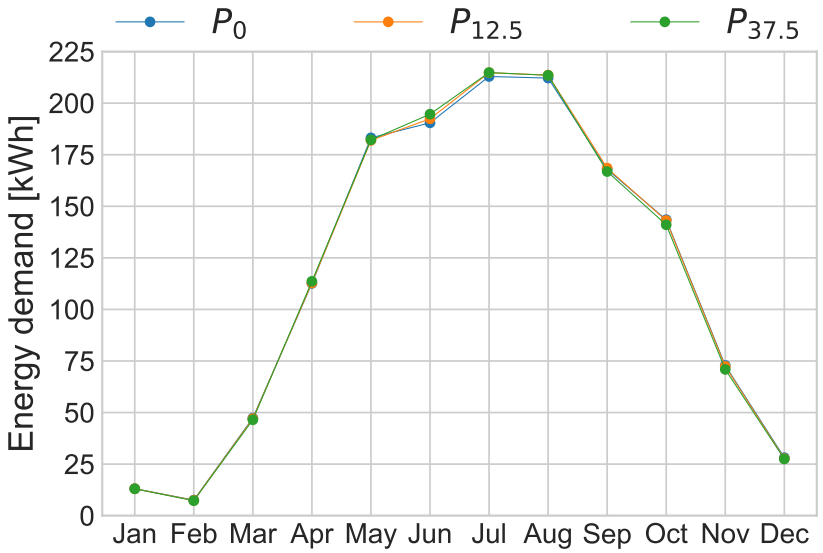

Figure 4.9 – Energy demand of the room for Hong Kong climate

First, because Hong Kong climate is hot and humid (see Table 4.1), the heater and the humidifier only worked in winter and they were turned on for less than 15 hours throughout this season. For the rest of the year, all of the energy demand came from the air-conditioner as shown in Table 4.10 for P_0.

Energy demand (kWh)				
Heater	Humidifier	Air-conditioner		Total
		sensible	*latent*	
7	6	649	730	1392

Table 4.10 – Yearly energy demand for P_0 decomposed by equipment for Hong Kong climate

Note that only the energy demand for P_0 is presented as only slight deviations were observed between P_0, $P_{12.5}$ and $P_{37.5}$, leading to approximately the same yearly energy demand. The latent contribution of the air-conditioner counted for almost half of the total energy demand highlighting the humid environmental conditions of Hong Kong.

Compared to Trappes climate, the energy demand of the room located in Hong Kong is 60% higher especially for the air-conditioner demand which was approximately 11 times superior.

4.2.2.2 Moisture buffering effect of the walls

Hong Kong climate is categorised as sub-tropical. To investigate the response of the room envelope when subjected to high relative humidity, the second week of June was selected as it is representative of a typical hot and humid week. The water vapour pressure evolution for P_0, $P_{12.5}$ and $P_{37.5}$ are presented in Figure 4.10. The exterior vapour pressure was also added.

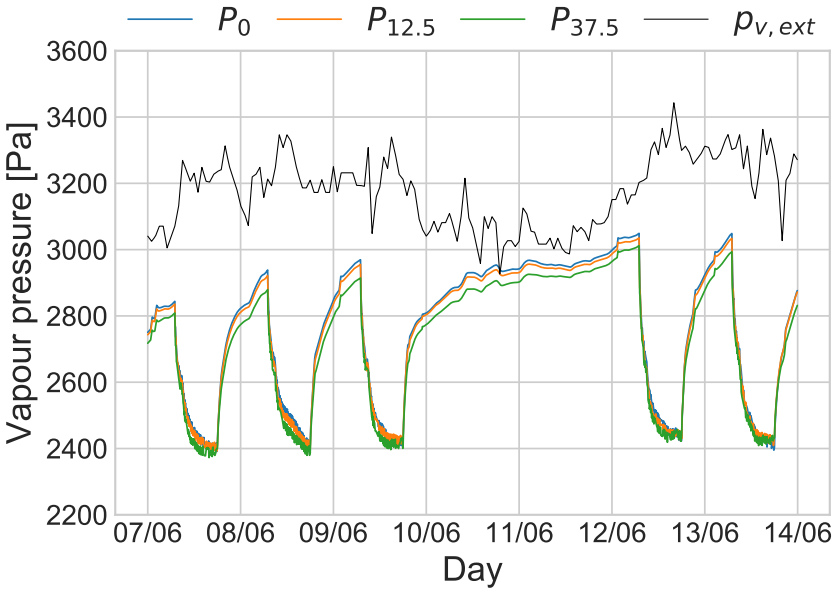

Figure 4.10 – Water vapour pressure evolution in the room during the second week of June for Hong Kong climate

The exterior water vapour pressure did not vary much during this week, but this was also the case for most of the humid weeks in Hong Kong. The changes from high vapour pressures to lower ones are the consequence of the air-conditioner switching between the ON and OFF positions in order to regulate the indoor temperature. During the weekend (June 10 and 11), the air-conditioner was turned off, leading to few variations of the indoor vapour pressure.

Figure 4.11. gives the relative humidity variations associated to the differences in water vapour pressure highlighted in Figure 4.10.

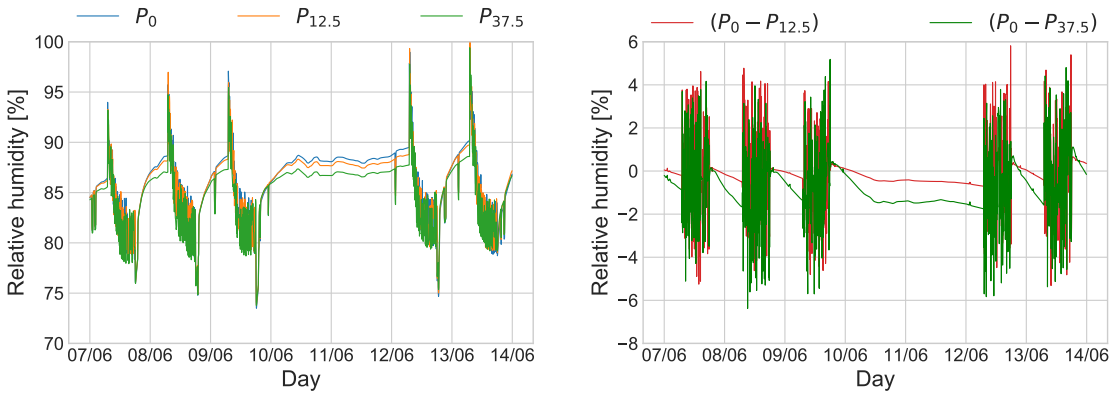

Figure 4.11 – Evolution of the relative humidity for P_0, $P_{12.5}$ and $P_{37.5}$ for the second week of June for Hong Kong climate (left). Evolution of the relative humidity difference between $P_{12.5}$ and P_0, and $P_{37.5}$ and P_0 (right)

The indoor relative humidity was almost always above 75% for the whole week. This result is in accord with what is really observed in Hong Kong as most buildings are designed with the temperature in mind, not the humidity. During the weekend, when they were no sources, the indoor humidity was around 87% as the exterior relative humidity varied between 88 and 95%.

Local spikes of high and low relative humidities are noticed during each day (left side of Figure 4.11). For example, the morning of June 9, the air-conditioner was turned on and the temperature decreased faster than the vapour pressure. Hence, according to the psychometric chart, this led to an increase of relative humidity. The evening of the same day, the air-conditioner was turned off provoking a decrease of relative humidity in the room.

Moreover, because the air-conditioner was repeatedly turned on and off throughout each day, fluctuations of humidities were noticed for each case leading to successive positive and negative differences between the case studies (right side of Figure 4.11). During the weekend, $P_{12.5}$ and $P_{37.5}$ led to a lower relative humidity, meaning that absorption occurred in the earth plaster. The maximum indoor relative humidity differences were 5.3% between P_0 and $P_{12.5}$, and 6.4% between P_0 and $P_{37.5}$.

The water vapour fluxes integrated on each day are presented in Figure 4.12 for P_0. $P_{12.5}$ and $P_{37.5}$ graphs are given in Appendix C.2.

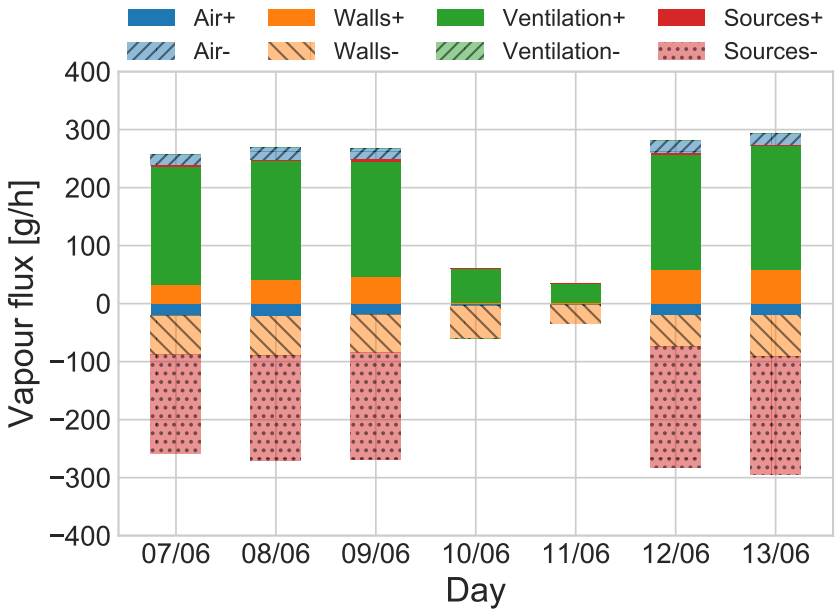

Figure 4.12 – Vapour fluxes representation for P_0 for Hong Kong climate

First, compared to Trappes, the total positive (or negative) fluxes were more than 3 times superior. The main reasons were:

- The difference between the exterior and the interior vapour pressure were bigger in Hong Kong than in Trappes;
- The air-conditioner was not working during June in Trappes while it was working every day of the month in Hong Kong.

Most of the negative vapour fluxes was dominated by the source term corresponding to the air-conditioner. For example, on June 8, 30% of the vapour flux was absorbed by the walls, 61% were the result of dehumidifying the indoor air and 9% contributed to decrease the indoor humidity. The vapour brought by the occupants was negligible compared to the vapour removed by the air-conditioner. It corresponded to only 1% of the source term each day. As a side note, using a stochastic scenario, a deterministic one or a constant one should not have a significant effect on the indoor air balance for Hong Kong climate.

The flux exchanged with the walls was both positive and negative for every day except for the weekend. As explained previously, because the air-conditioner was constantly turned on and off throughout the day, the variations of humidity provoked both absorption and desorption in the walls.

Figure 4.13 presents the vapour fluxes density for each wall.

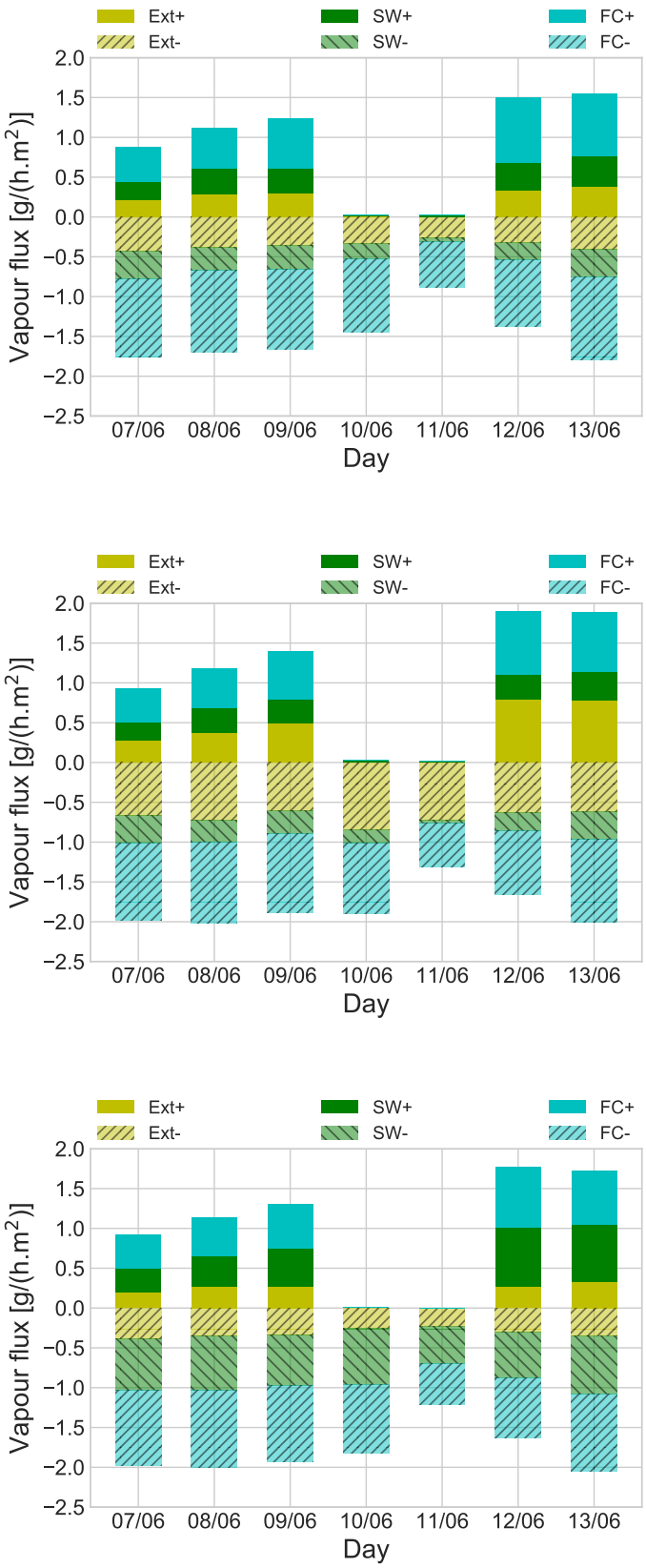

Figure 4.13 – Vapour exchanged with the walls for P_0, $P_{12.5}$ and $P_{37.5}$ (from top to bottom) for Hong Kong climate

First, as for Trappes, when the earth plaster is applied on the exterior wall ($P_{12.5}$) or on the separating walls ($P_{37.5}$), the vapour exchanged with the wall in question is higher than when no earth plaster is applied.

Table 4.11 gives the positive and negative amount of vapour exchanged with the walls divided by the surface of the corresponding wall for each case. The calculations were done in accord with Eqs. (4.4) and (4.5). Only the total vapour exchanged over the whole week is presented for each case.

	ϕ_{tot} $(g/(m^2))$			m_{tot} (kg)
	Exterior wall	*Separating walls*	*Floor and ceiling*	
P_{0+}	36.7	38.7	76.2	5.7
P_{0-}	59.8	41.8	153.3	10.0
Total	**96.5**	**80.5**	229.5	**15.7**
$P_{12.5+}$	65.3	37.0	73.6	5.9
$P_{12.5-}$	115.6	40.4	150.0	10.5
Total	**180.9**	77.4	223.6	**16.4**
$P_{37.5+}$	32.2	62.9	69.9	6.3
$P_{37.5-}$	53.0	106.6	143.1	11.8
Total	85.2	**169.5**	213.0	**18.1**

Table 4.11 – Vapour exchanged with the walls for P_0, $P_{12.5}$ and $P_{37.5}$

The total mass exchanged with the walls for $P_{12.5}$ and $P_{37.5}$ was more significant than for P_0 by 4 and 15% respectively, highlighting the impact of the earth plaster on the indoor humidity. The mass exchanged with the exterior wall of $P_{12.5}$ was approximately 1.9 times higher than the one from P_0. Similarly, the mass exchanged with the separating walls of $P_{37.5}$ was more than two times higher than the one from P_0. The results are in adequacy with the ones for Trappes.

Additionally, the contribution of the floor and ceiling in concrete was much more pronounced than for Trappes. For example, for P_0, the total mass exchanged was 2.4 and 2.9 times superior than the exterior and separating walls respectively. As high humidities remained in the room for a long time, the relatively high moisture penetration depth of the gypsum board (9.8 cm) and of the earth plaster (5 cm) let the moisture went through these materials. Whereas the concrete has a 0.5 cm penetration depth for a 20 cm thickness, providing a better buffering effect.

4.2.2.3 Indoor hygric comfort

As the indoor relative humidity covered a wide range in Hong Kong, Figure 4.14 presents its distribution by four percent intervals where the abscissa represents the mean value of each interval (for example the abscissa 42 corresponds to the interval [40;44]%).

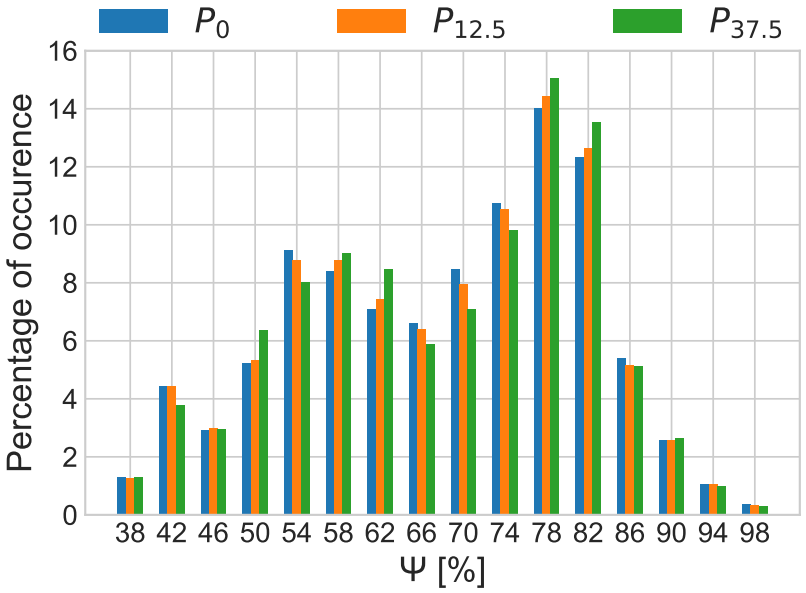

Figure 4.14 – Yearly indoor relative humidity distribution for Hong Kong climate

For clarity sake, the comfort zone was not represented. Slight deviations were observed between P_0, $P_{12.5}$ and $P_{37.5}$ leading to approximately 10% of the time spent in the comfort zone (see Table 4.12). Compared to Trappes, it is more than 5 times inferior. This result is consistent with Hong Kong humid climate: the indoor humidity was most of the time above 50%.

	[40;50]%
P_0	10.1
$P_{12.5}$	9.4
$P_{37.5}$	10.1

Table 4.12 – Prediction of the indoor relative humidity distribution in the comfort interval for P_0, $P_{12.5}$ and $P_{37.5}$ for Hong Kong climate

As Hong Kong climate is hot and humid, Wolkoff and Soren (2007) criterion does not seem relevant to estimate the yearly indoor comfort. However, Figure 4.11 showed that the relative humidity could be dampened up to 6.4%, reducing

the indoor discomfort provoked by high relative humidities. Therefore, looking at a smaller time scale, the month of December was selected because the air was dryer during this month. Results are presented in Figure 4.15, with a humidity distribution decomposed by two percent intervals.

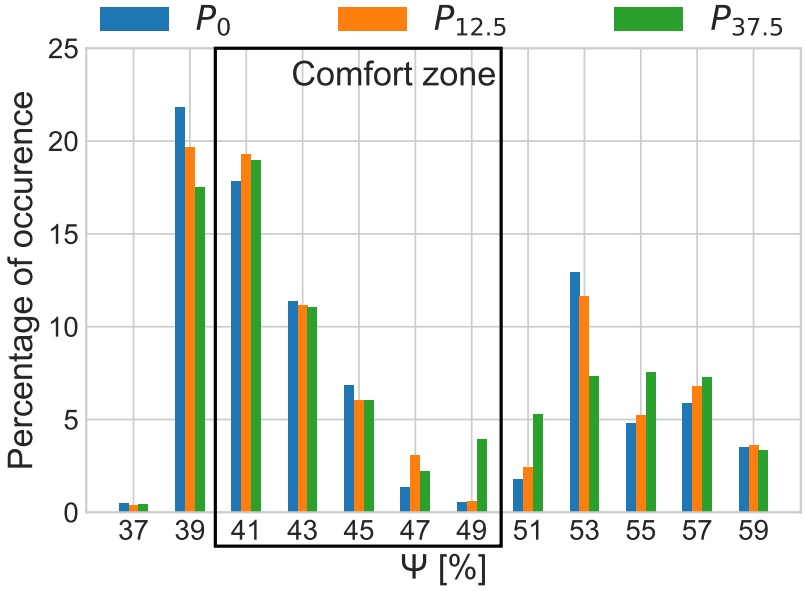

Figure 4.15 – Indoor relative humidity distribution in December for Hong Kong climate

Table 4.13 presents the time spent in the comfort zone in December.

	[40;50]%
P_0	38.0
$P_{12.5}$	40.2
$P_{37.5}$	42.3

Table 4.13 – Prediction of the indoor relative humidity distribution in the comfort interval for P_0, $P_{12.5}$ and $P_{37.5}$ for Hong Kong climate

The time spent in the comfort zone was improved by 2.2% and 4.3% respectively. Consequently, while the time spent in the comfort zone was not significant between the case studies at year scale, the walls contributed to dampen the indoor relative humidity at smaller scale. The indoor comfort improvement was observed at a specific month, but is noticeable at week or day scales (see Figure 4.11).

4.2.2.4 Moisture related risks

The isopleths at the surface of the exterior wall and at the interface between the concrete and the polystyrene are plotted in Figure 4.16 for the reference case P_0. The equations of the limit curves were previously given in Chapter 3.6.3.

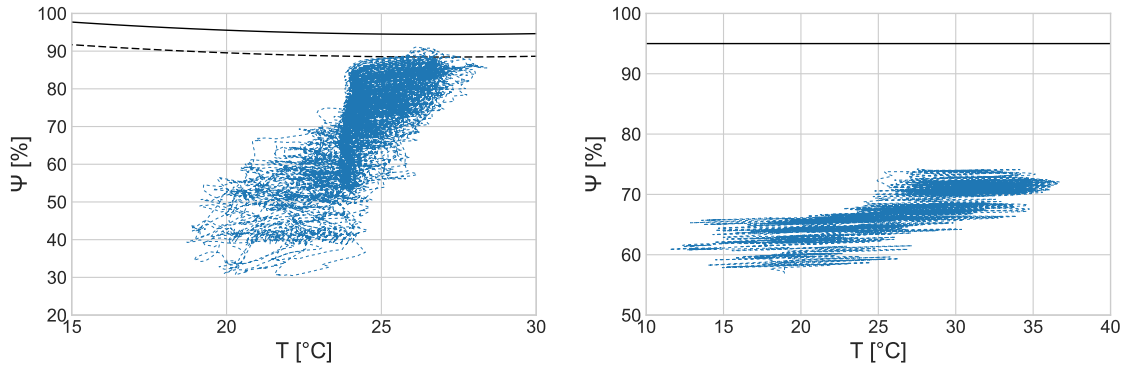

Figure 4.16 – Isopleth at the surface of the exterior wall (left) and at the interface between the concrete and the polystyrene (right) for P_0 subjected to Hong Kong climate

No risks are observed at the interface between the concrete and the polystyrene. However, at the surface of the wall, mould growth may be expected as some temperature and relative humidity couples were above the first limit curve. To take into account the material time of exposure to high relative humidities, the VTT model was used. Results are given in Figure 4.17 by assuming that the gypsum board belongs to the "medium resistant" class (see Chapter 2.7.3, Table 2.3).

The mould index for the gypsum board is well below 1, which is the threshold value initiating mould growth at the microscopic scale. It is usually assumed that a mould index between 1 and 2 is acceptable according to Ojanen et al. (2010). This means that mould was not expected to appear on the surface of the wall.

For $P_{12.5}$ and $P_{37.5}$, the literature did not provide the earth plaster limit curves. Consequently, it was chosen to rely only on the VTT model to estimate the mould growth on the surface of the material. The earth plaster was deemed "medium resistant" to mould like the gypsum board, based on the conclusion from Laborel-Préneron et al. (2018b) research on mould growth.

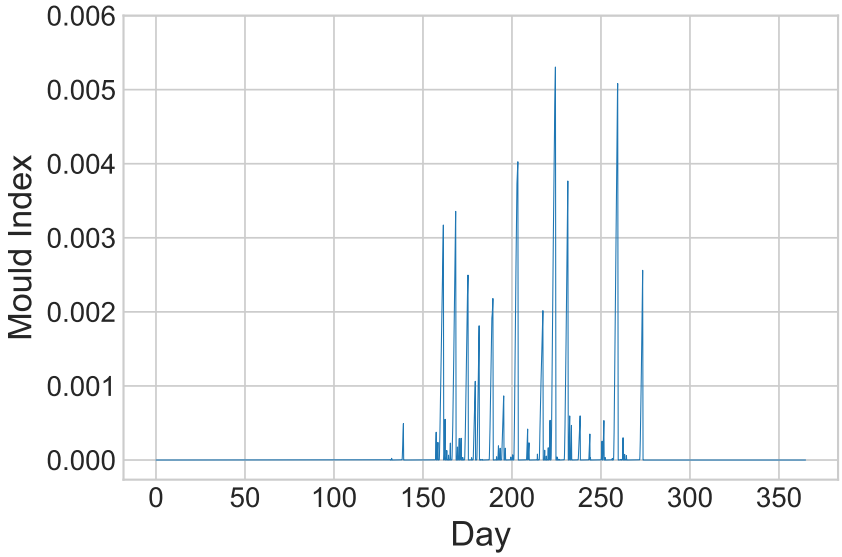

Figure 4.17 – Yearly mould index on the surface of the exterior wall calculated by the VTT model for P_0

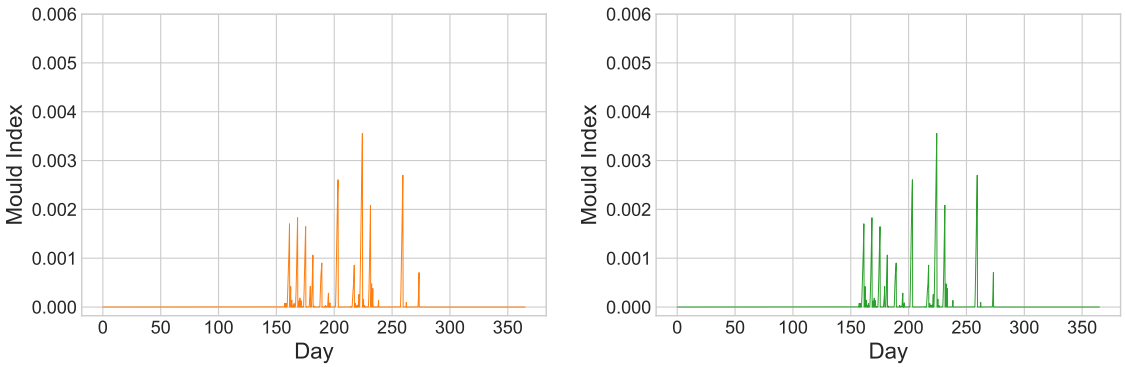

Figure 4.18 – Yearly mould index on the surface of the earth plaster calculated by the VTT model for $P_{12.5}$ (left) and $P_{37.5}$ (right)

For all of the case studies, the mould index was also well below 1. Therefore the earth plaster did not lead to any risks regarding mould growth.

4.2.3 Continental climate (Toronto)

4.2.3.1 Energy demand

The energy demand of the room located in Toronto is presented in Figure 4.19.

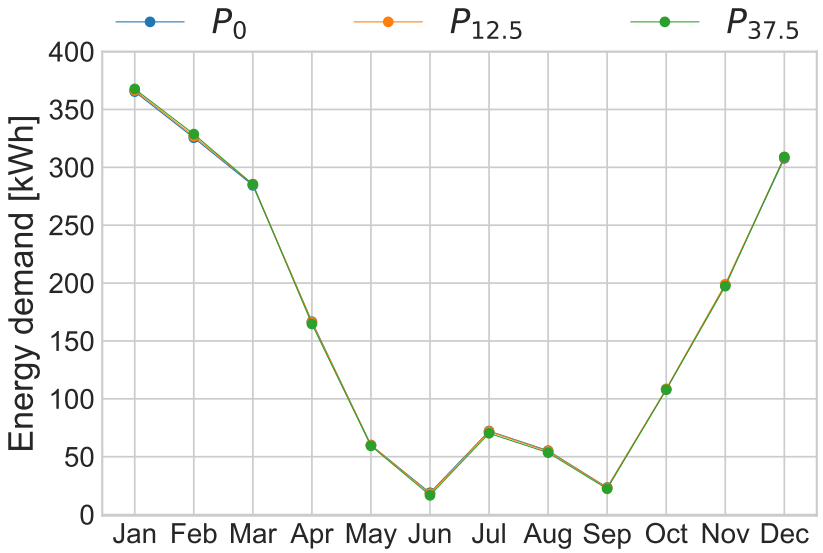

Figure 4.19 – Energy demand of the room for Toronto climate

First, the energy demand curve for Toronto is similar to the one from Trappes with high ernergy demand in winter due to the heating system, and a lower one in summer due to the air-conditioner not working much. Still, the energy consumption in winter was much higher. Slight deviations are observed between P_0, $P_{12.5}$ and $P_{37.5}$ with a maximum difference of 3.4 kWh reached in February. Therefore, Table 4.14 presents the energy demand for P_0 only as it was not deemed necessary to detail the energy demand for each case.

Energy demand (kWh)				
Heater	Humidifier	Air-conditioner		Total
		sensible	*latent*	
1595	235	92	63	1985

Table 4.14 – Yearly energy demand for P_0 decomposed by equipment for Toronto climate

The energy demand of the room exposed to Toronto climate was approximately 2.3 and 1.2 times higher than the one for Trappes and Hong Kong respectively. 80% of the energy demand came from the heater. Additionally, the energy demand of the humidifier was more than 4 times higher than the one in Trappes. The air-conditioner was turned on in summer for approximately 342 hours (corresponding to 14 days) in total.

4.2.3.2 Moisture buffering effect of the walls

Toronto climate is categorised as continental. However, looking at Table 4.14, it is much dryer than Trappes climate as the humidifier was turned on more often. This was also highlighted by Table 4.1 comparing the three different climates. To investigate the response of the walls exposed to this climate, the first week of May was selected as it is representative of a dry week, with significant variation of the exterior vapour pressure, as illustrated by Figure 4.20.

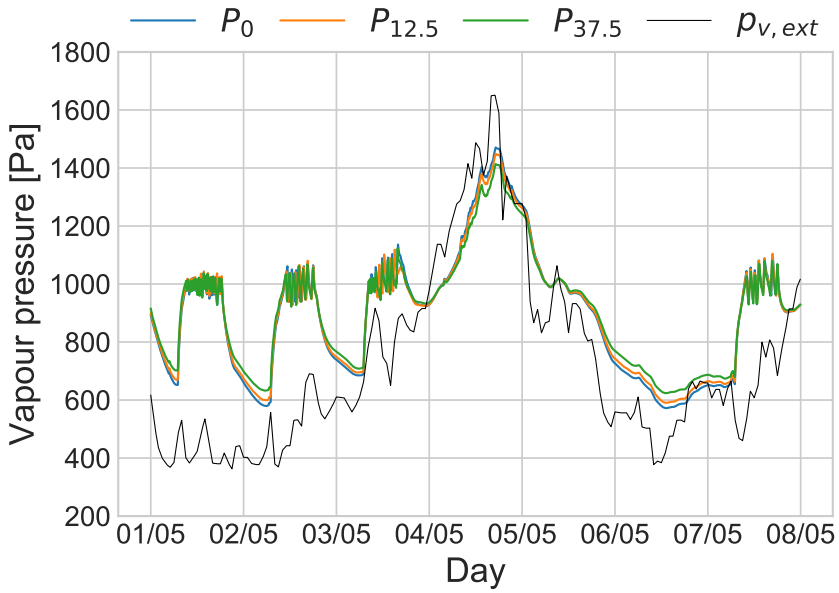

Figure 4.20 – Water vapour pressure evolution in the room for the first week of May for Toronto climate

First, the water vapour pressure was relatively low from May 1 to May 3, and always inferior to the interior one. Consequently, the humidifier was turned on during the day. Because it was repeatedly turned on and off, fluctuations of the interior vapour pressure were noticed around the vapour pressure corresponding the set point relative humidity of the humidifier. On May 4, the exterior vapour pressure rose and became superior to the interior one provoking its increase. On May 5 and May 6, the exterior vapour pressure was inferior to the interior one, but no control on the humidity was done because it was a weekend.

Secondly, the buffering capacity of the earth plaster was highlighted as low and high vapour pressures were smoothed. This corresponded to a maximum relative humidity dampening of 3.9% for $P_{12.5}$ and 4.7% for $P_{37.5}$ as shown in Figure 4.21.

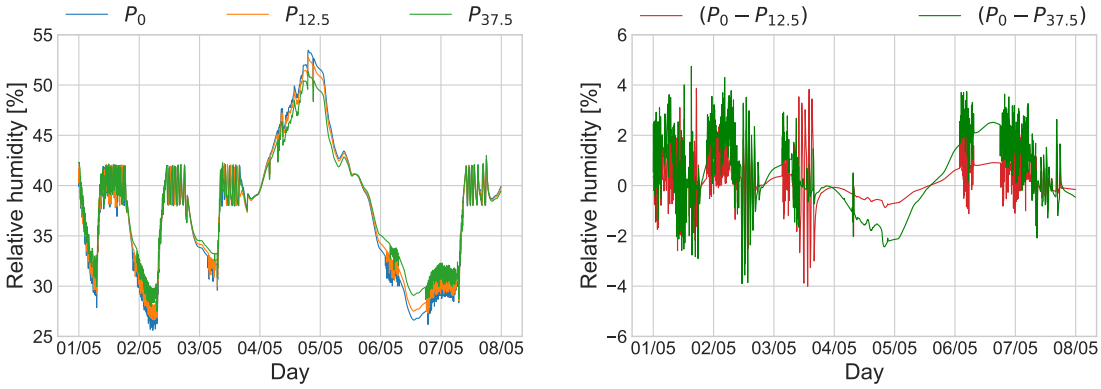

Figure 4.21 – Evolution of the relative humidity for P_0, $P_{12.5}$ and $P_{37.5}$ for the first week of May for Toronto climate (left). Evolution of the relative humidity difference between $P_{12.5}$ and P_0, and $P_{37.5}$ and P_0 (right)

The water vapour fluxes integrated on each day are presented in Figure 4.22 for P_0. $P_{12.5}$ and $P_{37.5}$ graphs are given in Appendix C.3.

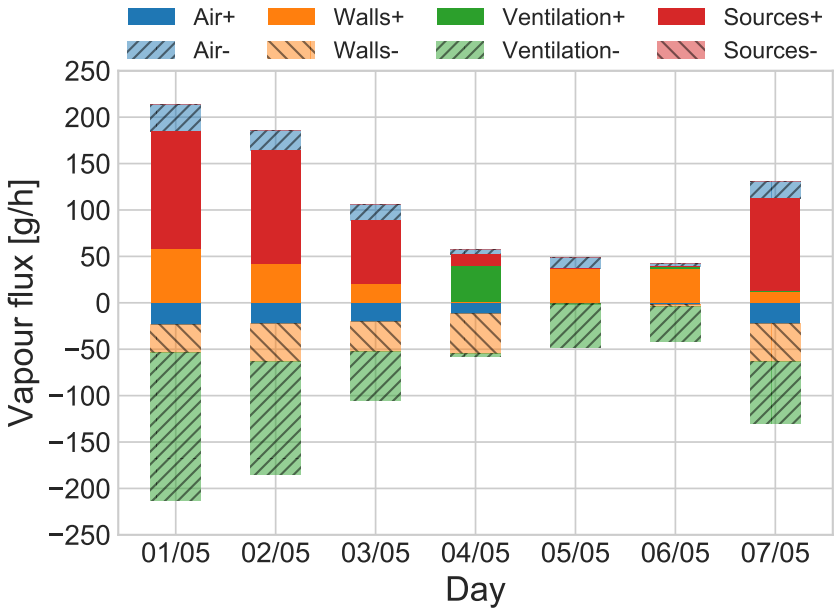

Figure 4.22 – Vapour fluxes representation for P_0 for Toronto climate

The source term was approximately 5.4 times superior than the one in Trappes. Compared to Hong Kong, the source was always positive as it corresponded to the occupants' metabolic vapour production and the humidifier.

From May 1 to May 3 and as well for May 7, moisture was removed through the ventilation, so the humidifier was turned on to regulate the indoor ambience. The vapour pressure fluctuations observed in Figure 4.20 are translated by both positive and negative vapour exchanged with the walls caused by successive desorption and

absorption respectively. This result is similar to the one obtained for Hong Kong when the air-conditioner was turned on.

On May 4, the humidifier was turned off, hence the indoor source corresponded to the occupants' vapour production. Moreover, because the exterior vapour pressure was higher than the interior one, moisture was brought into the room which was absorbed by the walls.

Contrarily, during the weekend (May 5 and May 6), the walls released moisture in the room to compensate for the negative ventilation flux.

Figure 4.23 presents the vapour fluxes density for each case and for each wall.

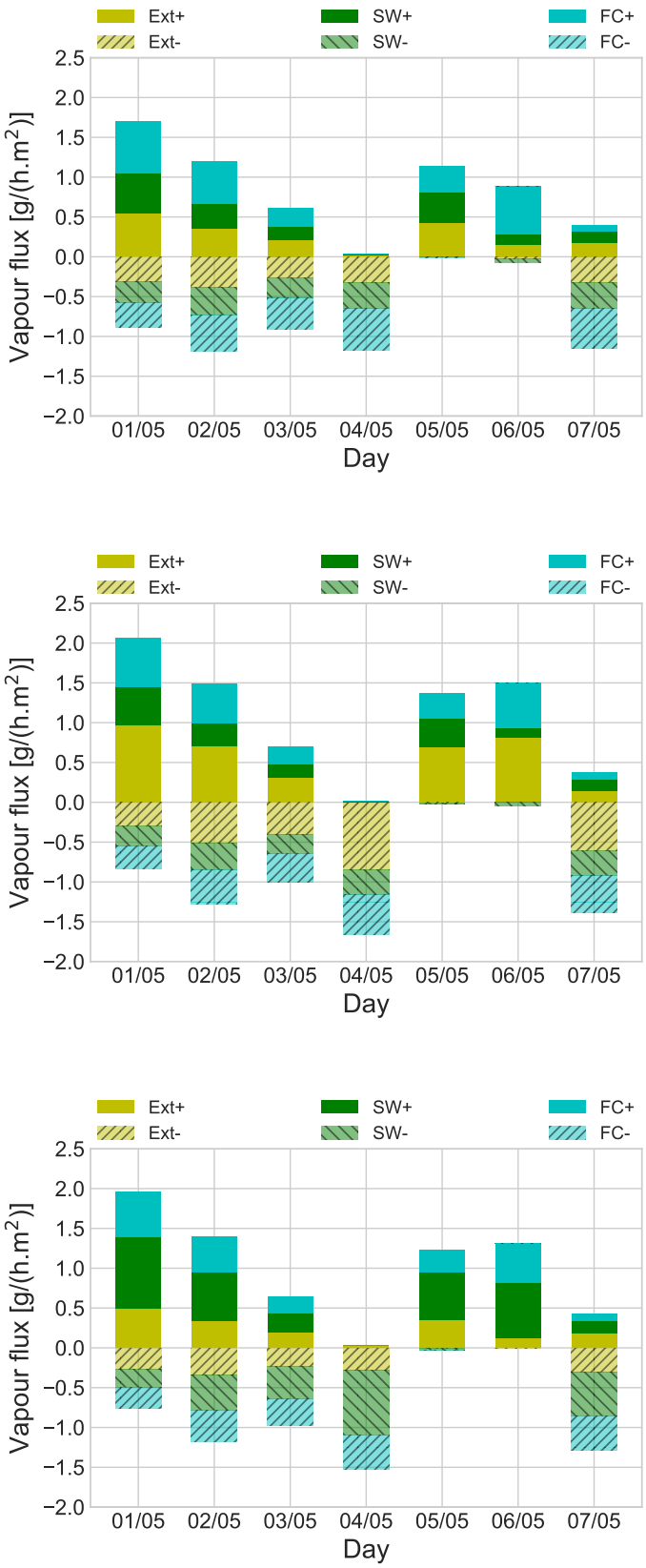

Figure 4.23 – Vapour exchanged with the walls for P_0, $P_{12.5}$ and $P_{37.5}$ (from top to bottom) for Toronto climate

As for the other two climates, when the earth plaster is applied on the exterior wall ($P_{12.5}$) or on the separating walls ($P_{37.5}$) the vapour exchanged with the wall in question is higher than when no earth plaster is applied.

Table 4.15 gives the mass exchanged with the exterior wall, the separating walls and the floor and ceiling for each case. Only the total mass over the whole week is presented.

	ϕ_{tot} $(g/(m^2))$			m_{tot} (kg)
	Exterior wall	*Separating walls*	*Floor and ceiling*	
P_{0+}	45.3	39.7	58.4	5.0
P_{0-}	39.2	37.6	52.2	4.5
Total	**84.5**	**77.3**	110.6	**9.5**
$P_{12.5+}$	87.2	38.1	55.3	5.3
$P_{12.5-}$	64.4	35.6	49.5	4.6
Total	**151.6**	73.7	104.8	**9.9**
$P_{37.5+}$	41.3	76.4	50.3	5.9
$P_{37.5-}$	34.7	58.8	44.0	4.8
Total	76.0	**135.2**	94.3	**10.7**

Table 4.15 – Vapour exchanged with the walls for P_0, $P_{12.5}$ and $P_{37.5}$

As for Trappes and Hong Kong, the mass exchanged with the walls for $P_{12.5}$ and $P_{37.5}$ was more significant than for P_0 by approximately 5 and 13% respectively. However, the positive masses were always superior to the negative ones in absolute terms. This means that most of the time, desorption occurred in the walls to compensate for the relatively dry indoor air.

Overall, the mass exchanged with the exterior wall was 1.8 times higher for $P_{12.5}$ than the one from P_0. Similarly, the mass exchanged with the separating walls for $P_{37.5}$ was also 1.7 times higher than the one from P_0. These observations are similar than the ones for Trappes and Hong Kong, meaning that when the earth plaster is applied on the surface of the walls, the mass exchanged is higher. This was already discussed in the previous section.

4.2.3.3 Indoor hygric comfort

The indoor hygric comfort decomposed by two percent humidity intervals is presented in Figure 4.24. As for the previous case study, only the values of indoor

relative humidity obtained when the occupants were present were used to plot Figure 4.24.

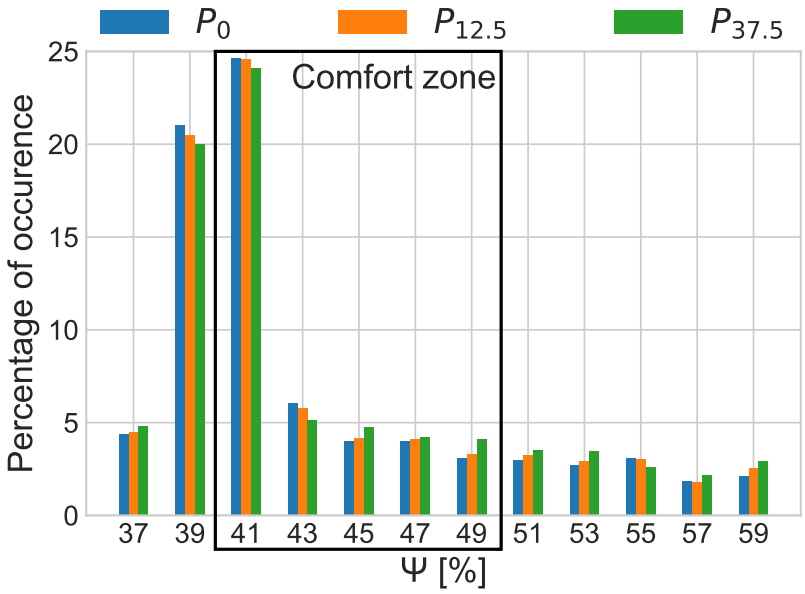

Figure 4.24 – Yearly indoor relative humidity distribution for Toronto climate

Figure 4.24 highlighted the relatively dry climate of Toronto. The indoor relative humidities were most of the time in the interval [38;42]% corresponding to the humidifier set point relative humidity (40% ± 2%).

Slight differences were observed between P_0, $P_{12.5}$ and $P_{37.5}$, leading to approximately 42% of the time spent in the comfort zone (see Table 4.16).

	[40;50]%
P_0	41.9
$P_{12.5}$	42.0
$P_{12.5}$	42.3

Table 4.16 – Prediction of the indoor relative humidity distribution in the comfort interval for P_0, $P_{12.5}$ and $P_{37.5}$ for Toronto climate

As for Hong Kong, looking at the relative humidity at year scale masked the walls moisture buffering effect. Indeed, it was previously showed in Figure 4.21 that the indoor humidity could be dampened up to 4.7% by the earth plaster.

Figure 4.25 presents the relative humidity distribution in June to investigate the comfort at a smaller time scale.

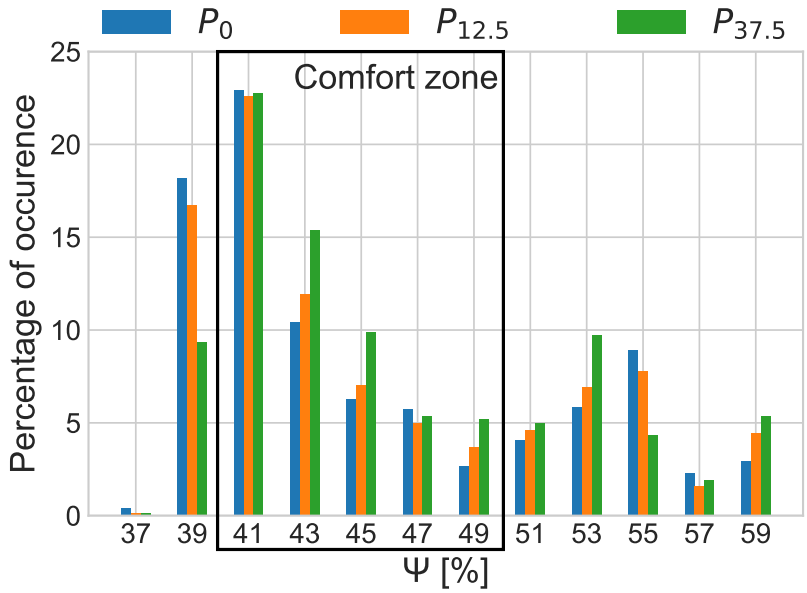

Figure 4.25 – Indoor relative humidity distribution for Toronto climate in June

The differences between P_0, $P_{12.5}$ and $P_{37.5}$ are more noticeable in June than at year scale. They are presented in Table 4.17.

	[40;50]%
	June
P_0	48.1
$P_{12.5}$	50.2
$P_{37.5}$	58.6

Table 4.17 – Prediction of the indoor relative humidity distribution in the comfort interval for P_0, $P_{12.5}$ and $P_{37.5}$ in February and May

In June, the time spent in the comfort zone improved by 2.1 and 10.5% for $P_{12.5}$ and $P_{37.5}$ respectively. The same conclusion than the one for Hong Kong climate can be drawn here: the walls moisture buffering might not influence the comfort at year scale but it is more noticeable at month, week or day scale.

4.2.3.4 Moisture related risks

Toronto climate did not lead to relative humidities above 80%, which is well below the limit curves for the plaster and polystyrene isopleths (see Figure 4.16). Moreover, it was previously shown, for Hong Kong climate, that even relative humidities above 80% did not lead to mould growth estimated by the VTT model due to the materials belonging to the "medium resistant" class. (see Figure 4.17). Consequently, it was

not deemed necessary to investigate the moisture related risks for Toronto climate and it was safe to assumed that no mould growth could occur.

4.3 Summary and conclusion

This chapter aimed at proposing an estimation of the walls moisture buffering impact on the energy demand, the indoor hygric comfort and the moisture related risks in an office when it was subjected to realistic solicitations.

The methodology consisted on simulating three climates to assess the walls buffering under mild and extreme environmental conditions: a temperate climate (Trappes), a sub-tropical one (Hong Kong) and a continental one (Toronto). In order to highlight the walls contribution on the indoor air balance, a hygroscopic plaster corresponding to an earth plaster was applied on surfaces corresponding to 12.5% and 37.5% of the total surface of the walls. The occupants' presence and activities were modelled in a stochastic way with No-MASS to emulate their real behaviour.

For all three of the climates, the results showed that using an earth plaster led to negligible differences on the energy performance of the room.

The walls moisture buffering was highlighted by focusing on a single week for each climate. The general observation was that when an earth plaster was applied on the walls, the vapour exchanges were more significant, up to 24% more than if no earth plaster was applied. On short period of time, the moisture buffering impact was noticeable as the relative humidity could be dampened up to 6.4% for Hong Kong climate for humidities above 85% for example.

For the indoor hygric comfort, the walls moisture buffering was investigated at different time scales for all three climates. At year scale, only slight differences on the relative humidity distribution in the room were observed between the different case studies. However, for specific months, the walls moisture buffering effect was more noticeable. For example in Toronto the time spent in the comfort zone was improved by 10.5% in June. This led to improve the indoor hygric comfort.

The moisture related risks were estimated with the isopleths and the VTT model. For Hong Kong, the isopleths of the earth plaster showed a slight risk of mould growth, but it was not the case with the VTT model estimation as the the materials were categorised as "medium resistant" to mould growth. No risks were observed for the other two climates.

The walls moisture buffering effect was less pronounced in our case than in

the literature (see Chapter 1.1). But we proposed its estimation with a realistic occupancy scenario. Compared to cyclic and constant scenarios, the sources were not continuous in time, leading to a lower average moisture production and random spikes of vapour production. Moreover, compared to laboratory experiments using constant boundary conditions (as in Yoshino et al. (2009) for example), we simulated realistic boundary conditions with significant variations of relative humidity. This gave less smoother variations of the indoor humidity, soliciting the materials in a different way. The literature showed a non negligible impact of the walls moisture buffering on the indoor humidity under specific conditions to underline it, but under realistic conditions the impact — while not negligible — is less pronounced.

General conclusion and perspectives

This work investigated the moisture buffering of materials on the hygrothermal performance of an office room. This property is already well known and it can contribute to smooth the humidity in a passive way. The main factors influencing it are the ventilation, the interaction between the indoor air and the walls, and the indoor moisture sources.

The state of the art presented in Chapter 1 showed that the buffering property was highlighted at material and wall scales through laboratory experiments and numerical models. Its sensitivity to the ventilation rate was thoroughly investigated but few researches focused on studying the moisture sources impact in details, especially the ones related to the occupants' presence and activities. These sources are complex to model as the occupants' behaviour is by nature stochastic (or probabilistic). As a consequence, most studies in the hygrothermal field rely on simplified occupancy scenarios such as constant scenarios or deterministic ones.

Therefore, our work aimed at proposing a numerical methodology taking into account the following elements:

- The coupled heat and mass transfer in a room envelope;
- The air-conditioning system;
- The stochastic modelling of the occupants' presence and activities.

Chapter 2 presented the development of the model combining these elements. The coupled heat and mass transfer in the walls was described by the mass and energy conservation equations driven by the temperature and the capillary pressure changes respectively. The exterior boundary conditions accounted for the convective heat and mass transfer, the radiative heat transfer and the latent and sensible transfer due to vapour exchange. The air-conditioning system was depicted by a heater, a humidifier and a split-type air-conditioner. This work led to the development of the *Room model* written in *Python*. Finally, the occupants' presence and activities were modelled in a stochastic way in a numerical platform called No-MASS. It was coupled with the *Room model* by relying on a Functional Mockup Interface. Performance indicators associated with each module of the model were defined: the energy demand of the air-conditioning system, the indoor hygric comfort and the moisture related risks in the walls.

Particular attention was addressed to the occupancy scenario impact in Chapter 3. The hygrothermal sensitivity of a room subjected to different scenarios was investigated by simulating a stochastic scenario, a deterministic one, a constant one and a scenario taken from the French regulation code (RT Bâtiment, 2012). At year scale,

only slight deviations on the energy demand and the moisture related risks were noticed between the stochastic, the deterministic and the constant scenario, but the impact on the indoor hygric comfort was more significant. The French code scenario gave a comparison between a relatively realistic scenario and the one used to design new buildings construction in France. Large discrepancies on the energy demand and the hygric comfort were observed between this case and the other three. The deviations on humidity between the stochastic, the deterministic and the constant scenarios were marginal at year scale, but far from negligible at smaller time scales (seasonal or monthly). It could lead to deviation up to 46% on the cooling demand and up to 21% on the comfort estimation due to a seasonal effect considered by the stochastic scenario. As the walls moisture buffering effect is sensitive to short humidity variations, the stochastic scenario was favoured in our approach to estimate it.

The walls moisture buffering effect was investigated in Chapter 4 by simulating different climates (temperate, humid sub-tropical and continental). It was emphasised by simulating a room in which a hygroscopic plaster — an earth plaster — was applied on the walls surface. A comparison with a reference case study with no hygroscopic plaster was done to highlight its buffering capacity. For each climate, almost no deviations were observed on the room energy demand. However, discrepancies appeared on the indoor hygric comfort. It was investigated at different scales. At year scale, the effect was almost not noticeable. However, for specific months, differences between a walls with and without hygroscopic plaster resulted on an improvement on the indoor hygric comfort between 2 and 10% depending on the climate. This improvement was more noticeable at day scale were the relative humidity was dampened in more significant proportion, up to 6% in a humid climate.

To conclude, this work proposed a numerical methodology to estimate the walls moisture buffering effect on the hygrothermal performance of a room subjected to realistic indoor sources, especially the ones related to the occupants' presence and activities as they were modelled in a stochastic way. Results were in adequacy with the ones found in the literature as the indoor relative humidity variations were dampened. However, the effect was less pronounced in our case than in other studies. The discrepancies were due to the description of the indoor sources depicted by the occupants' presence and activities, and by the simulation of variable boundary conditions. Therefore, describing accurately the indoor sources is of crucial importance in the aim of estimating the walls moisture buffering.

Further work could focus on validating the whole model by comparing the results

with experimental data.

The modelling of the occupants' activities in offices could be enhanced by considering windows opening for example. This feature is already implemented in No-MASS (Chapman et al., 2017) but not coupled with the *Room model* yet. It could be interesting to combine the windows opening activity and the walls moisture buffering to investigate the contribution of each of these elements towards indoor air balance.

The *Room model* takes into account a lot of parameters. For example, the occupancy scenario had a significant impact on the performance indicators for a temperate climate. But for a humid climate (Hong Kong), this parameter had almost no influence as it represented approximately 1% of the total indoor load. Other parameters influence indoor air: the wall materials hygrothermal properties, the ventilation rate, the air-conditioning system set point temperature and relative humidity, etc... A sensitivity analysis could help sorting the most influential parameters and evaluating the robustness of the moisture buffering effect.

Finally, from a broader standpoint, simulations could be extended to residential buildings where the occupants generate more moisture throughout various activities like showering, cooking, dishwashing, ... This module is still on ongoing development in No-MASS platform, and could later be coupled with the *Room model* as the Functional Mockup Interface is already implemented. Other case study could include a cafeteria with moisture production peaks at specific times of the day due to the occupants and the meals, or a library where books also provide a buffering capacity.

Bibliography

Abe, K., Nagao, Y., Nakada, T., and Sakuma, S. (1996). Assessment of indoor climate in an apartment by use of fungal index. *Applied and Environmental Microbiology*, 62(3):959–963.

Abuku, M., Janssen, H., and Roels, S. (2009). Impact of wind-driven rain on historic brick wall buildings in a moderately cold and humid climate: Numerical analyses of mould growth risk, indoor climate and energy consumption. *Energy and Buildings*, 41.

Adan, O. (1994). *On the fungal defacement of interior finishes*. PhD thesis, The Netherlands.

Afnor (2000). EN ISO 12570 - Performance hygrothermique des matériaux et produits pour le bâtiment - Détermination du taux d'humidité par séchage à chaud.

Afnor (2005). EN ISO 7730 - Ergonomics of the thermal environment - Analytical determination and interpretation of thermal comfort using calculation of the pmv and ppd indices and local thermal comfort criteria.

Afnor (2007). EN 15026 - Hygrothermal performance of building components and building elements - Assessment of moisture transfer by numerical simulation.

Afnor (2013). EN ISO 12571 - Performance hygrothermique des matériaux et produits pour le bâtiment - Détermination des propriétés de sorption hygroscopique.

Afram, A. and Janabi-Sharifi, F. (2014). Theory and applications of HVAC control systems - a review of model predictive control (MPC). *Building and Environment*, 72:343–345.

Afshari, A. and Bergsoe, N. (2003). Humidity as a control parameter for ventilation. *Indoor and Built Environment*, 12(4).

Arrêté du 24 Mars 1982 (1982). http://www.legifrance.gouv.fr/affichtexte.do? cidtexte=jorftext000000862344.

ASHRAE (2005). Fundamentals thermodynamics properties of water at saturation. atlanta, GA: American society of heating, refrigerating and air-conditioning engineers, inc.

Aït Oumeziane, Y., Bart, M., Moissette, S., and Lanos, C. (2014). Hysteretic Behaviour and Moisture Buffering of Hemp Concrete. *Transport in Porous Media*, 103(3):515–533.

Becker, T. W. and Kaus, B. J. (2013). *An introduction to computational methods focus on solid Earth applications of continuum mechanics*. Lecture notes for USC GEOL557, v1.1.1.

Bejan, A. (2013). *Convection Heat Transfer*. Wiley & Sons, Hoboken, 4 edition.

Berger, J. (2014). *Contribution à la modélisation hygrothermique des bâtiments : application des méthodes de réduction de modèle*. PhD thesis, Université de Grenoble, Grenoble.

Bremaud, P. (1999). *Markov Chains*. Springer-Verlag New York, 1 edition.

British Standards Institution (2002). BS 5250:2002 british standard code of practice for control of condensation in buildings.

Brunauer, S., Deming, L., Deming, E., and Teller, E. (1940). On a theory of the Van Der Waals adsorpion of gases. *J. Am. Chem. Soc.*, 62(7):1723–1732.

Brunauer, S., Emmet, P. H., and Teller, E. (1938). Adsorption of gases in multimolecular layer. *J. Am. Chem. Soc.*, 60(2):309–319.

Bui, R., Labat, M., and Aubert, J.-E. (2017a). Comparison of the saturated salt solution and the dynamic vapor sorption techniques based on the measured sorption isotherm of barley straw. *Construction and Building Materials*, 141:140–151.

Bui, R., Labat, M., and Lorente, S. (2017b). Impact of heat and moisture transfer through a multilayer wall on the comfort conditions of an occupied room. In *15th Canadian Conference on Building Science and Technology*, Vancouver, Canada.

C-E. Hagentoft, O. A. (2004). Assessment method of numerical prediction models for combined heat, air and moisture transfer in building components : Benchmarks for one-dimensional cases. *Journal of Thermal Envelope and Building Science*, 27(4).

Cao, G., Awbi, H., Yao, R., Fan, Y., Sirén, K., Kosonen, R., and Zhang, J. (2014). A review of the performance of different ventilation and airflow distribution systems in buildings. *Buildings and Environment*, 73:171–186.

Carman, P. (1951). Physical adsorption of gases on porous solids. ii. calculation of pore-size distributions. *Proceedings of the Royal Society of London. Series A, Mathematical and Physical Sciences*, 209(1096):69–81.

Carmeliet, J., De Wit, M., and Janssen, H. (2005). Hysteresis and moisture buffering of wood. In *Symposium of Building Physics in the Nordic Countries*, pages 55–62.

Carmeliet, J., Hens, H., Roels, S., Adan, O., Brocken, H., Cerny, R., Pavlik, Z., Hall, C., Kumaran, K., and Pel, L. (2004). Determination of the liquid water diffusivity from transient moisture transfer experiments. *IEA EACBS Annex 41*, 27(4):277–305.

Cerolini, S., D'Orazio, M., Di Perna, C., and Stazi, A. (2009). Moisture buffering capacity of highly absorbing materials. *Energy and Buildings*, 41(2):164–168.

Chamoin, J. (2013). *Optimisation des propriétés (physiques, mécaniques et hydriques) de bétons de chanvre par la maîtrise de la formulation.* PhD thesis, INSA de Rennes.

Chang, W.-K. and Hong, T. (2013). Statistical analysis and modeling of occupancy patterns in open-plan offices using measured lighting-switch data. *Building Simulation*, 6:23–32.

Chapman, J., Siebers, P.-O., and Robinson, D. (2017). Multi-agent stochastic simulation of occupants for building simulation. In *15th IBPSA Conference*, San Francisco, USA.

Chapman, J., Siebers, P.-O., and Robinson, D. (2018). On the multi-agent stochastic simulation of occupants in buildings. *Journal of Building Performance Simulation*, 11(5):604–621.

Claisse, P., El-Sayad, H., and Ganjian, E. (2009). Water vapour and liquid permeability measurements in mortar samples. *Advances in Cement Research*, 21(2):83–89.

Clarke, J. (2001). Energy simulation in building design. Technical report, Routledge, United Kingdom.

Cole, R. (1976). The longwave radiation incident upon the external surface of buildings. *Building Services Engineers*, 44:195–206.

Collet, F. (2004). *Caractérisation hydrique et thermique de matériaux de génie civil à faibles impacts environnementaux.* PhD thesis, INSA de Rennes.

Crank, J. and Nicolson, P. (1947). A practical method for numerical evaluation of solutions of partial differential equations of the heat-conduction type. *Proceedings of the Cambridge Philosophical Society*, 43:207–226.

Crawkey, D. B., Lawrie, L. K., Winkelmann, F. C., Buhl, W., Huang, Y. J., Pendersen, C. O., Strand, R. K., Liesen, R. J., Fisher, D. E., Witte, M. J., and Glazer, J. (2001). Energyplus: creating a new-generation building energy simulation program. *Energy and Buildings*, 33:319–331.

Darakdjian, Q., Bille, S., and Inard, C. (2017). Data mining of building performance simulations comprising ocupant behaviour modelling. *Advances in Building Energy Research*, 139:214–223.

Darcy, H. (1856). *Les fontaines publiques de la ville de Dijon*. Dalmont.

Delgado, Ramos, Barreira, and de Freitas (2010). A critical review of hygrothermal models used in porous building materials. *Journal of Porous Media*, 13(3):231–234.

Delgado, J., Barreira, E., Ramos, N., and de Freitas, V. (2013). *Hygrothermal Numerical Simulation Tools Applied to Building Physics*. Springer.

DesignBuilder (2014). DesignBuilder software limited.

Desta, T. Z., Langmans, J., and Roels, S. (2011). Experimental data set for validation of heat, air and moisture transport models of building envelopes. *Building and Environment*, 46(5):1038–1046.

Diasty, R., Fazio, P., and Budaiwi, I. (1992). Modelling of indoor air humidity: the dynamic behaviour within the enclosure. *Energy and Buildings*, 19:61–73.

Dixit, M., Fernandez-Solis, J., Lavy, S., and Culp, C. (2010). Identification of parameters for embodied energy measurement: A literature review. *Energy and Buildings*, 42:1238–1247.

Djedjig, R., Bozonnet, E., and Belarbi, R. (2015). Analysis of thermal effects of vegetated envelopes: Integration of a validated model in a building energy simulation program. *Energy and Buildings*, 86:93–103.

Dubois, S., Evrard, A., and Lebeau, F. (2014). Modeling the hygrothermal response of a prefabricated straw bale panel and assessing its impact on indoor climate. In *2014 ASABE and CSBE/SCGAB Annual International Meeting*.

Evrard, A. (2008). *Transient hygrothermal behaviour of lime-hemp materials*. PhD thesis, Université Catholique de Louvain, Louvain, Belgique.

Feng, X., Yan, D., and Hong, T. (2015). Simulation of occupancy in buildings. *Energy and Buildings*, 87:348–359.

Fermanel, F. and Miriel, J. (1999). Air heating system: influence of a humidifier on thermal comfort. *Applied Thermal Engineering*, 19:1107–1127.

Freitas, V., Abrantes, V., and Crausse, P. (1996). Moisture migration in building walls - Analysis of the interface phenomena. *Building and Environment*, 31(2):99–108.

Gan, G. (2014). Dynamic interactions between the ground heat exchanger and environments in earth-air tunnel ventilation of buildings. *Energy and Buildings*, 85:12–22.

Ge, H., Yang, X., Fazio, P., and Rao, J. (2014). Influence of moisture load profiles on moisture buffering potential and moisture residuals of three groups of hygroscopic materials. *Building and Environment*, 81:162–171.

Gill, Z., Tierney, M., Pegg, I., and Allan, N. (2010). Low-energy dwellings: the contribution of behaviours to actual performance. *Building Research and Information*, 38(5).

Gobakis, K. and Kolokotsa, D. (2017). Coupling building energy simulation software with microclimatic simulation for the evaluation of the impact of urban outdoor conditions on the energy consumption and indoor environmental quality. *Energy and Buildings*, 157:101–115.

Grossman, C. and Roos, H.-G. (2007). *Numerical Treatment of Partial Differential Equations*. Springer, 3 edition.

Hagashima, A., Tanimoto, J., and Ken-Ich, N. (2005). Intercomparison of experimental convective heat transfer coefficients and mass transfer coefficients of urban surfaces. *Boundary-Layer Meteorology*, 117:551–576.

Haines, W. (1939). Studies in the physical properties of soil, V, the hysteresis effect in capillary properties, and the modes of moisture distribution associated therewith. *Journal of Agricultural Science*, 20:97–116.

Haldi, F. and Robinson, D. (2009). Interactions with window openings by office occupants. *Building and Environment*, 44(12):2378–2395.

Haldi, F. and Robinson, D. (2010). Adaptive actions on shading devices in response to local visual stimuli. *Journal of Building Performance Simulation*, 3(2):135–153.

Hameury, S. (2005). Moisture buffering capacity of heavy timber structures directly exposed to an indoor climate: a numerical study. *Building and Environment*, 40:1400–1412.

Harkins, W. and Jura, G. (1944). Surface of Solids. X. Extension of the Attractive Energy of a Solid into an Adjacent Liquid or Film, the Decrease of Energy with Distance, and the Thickness of Films. *J. Am. Chem. Soc.*, 66(6):919–927.

Henderson (1952). A basic concept of equilibrium moisture. *Agricultural Engineering*, 33(1):29–32.

Hens, H. (2012). *Building Physics Heat, Air and Moisture*. Ernst & Sohn, 2 edition.

Hens, H. L. S. C. (2015). Combined heat, air, moisture modelling: A look back, how, of help? *Building and Environment*, 91:138–151.

Hukka, A. and Viitanen, H. (1994). A mathematical model for mould growth on wooden material. *Wood Science and Technology*, 33:475–485.

Hunt, D. (1980). The use of artificial lighting in relation to daylight levels and occupancy. *Lighting Research and Technology*, 14:21–33.

Hutcheon, N. (1955). Humidity in Canadian buildings. In *Canadian Chapters Conference*, Toronto, Canada.

IDAE (2006). Instituto para la diversificacion y ahorro de la energıa. In *Eficiencia Energetica y Energıas Renovables (No. 8)*, Madrid, Espana.

IEA-Annex 14 (1990). *Condensation and Energy*. Source Book, Acco, Leuven.

International Union of Pure and Applied Chemistry (1985). Reporting physisorption data for gas/solid systems with special reference to the determination of surface area and porosity. *Pure Applied Chemistry*, 57:603–619.

Jaboob, S. (2015). *Stochastic modelling of occupants' activities and related behaviours*. PhD thesis, University of Nottingham, Nottingham.

Janssen, H. (2011). Thermal diffusion of water vapour in porous materials: Fact or fiction? *International Journal of Heat and Mass Transfer*, 54(7-8):1548–1562.

Janssen, H., Blocken, B., and Carmeliet, J. (2007). Conservative modelling of the moisture and heat transfer in building components under atmospheric excitation. *International Journal of Heat and Mass Transfer*, 50(5-6):1128–1140.

Janssens, A. (2001). Advanced numerical models for hygrothermal research: 2dhav model description. *Moisture analysis and condensation control in building envelopes*, 40:177–178.

Johansson, P., Ekstrand-Tobin, A., and Bok, G. (2014). An innovative test method for evaluation the critical moisture level for mould growth on building materials. *Building and Environment*, 81:404–409.

Johansson, P., Pallin, S., and Shahriari, M. (2010a). Risk assessment model applied on building physics: Statistical data acquisition and stochastic modeling of indoor moisture supply in swedish multi-family dwellings. *In IEA Annex 55 RAP-RETRO. Copenhagen*.

Johansson, P., Svensson, T., and Ekstrand-Tobin, A. (2013). Validation of critical moisture conditions for mould growth on building materials. *Building and Environment*, 62:201–209.

Johansson, S., Wadsö, L., and Sandin, K. (2010b). Estimation of mould growth levels on rendered façades on surface relative humidity and surface temperature measurements. *Building and Environment*, 45:1153–1160.

Kalagasidis, A. S. (2004). *HAM-Tools, an integrated simulation tool for Heat, Air and Moisture transfer analyses in building physics*. PhD thesis, Chamlers University of Technology.

Kalagasidis, A. S., Rode, C., and Woloszyn, M. (2008). HAM-Tools: a whole building simulation tool in annex 41. *IEA EACBS Annex 41*, 130:21–35.

Kashif, A., Binh, L. X. H., Dugdale, J., and Ploix, S. (2011). Agent based framework to simulate inhabitants' behaviour in domestic settings for energy management. In *International Conference on Agents and Artificial Intelligence*, Rome, Italy.

Knabe, G. and Le, H.-T. (2001). Building simulation by application of a HVAC system considering the thermal and moisture behaviour of the perimeter walls. In *Seventh International IBPSA Conference*, Rio De Janeiro, Brazil.

Künzel, H., Holm, A., and Krus, M. (2008). Hygrothermal properties and behaviour of concrete. *WTA-Almanach*, pages 161–181.

Künzel, H., Holm, A., Zirkelbach, D., and Karagiozis, A. (2005). Simulation of indoor temperature and humidity conditions including hygrothermal interactions with the building envelope. *Energy and Buildings*, 78:554–561.

Künzel, H. M. (1995). *Simultaneous Heat and Moisture Transport in Building Components - One- and two-dimensional calculation using simple parameters*. PhD thesis, Fraunhofer Institute of Building Physics, Stuggart, Allemagne.

Künzel, H. M. and Kiesel, K. (1994). Calculation of heat and moisture transfer in exposed building components. *Journal of Heat and Mass Transfer*, 40(1):159–167.

Krus, M. (1996). *Moisture transport and storage coefficients of porous mineral building materials*. PhD thesis, Fraunhofer Institute of Building Physics.

Kumaran, K. (2009). *Moisture control in buildings*. Trechsel editorial serie, ASTM manual series edition.

Kwiatkowski, J., Woloszyn, M., and Roux, J.-J. (2009). Modelling of hysteresis influence on mass transfer in building materials. *Building and Environment*, 44(3):633–642.

Kwiatkowski, J., Woloszyn, M., and Roux, J.-J. (2011). Influence of sorption isotherm hysteresis effect on indoor climate and energy demand for heating. *Applied Thermal Engineering*, 31(6-7):1050–1057.

Labat, M. (2012). *Chaleur - Humidité - Air dans les maisons à ossature bois : expérimentation et modélisation*. PhD thesis, Institutal National des Sciences Appliquées de Lyon, Lyon.

Labat, M., Magniont, C., Nicolaas, O., and Auberty, J.-E. (2016). From the experimental characterization of the hygrothermal properties of straw-clay mixtures to the numerical assessment of their buffering potential. *Building and Environment*, 97:69–81.

Labat, M. and Woloszyn, M. (2015). Moisture balance assessment at room scale for four cases based on numerical simulations of heat-air-moisture transfers for

a realistic occupancy scenario. *Journal of Building Performance Simulation*, 9(5):487–509.

Labat, M., Woloszyn, M., Garnier, G., and Roux, J. J. (2015). Dynamic coupling between vapour and heat transfer in wall assemblies: Analysis of measurements achieved under real climate. *Building and Environment*, 87:129–141.

Laborel-Préneron, A., Magniont, C., and Aubert, J. (2018a). Hygrothermal properties of unfired earth bricks: effect of barley straw, hemp shiv and corn cob addition. *Energy and Buildings*, 178:265–278.

Laborel-Préneron, A., Ouédraogo, K., Simons, A., Labat, M., Bertron, A., Magniont, C., Roques, C., Roux, C., and Aubert, J. (2018b). Laboratory test to assess sensitivity of bio-based earth materials to fungal growth. *Building and Environment*, 142:11–21.

Langmuir, I. (1918). The adsorption of gases on plane surfaces of glass, mica and platinium.

Lax, P. and Ritchmyer, R. (1956). Survey of the stability of linear finite difference equations. *Communications on pure and applied mathematics*, 9:267–293.

Li, Q., Rao, J., and Fazio, P. (2009). Development of HAM tool for building envelope analysis. *Building and Environment*, 44(5):1065–1073.

Li, Y., Fazio, P., and Rao, J. (2012). An investigation of moisture buffering performance of wood paneling at room level and its buffering effect on a test room. *Building and Environment*, 47:205–216.

Lorente, S. (2017). The constructal law as an approach to address energy efficiency in the urban fabric. In *Constructal Law And Second Law Conference*, Bucharest, Romania.

Loveday, D. L. and Taki, A. H. (1996). Convective heat transfer coefficients at a plane surface on a full-scale building facade. *International Journal of Heat and Mass Transfer*, 39(8):1729–1742.

Luikov, A. (1975). Systems of differential equations of heat and mass transfer in capillary-porous bodies. *International Journal of Heat and Mass Transfer*, 18:1–14.

Macal, C. and North, M. (2010). Tutorial on agent-based modelling and simulation. *Journal of Simulation*, 4:151–162.

Maier, T., Krzaczek, M., and Tejchman, J. (2009). Comparison of physical performances of the ventilation systems in low-energy residential houses. *Energy and Buildings*, 41(3):337–353.

Maqsoud, A., Bussière, B., Mbonimpa, M., and Aubertin, M. (2006). Hysteresis effect on the water retention curve: a comparison between laboratory results and predictive models. In *57 congrès canadien de géotechnique*.

Mcgregor, F., Fabbri, A., Ferreira, J., Simoes, T., Faria, P., and Morel, J.-C. (2009). Procedure to determine the impact of the surface film resistance on the hygric properties of composite clay/fibre plasters. *Materials and Structures*, 50.

McGregor, F., Heath, A., Shea, A., and Lawrence, M. (2014). The moisture buffering capacity of unfired clay masonry. *Building and Environment*, 82:599–607.

Meeus, J. (1998). *Astronomical Algorithms*. Errata, 2 edition.

Mendes, N. and Philippi, P. (2005). A method for predicting heat and moisture transfer through multilayered walls based on temperature and moisture content gradients. *International Journal of Heat and Mass Transfer*, 48(1):37–51.

Minkowycz, W., Sparrow, E., and Murthy, J. (2006). *Handbook of Numerical Heat Transfer*. Wiley & Sons, Inc, 2 edition.

Miranville, F. (2002). *Contribution à l'Etude des Parois Complexes en Physique du Bâtiment : Modélisation, Expérimentation et Validation Expérimentale de Complexes de Toitures incluant des Produits Minces Réfléchissants en climat tropical humide*. PhD thesis, Université de La Réunion.

Mualem, Y. (1984). A modified dependent-domain theory of hysteresis. *Soil Science*, 137:250–257.

Newsham, G., Mahdavi, A., and Beausoleil-Morrison, I. (1995). Lightswitch: a stochastic model for predicting office lighting energy consumption. In *Right Light Three, The Third European Conference on Energy Efficient Lighting*, pages 60–66, Newcastle-upon-Tyne, UK.

Nicolas, V., Salagnac, P., Glouannec, P., Ploteau, J.-P., Jury, V., and Boillereaux, L. (2014). Modelling heat and mass transfer in deformable porous media: Application to bread baking. *Journal of Food Engineering*, 130:23–35.

Nielsen, K. (2003). Mycotoxin production by indoor molds. *Fungal Genet. Biol.*, 39(2):103–117.

Nouidui, T., Wetter, M., and Zuo, W. (2014). Functional mock-up unit for co-simulation import in energyplus. *Journal of Building Performance Simulation*, 7(3).

Ojanen, T., Viitanen, H., Peuhkuri, R., Lahdesmaki, K., Vinha, J., and Salminen, K. (2010). Mold growth modeling of building structures using sensitivity classes of materials. In *Proceeding Building XI*, Florida, USA.

Oswin, C. (1946). The kinetics of package life. III. The isotherm. *Journal of the Society of Chemical Industry*, 65(12):416–421.

Oumeziane, Y. A. (2013). *Evaluation des performances hygrothermiques d'une paroi par simulation numérique: application aux parois en béton de chanvre*. PhD thesis, INSA de Rennes.

Page, J. (2007). *Simulating occupant presence and behaviour in buildings*. PhD thesis, Ecole Polytechnique de Lausanne, Switzerland.

Page, J., Robinson, D., Morel, N., and Scartezzini, J.-L. (2008). A generalised stochastic model for the simulation of occupant presence. *Building and Environment*, 40:83–98.

Patankar, S. V. (1980). *Numerical Heat Transfer and Fluid Flow*. Hemisphere Publishing Corporation.

Patankar, S. V. and Baliga, B. R. (1978). A New Finite-Difference Scheme for Parabolic Differential Equations. *Numerical Heat Transfer Part B - Fundamentals*, 1:27–37.

Pedersen, C. R. (1990). *Combined Heat and Moisture Transfer in Building Constructions*. PhD thesis, Technical University of Denmark, Denmark.

Perez-Lombard, L., Ortiz, J., and Maestre, I. (2011). The map of energy flow in HVAC systems. *Applied Energy*, 88:5020–5031.

Peuhkuri, R. (2003). *Moisture Dynamics in Building Envelopes*. PhD thesis, Technical University of Denmark.

Philip, J. and De Vries, D. (1957). Moisture movement in porous materials under temperature gradients. *Transactions, American Geophysical Union*, 38(2):222–232.

Piot, A. (2009). *Hyrothermique du bâtiment : expérimentation sur une maison à ossature bois en conditions climatiques naturelles et modélisation numérique*. PhD thesis, Institut National des Sciences Appliquées de Lyon.

Plathner, P. and Woloszyn, M. (2002). Interzonal air and moisture transport in a test house. experiment and modelling. *Buildings and Environment*, 37(2):189–199.

Pérez-Lombard, L., Ortiz, J., and Pout, C. (2008). A review on buildings energy consumption information. *Energy and Buildings*, 40:394–398.

Qin, M. (2010). *Whole Building Heat, Air and Moisture Transfer*. USA, LAP LAMBERT edition.

Qin, M., Walton, G., Belarbi, R., and Allard, F. (2011). Simulation of whole building coupled hygrothermal-airflow transfer in different climates. *Energy and Conversion Management*, 52:1470–1478.

Raoui, A., Mouhous, S., Malek, A., and Benyoucef, B. (2011). Etude statistique du rayonnement solaire à alger. *Revue des Energies Renouvelables*, 14(4):637–648.

Reinhart, C. (2004). Lightswitch-2002: a model for manual and automated control of electric lighting and blinds. *Solar Energy*, 77(1):15–28.

Robinson, D. (2006). Some trends and research needs in energy and comfort prediction. In *Comfort and Energy Use in Buildings*, Windsor, United Kingdom.

Rode, C., Peukhuri, R., Hansen, K. K., Time, B., Svennberg, K., Arfvidsson, J., and Ojanen, T. (2005). Nordtest project on moisture buffer value of materials. In *Energy performance regulation*, Brussels, Belgium.

Rose, W. (2003). The rise of the diffusion paradigm in the US. *Research in Building Physics: Proceedings of the Second International Conference on Building Physics*, 27(4):327–334.

RT Bâtiment (2012). RT neuf 2012: Données météorologiques. `http://www.rt-batiment.fr/batiments-neufs/reglementation-thermique-2012/donnees-meteorologiques.html`, accessed 6.14.17.

Sakamoto, Y., Matsuo, Y., Nagata, A., and Kim, H. (1996). Effect of the moisture sorption of miscellaneous room goods on latent heat load and humidity part-2 simulation analysis on the effects of the moisture sorption. In *Summaries of technical papers of annual meeting Architectural Institute of Japan*, Japan.

Savin, J., Berthin, S., and Jardinier, M. (2005). Assessment of improvement brought by humidity sensitive and hybrid ventilation/hr-vent project. In *Proceedings of 26th AIVC conference on ventilation in relation to the energy performance of buildings*, pages 157–167, Brussels, Belgium.

Scheffler, G. (2008). *Validation of hygrothermal material modelling under consideration of the hysteresis of moisture storage*. PhD thesis, Dresden University of Technology, Dresden.

Scheffler, G. A. and Plagge, R. (2009). A whole range hygric material model: Modelling liquid and vapour transport properties in porous media. *International Journal of Heat and Mass Transfer*, 53(1–3):286–296.

Schellen, H., Van Schijndel, A., and Briggen, P. (2008). The use of COMSOL for building constructions engineering regarding heat and moisture transport. In *Excerpt from the Proceedings of the COMSOL Conference*.

Schijndel, A. W. M. v. (2007). *Integrated heat air and moisture modeling and simulation*. Technische Universiteit Eindhoven.

Sedlbauer, K. (2001). *Prediction of mould fungus formation on the surface of and inside building components*. PhD thesis, Frauhnofer Institute for Building Physics, Munich, Germany.

Seligman, C., Darley, J., and Becker, L. (1978). Behavioral approaches to residential energy conservation. *Energy and Buildings*, 1:325–337.

Seng, B., Lorente, S., and Magniont, C. (2017). Scale analysis of heat and moisture transfer through bio-based materials - application to hemp concrete. *Energy and Buildings*, 155:546–558.

Sharples, S. (1984). Full-scale measurements of convective energy losses from exterior building surfaces. *Building and Environment*, 19(1):31–39.

Smith, S. (1947). The sorption of water Vapor by High Polymers. *J. Am. Chem. Soc.*, 69(3):646–651.

Soderlind, G. and Wang, L. (2003). Adaptive time-stepping and computational stability. *Journal of Computational Methods in Sciences and Engineering*, 2(3):1–3.

Spencer, J. (1971). Fourier series representation of the position of the sun. *Search*, 2(5):172.

Steeman, H.-J., Van Belleghem, M., Janssens, A., and De Paepe, M. (2009). Coupled simulation of heat and moisture transport in air and porous materials for the assessment of moisture related damage. *Building and Environment*, 44(10):2176–2184.

Sulaiman, H. and Olsina, F. (2014). Comfort reliability evaluation of building designs by stochastic hygrothermal simulation. *Renewable and Sustainable Energy Reviews*, 40:171–184.

Tariku, F., Kumaran, K., and Fazio, P. (2010). Transient model for coupled heat, air and moisture transfer through multilayered porous media. *International Journal of Heat and Mass Transfer*, 53(15-16):3035–3044.

Teesdale, L. (1937). Condensation in walls and attics. *Forest Products Laboratory, Madison WI.*

TenWolde, A. and Walker, I. (2001). Interior moisture design loads for residences. In *Proceedings of thermal performance of exterior envelopes of buildings VIII, ASHRAE*, Atlanta, GA.

Van Belleghem, M., Steeman, M., Janssen, H., Janssens, A., and De Paepe, M. (2014). Validation of a coupled heat, vapour and liquid moisture transport model for porous materials implemented in CFD. *Building and Environment*, 81:340–353.

van Rossum, G. (1995). Python tutorial, technical report CS-R9526. In *Centrum voor Wiskunde en Informatica (CWI)*, Amsterdam.

van Schijndel, A. (2011). Multiphysics modeling of building physical constructions. *Building Simulations*, 4(1):49–60.

Vereecken, E. and Roels, S. (2012). Review of mould prediction models and their influence on mould risk evaluation. *Building and Environment*, 51:296–310.

Vereecken, E., Roels, S., and Janssen, H. (2011). In situ determination of the moisture buffer potential of room enclosures. *Building and Environment*, 34(3):223–246.

Vorger, E. (2014). *Etude de l'influence du comportement des habitants sur la performance énergétique du bâtiment*. PhD thesis, Ecole nationale supérieure des mines de Paris.

Walker, I. and Sherman, M. (2006). Evaluation of existing technologies for meeting residential ventilation requirements. lawrence berkeley national laboratory, berkeley, ca. lbnl 59998.

Walker, I. S. and Sherman, M. H. (2007). Humidity implications for meeting residential ventilation requirements. In *Lawrence Berkley National Laboratory*, Berkley, California.

Wang, C., Yan, D., and Jiang, Y. (2011). A novel approach for building occupancy simulation. *Building Simulation*, 4:149–167.

Wang, D., Federspiel, C., and Rubinstein, F. (2005). Modelling occupancy in single person offices. *Energy and Buildings*, 37:121–126.

Widen, J., Lundh, M., Vassileva, I., Dahlquist, E., Ellegard, K., and Wackelgard, E. (2015). Constructing load profiles for household electricity and hot water from time-use data - modelling approach and validation. *Energy and Buildings*, 87:348–359.

Wilke, U. (2013). *Probabilistic bottom-up modelling of occupancy and activities to predict electricity demand in residential buildings*. PhD thesis, Ecole polytechnique fédérale de Lausanne.

Williams Portal, N. (2011). Evaluation of heat and moisture induced stress and strain of historic building materials and artefacts. In *12th Conference of International Building Simulation Association*, Sydney, Australia.

Wolkoff, P. and Soren, K. K. (2007). The dichotomy of relative humidity on indoor air quality. *Environment International*, 33(6):850–857.

Woloszyn, M., Kalamees, T., Olivier Abadie, M., Steeman, M., and Sasic Kalagasidis, A. (2009). The effect of combining a relative-humidity-sensitive ventilation system with the moisture-buffering capacity of materials on indoor climate and energy efficiency of buildings. *Building and Environment*, 44(3):515–524.

Woloszyn, M. and Rode, C. (2008). Tools for performance simulation of heat, air and moisture conditions of whole buildings. *Building Simulation*, 1(1):5–24.

Yang, X., Fazio, P., Ge, H., and Rao, J. (2012). Evaluation of moisture buffering capacity of interior surface materials and furniture in a full-scale experimental investigation. *Building and Environment*, 47:188–196.

Yoshino, H., Mitamura, T., and Hasegawa, K. (2009). Moisture buffering and effect of ventilation rate and volume rate of hygrothermal materials in a single room under steady state exterior conditions. *Building and Environment*, 44:1418–1425.

Zhang, H., Yoshino, H., Hasegawa, K., Liu, J., Zhang, W., and Xuan, H. (2017). Practical moisture buffering effect of three hygroscopic materials in real-world conditions. *Energy and Buildings*, 139:214–223.

Zhang, X., Zillig, W., Künzel, H. M., Zhang, X., and Mitterer, C. (2015). Evaluation of moisture sorption models and modified Mualem model for prediction of desorption isotherm for wood materials. *Building and Environment*, 92:387–395.

Zhang, Z., Thiéry, M., and Baroghel-Bouny, V. (2014). A review and statistical study of existing hysteresis models for cementitious materials. *Cement and Concrete Research*, 57:44–60.

Appendices

Appendix A

Numerical discretisation of the coupled heat and moisture transfer equations

The coupled heat and moisture transfer equations can be expressed in the following fashion (Eq. (A.1) for the mass conservation and Eq. (A.2) for the energy conservation). Note that the energy conservation equation was combined with the source term in order to have a set of two equations instead of three:

$$C_{11}\frac{\partial p_c}{\partial t} = R_{11}\frac{\partial^2 p_c}{\partial x^2} + R_{12}\frac{\partial^2 T}{\partial x^2} + \frac{\partial R_{11}}{\partial x}\frac{\partial p_c}{\partial x} + \frac{\partial R_{12}}{\partial x}\frac{\partial T}{\partial x} \tag{A.1}$$

where:

$$C_{11} = \frac{\partial w}{\partial p_c}$$

$$R_{11} = -\left(\delta_l + \delta_v \frac{\rho_v}{\rho_l}\right)$$

$$R_{12} = \delta_v \left(\Psi \frac{\partial p_{sat}}{\partial T} - p_v \frac{ln(\Psi)}{T}\right)$$

$$\begin{aligned} C_{22}\frac{\partial T}{\partial t} + C_{21}\frac{\partial p_c}{\partial t} =& R_{22}\frac{\partial^2 T}{\partial x^2} + \frac{\partial R_{22}}{\partial x}\frac{\partial T}{\partial x} + R_{21}\frac{\partial^2 p_c}{\partial x^2} + \frac{\partial R_{21}}{\partial x}\frac{\partial p_c}{\partial x} \\ &+ r_1\left(\frac{\partial T}{\partial x}\right)^2 + r_2\frac{\partial T}{\partial x}\frac{\partial p_c}{\partial x} \end{aligned} \tag{A.2}$$

where:

$C_{22} = \rho_{mat} c_{p,mat} + w c_{p,l}$

$C_{21} = [(c_{p,l} - c_{p,v})T - L_v] \left(\frac{1}{1 - \frac{\rho_v}{\rho_l}} \right) \frac{\partial w}{\partial p_c}$

$R_{22} = k_{mat}$

$R_{21} = -[(c_{p,l} - c_{p,v})T - L_v]\delta_l$

$r_1 = c_{p,v}\delta_v \left(\Psi \frac{\partial p_{sat}}{\partial T} - p_v \frac{ln(\Psi)}{T} \right)$

$r_2 = -\left(c_{p,l}\delta_l + c_{p,v}\delta_v \frac{\rho_v}{\rho_l} \right)$

The global water content w intervenes in the coefficient C_{22} regrouping the vapour content w_v and liquid w_l content. Since it is not possible to differentiate both of these terms, the following assumption is made:

$$C_{22} \approx \rho_{mat} c_{p,mat} + w c_{p,l}$$

In this section , the variable u refers to the driving potential T or p_c, j refers to the time and i to a node.

A.1 Linearisation

A.1.1 General formulation

Equation (A.2) is non linear and has to be linearized in order to be solved by numerical methods. The linearisation method applied here relies on a first order Taylor series expansion which is formulated as follows:

I is an interval of $\mathbb{R}$, $(x_0, y_0) \in I^2$, E is a normalized vector space and f is a function of I in E differentiable in (x_0, y_0) at the first order; then for all $(x, y) \in I^2$:

$$\begin{cases} f(x) = f(x_0) + \frac{df(x_0)}{dx}(x - x_0) \\ f(x, y) = f(x_0, y_0) + \frac{\partial f(x_0, y_0)}{\partial x}(x - x_0) + \frac{\partial f(x_0, y_0)}{\partial y}(y - y_0) \end{cases}$$

Hence, the calculation of x at the time j is done by using its value at the previous time step $j - 1$ (meaning x_0).

A.1.2 Linearisation of the energy conservation equation

The linearisation of $\left(\frac{\partial T}{\partial x}\right)^2$ was done with a Taylor series expansion for a one-variable function f. The Taylor series expansion at the first order gives:

$$\begin{aligned}\left(\frac{\partial T}{\partial x}\bigg|^{j}\right)^2 &\approx \left(\frac{\partial T}{\partial x}\bigg|^{j-1}\right)^2 + 2\,\frac{\partial T}{\partial x}\bigg|^{j-1}\left(\frac{\partial T}{\partial x}\bigg|^{j} - \frac{\partial T}{\partial x}\bigg|^{j-1}\right)\\ &= q_0\,\frac{\partial T}{\partial x}\bigg|^{j} + q_0\end{aligned} \tag{A.3}$$

With:

$$q_0 = 2\,\frac{\partial T}{\partial x}\bigg|^{j-1}$$

$$q_1 = -\left(\frac{\partial T}{\partial x}\bigg|^{j-1}\right)^2$$

The linearisation of $\frac{\partial T}{\partial x}\frac{\partial p_c}{\partial x}$ was done with a Taylor series expansion for a two-variables function:

$$\begin{aligned}&\frac{\partial T}{\partial x}\bigg|^{j}\,\frac{\partial p_c}{\partial x}\bigg|^{j} \approx \frac{\partial T}{\partial x}\bigg|^{j-1}\,\frac{\partial p_c}{\partial x}\bigg|^{j-1} + \frac{\partial T}{\partial x}\bigg|^{j-1}\left(\frac{\partial p_c}{\partial x}\bigg|^{j} - \frac{\partial p_c}{\partial x}\bigg|^{j-1}\right)\\ &+ \frac{\partial p_c}{\partial x}\bigg|^{j-1}\left(\frac{\partial T}{\partial x}\bigg|^{j} - \frac{\partial T}{\partial x}\bigg|^{j-1}\right)\\ &= \frac{\partial T}{\partial x}\bigg|^{j}\,\frac{\partial p_c}{\partial x}\bigg|^{j} \approx p_0\,\frac{\partial T}{\partial x}\bigg|^{j} + p_1\,\frac{\partial p_c}{\partial x}\bigg|^{j} + p_2\end{aligned} \tag{A.4}$$

where:

$$p_0 = \frac{\partial p_c}{\partial x}\bigg|^{j-1}$$

$$p_1 = \frac{\partial T}{\partial x}\bigg|^{j-1}$$

$$p_2 = -\,\frac{\partial T}{\partial x}\bigg|^{j-1}\,\frac{\partial p_c}{\partial x}\bigg|^{j-1}$$

By implementing (A.3) and (A.4) in (A.2), a new equation is deduced:

$$C_{22}\frac{\partial T}{\partial t} + C_{21}\frac{\partial p_c}{\partial t} = R_{22}\frac{\partial^2 T}{\partial x^2} + R_{21}\frac{\partial^2 p_c}{\partial x^2} + R_1\frac{\partial T}{\partial x} + R_2\frac{\partial p_c}{\partial x} + R_3 \tag{A.5}$$

where:

$$R_1 = r_1 q_0 + r_2 p_0 + \frac{\partial R_{22}}{\partial x}$$
$$R_2 = r_2 p_1 + \frac{\partial R_{21}}{\partial x}$$
$$R_3 = r_1 q_1 + r_2 p_2$$

Finally, the coupled heat and mass transfer system is described by equations (A.1) and (A.5).

A.1.3 Linearisation of the exterior boundary conditions

The convective mass transfer is a function of the exterior vapour pressure and the surface capillary pressure. However, the latter is in a exponential function which has to be linearized. f is a continuous and differentiable function on $\mathbb{R}$ and is defined as follows:

$$f : \mathbb{R} \to \mathbb{R}$$
$$f : p_c \mapsto p_{sat}(T) \cdot exp\left(\frac{-p_c}{\rho_l R_v T}\right)$$
$$\frac{df}{dx} : f \mapsto -\frac{p_{sat}(T)}{\rho_l R_v T} \cdot exp\left(\frac{-p_c}{\rho_l R_v T}\right)$$

A first order Taylor expansion gives:

$$p_{sat}(T_{es}^j) \cdot exp\left(\frac{-p_{c,es}^j}{\rho_l R_v T_{es}^j}\right) \approx k_0 \cdot p_{c,es}^j + k_1 \tag{A.6}$$

where:

$$k_0 = -\frac{p_{sat}(T_{es}^{j-1})}{\rho_l R_v T_{es}^{j-1}} \cdot exp\left(\frac{-p_{c,es}^{j-1}}{\rho_l R_v T_{es}^{j-1}}\right)$$
$$k_1 = exp\left(\frac{-p_{c,es}^{j-1}}{\rho_l R_v T_{es}^{j-1}}\right)\left(p_{sat}(T_{es}^{j-1}) + \frac{p_{sat}(T_{es}^{j-1})}{\rho_l R_v T_{es}^{j-1}} p_{c,es}^{j-1}\right)$$

Then, injecting (A.6) in (A.7) yields:

$$g_{conv} = -h_{m,e} k_0 p_{c,se} + h_{m,e} p_{v,se} - h_{m,e} k_1 \tag{A.7}$$

Equation (A.7) was also used and validated by Van Belleghem et al. (2014).

A.2 Spatial discretisation

Figure A.1 gives the nomenclature for a non-uniform mesh.

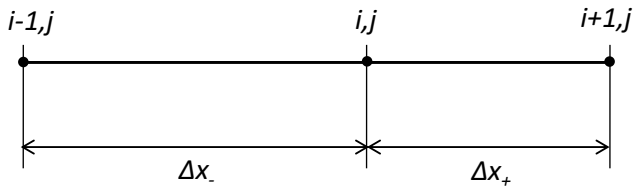

Figure A.1 – Nomenclature for a non uniform mesh grid

A forward Taylor series expansion applied to u gives:

$$u_{i+1} = u_i + \left.\frac{\partial u}{\partial x}\right|_i \Delta x_+ + \left.\frac{\partial^2 u}{\partial x^2}\right|_i \frac{(\Delta x_+)^2}{2!} + \left.\frac{\partial^3 u}{\partial x^3}\right|_i \frac{(\Delta x_+)^3}{3!} + \cdots + \text{truncation error} \tag{A.8}$$

A backward Taylor series expansion applied to u gives:

$$u_{i-1} = u_i - \left.\frac{\partial u}{\partial x}\right|_i \Delta x_- + \left.\frac{\partial^2 u}{\partial x^2}\right|_i \frac{(\Delta x_-)^2}{2!} - \left.\frac{\partial^3 u}{\partial x^3}\right|_i \frac{(\Delta x_-)^3}{3!} + \cdots + \text{truncation error} \tag{A.9}$$

Summing Eqs. (A.8) and (A.9) gives a centered difference for the second order derivative of u:

$$\left.\frac{\partial^2 u}{\partial x^2}\right|_i = \frac{2}{\Delta x_+ + \Delta x_-}\left(\frac{u_{i+1} - u_i}{\Delta x_+} - \frac{u_i - u_{i-1}}{\Delta x_-}\right) + O(\Delta x) \tag{A.10}$$

Similarly, by subtracting Eqs. (A.8) and (A.9) a centered difference for the first order derivative of u is deducted:

$$\frac{\partial u}{\partial x} = \frac{u_{i+1} - u_i}{2\Delta x_+} - \frac{u_{i-1} - u_i}{2\Delta x_-} + O(\Delta x)^2 \tag{A.11}$$

Eq. (A.10) has a first order truncation error. When $\Delta x_+ \to \Delta x_-$ it becomes of the second order ($O(\Delta x)^2$) (Minkowycz et al., 2006).

These last two equations do not take into consideration the variation of the coefficients in front of the derivative of the driving potential. To do so, a control volume balance around the node i gives (example for a coefficient R):

$$\left.\frac{\partial^2 u}{\partial x^2}\right|_i = \frac{2}{\Delta x_+ + \Delta x_-}\left(R_{i+1/2}\frac{u_{i+1} - u_i}{\Delta x_+} - R_{i-1/2}\frac{u_i - u_{i-1}}{\Delta x_-}\right) + O(\Delta x) \tag{A.12}$$

$$\frac{\partial u}{\partial x} = R_{i+1/2}\frac{u_{i+1} - u_i}{2\Delta x_+} - R_{i-1/2}\frac{u_{i-1} - u_i}{2\Delta x_-} + O(\Delta x)^2 \tag{A.13}$$

where:

$$R_{i+1/2} = \frac{R_i + R_{i+1}}{2}$$
$$R_{i-1/2} = \frac{R_i + R_{i-1}}{2}$$

A.3 Temporal discretisation

A conventional "forward" difference in time was used for the temporal discretisation:

$$\frac{u_i^{j+1} - u_i^j}{\Delta t} \tag{A.14}$$

A.4 Resolution scheme

A.4.1 General case

Figure A.2 presents the nomenclature of the mesh grid chosen.

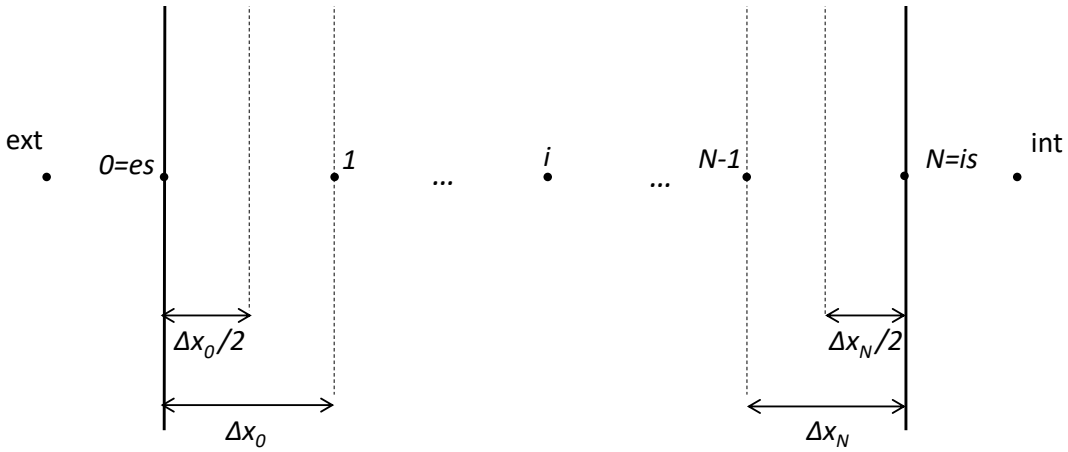

Figure A.2 – Nomenclature of the mesh grid in a wall

Sections A.2 and A.3 presented the spatial and temporal discretisation of the coupled heat and mass transfer equations. As explained in Chapter 2, an implicit method was selected. To simplify the equations, the derivative of the coefficients R are not considered here. The method used relies on the one described in Minkowycz et al. (2006) and Patankar (1980).

The mass conservation equation is discretised as follows:

$$\frac{C_{11}}{\Delta t} p_{c,i}^j = a_0 p_{c,i+1}^{j+1} + a_1 p_{c,i}^{j+1} + a_2 p_{c,i-1}^{j+1} + b_0 T_{i+1}^{j+1} + b_1 T_i^{j+1} + b_2 T_{i-1}^{j+1} \tag{A.15}$$

where:

$$a_0 = -\frac{R_{11,i} + R_{11,i+1}}{\Delta x_+(\Delta x_+ + \Delta x_-)}$$
$$a_1 = \frac{1}{\Delta x_+ + \Delta x_-}\left(\frac{R_{11,i} + R_{11,i+1}}{\Delta x_+} + \frac{R_{11,i} + R_{11,i-1}}{\Delta x_-}\right) + \frac{C_{11,i}}{\Delta t}$$
$$a_2 = -\frac{R_{11,i} + R_{11,i-1}}{\Delta x_-(\Delta x_+ + \Delta x_-)}$$
$$b_0 = -\frac{R_{12,i} + R_{12,i+1}}{\Delta x_+(\Delta x_+ + \Delta x_-)}$$
$$b_1 = \frac{1}{\Delta x_+ + \Delta x_-}\left(\frac{R_{12,i} + R_{12,i+1}}{\Delta x_+} + \frac{R_{12,i} + R_{12,i-1}}{\Delta x_-}\right)$$
$$b_2 = -\frac{R_{12,i} + R_{12,i-1}}{\Delta x_-(\Delta x_+ + \Delta x_-)}$$

Similarly, the energy conservation equation is discretised as follows:

$$\frac{C_{22}}{\Delta t}T_i^j + \frac{C_{21}}{\Delta t}p_{c,i}^j = a_3 p_{c,i+1}^{j+1} + a_4 p_{c,i}^{j+1} + a_5 p_{c,i-1}^{j+1} + b_3 T_{i+1}^{j+1} + b_4 T_i^{j+1} + b_5 T_{i-1}^{j+1} \quad \text{(A.16)}$$

where:

$$a_3 = -\frac{R_{21,i} + R_{21,i+1}}{\Delta x_+(\Delta x_+ + \Delta x_-)} - \frac{R_{2,i} + R_{2,i+1}}{4\Delta x_+}$$
$$a_4 = \frac{1}{\Delta x_+ + \Delta x_-}\left(\frac{R_{21,i} + R_{21,i+1}}{\Delta x_+} + \frac{R_{21,i} + R_{21,i-1}}{\Delta x_-}\right) + \frac{R_{2,i} + R_{2,i+1}}{4\Delta x_+} - \frac{R_{2,i} + R_{2,i-1}}{4\Delta x_-} + \frac{C_{21,i}}{\Delta t}$$
$$a_5 = -\frac{R_{21,i} + R_{21,i-1}}{\Delta x_-(\Delta x_+ + \Delta x_-)} + \frac{R_{2,i} + R_{2,i-1}}{4\Delta x_-}$$
$$b_3 = -\frac{R_{22,i} + R_{22,i+1}}{\Delta x_+(\Delta x_+ + \Delta x_-)} - \frac{R_{1,i} + R_{1,i+1}}{4\Delta x_+}$$
$$b_4 = \frac{1}{\Delta x_+ + \Delta x_-}\left(\frac{R_{22,i} + R_{22,i+1}}{\Delta x_+} + \frac{R_{22,i} + R_{22,i-1}}{\Delta x_-}\right) + \frac{R_{1,i} + R_{1,i+1}}{4\Delta x_+} - \frac{R_{1,i} + R_{1,i-1}}{4\Delta x_-} + \frac{C_{22,i}}{\Delta t}$$
$$b_5 = -\frac{R_{22,i} + R_{22,i-1}}{\Delta x_-(\Delta x_+ + \Delta x_-)} + \frac{R_{1,i} + R_{1,i-1}}{4\Delta x_-}$$

A.4.2 Exterior boundary conditions

A control volume balance on the surface of the material leads to:

$$C_{11,0}\frac{\Delta x_0}{2}\frac{p_{c,0}^{j+1} - p_{c,0}^j}{\Delta t} = R_{11,0}\frac{p_{c,1}^{j+1} - p_{c,0}^{j+1}}{\Delta x} + R_{12,0}\frac{T_1^{j+1} - T_0^{j+1}}{\Delta x} + g_{conv} \quad \text{(A.17)}$$

Developing each term and organizing this equation yields:

$$\begin{aligned}&\frac{C_{11,0}}{\Delta t}p_{c,0}^{j}+\frac{2h_{m,ext}}{\Delta x_0}p_{v,ext}^{j}-\frac{2h_{m,ext}^{j}k_1}{\Delta x_0}=-\frac{2R_{11,0}}{\Delta x_0^2}p_{c,1}^{j+1}\\&+\left(\frac{2R_{11,0}}{\Delta x_0^2}+\frac{C_{11,0}}{\Delta t}+\frac{2h_{m,ext}k_0}{\Delta x_0}\right)p_{c,0}^{j+1}-\frac{2R_{12,0}}{\Delta x_0^2}T_1^{j+1}+\frac{2R_{12,0}}{\Delta x_0^2}T_0^{j+1}\end{aligned}\tag{A.18}$$

The same equation can be used for the interior boundary conditions by changing the subscripts ext, 0 and 1 by respectively int, N and $N-1$ (refer to Figure A.2).

Similarly to the mass conservation exterior boundary conditions, a control volume balance on the surface of the material leads to:

$$\begin{aligned}&C_{22,0}\frac{\Delta x_0}{2}\frac{T_0^{j+1}-T_0^{j}}{\Delta t}+C_{21,0}\frac{\Delta x_0}{2}\frac{p_{c,0}^{j+1}-p_{c,0}^{j}}{\Delta t}=R_{22,0}\frac{T_1^{j+1}-T_0^{j+1}}{\Delta x}\\&+R_{21,0}\frac{p_{c,1}^{j+1}-p_{c,0}^{j+1}}{\Delta x}+T_0R_{1,0}\frac{T_1^{j+1}-T_0^{j+1}}{\Delta x}+T_0R_{2,0}\frac{p_{c,1}^{j+1}-p_{c,0}^{j+1}}{\Delta x}\\&+q_{h,conv}+q_{m,conv}+q_{LWR}+q_{SWR}\end{aligned}\tag{A.19}$$

Developing each term and organizing this equation yields:

$$\begin{aligned}&\frac{C_{22,0}}{\Delta t}T_0^{j}+\frac{C_{21,0}}{\Delta t}p_{c,0}^{j}+\frac{2}{\Delta x_0}h_{h,ext}^{j}T_e^{j}+\frac{2}{\Delta x_0}h_{eq,ext}^{j}p_{v,ext}^{j}-\frac{2h_{m,e}^{j}k_1}{\Delta x_0}\\&+\frac{2}{\Delta x_0}h_{r,gro}^{j}T_{gro}^{j}+\frac{2}{\Delta x_0}h_{r,sky}^{j}T_{sky}^{j}+\kappa(Dir^{j}+Dif^{j}+Ref^{j})\\&=-\frac{2(R_{22,0}+T_0R_{1,0})}{\Delta x_0^2}T_1^{j+1}\\&+\left[\frac{2(R_{22,0}+T_0R_{1,0})}{\Delta x_0^2}+\frac{2(h_{h,ext}+h_{r,gro}+h_{r,sky})}{\Delta x_0}+\frac{C_{22,0}}{\Delta t}\right]T_0^{j+1}\\&-\frac{2(R_{21,0}+T_0R_{2,0})}{\Delta x_0^2}p_{c,1}^{j+1}+\left[\frac{2(R_{21,0}+T_0R_{2,0})}{\Delta x_0^2}+\frac{2k_0h_{eq,ext}}{\Delta x_0}+\frac{C_{21,0}}{\Delta t}\right]p_{c,0}^{j+1}\end{aligned}\tag{A.20}$$

The same equation can be used for the interior boundary conditions by changing the subscripts e, 0 and 1 by respectively i, N and $N-1$; and by removing all the terms relative to the radiative heat transfer.

A.4.3 Interior boundary conditions

Contrarily to the exterior boundary conditions, a source term was taken into account for the interior boundary conditions. A discretisation method for a fully implicit scheme with a source term can be found in Becker and Kaus (2013). The

indoor mass balance can be expressed as follows:

$$C_{1,int}\frac{\partial p_v}{\partial t} = R_{1,int}p_{v,int} + R_{2,int}p_{v,is} + R_{3,int}p_{v,ext} + \dot{m}_{int} \tag{A.21}$$

with:

$$C_{1,int} = \frac{R_a}{R_v}\cdot\frac{\rho_{air}V}{p_{atm}-p_{v,int}}$$
$$R_{1,int} = -\left(A\cdot h_{m,int} + \frac{R_{da}}{R_v}\cdot\frac{n\rho_{air}V}{p_{atm}-p_{v,int}}\right)$$
$$R_{2,int} = A\cdot h_{m,int}$$
$$R_{3,int} = \frac{R_a}{R_v}\cdot\frac{n\rho_{air}V}{p_{atm}-p_{v,ext}}$$

The discretised equation is:

$$\frac{C_{1,int}}{\Delta t}p^j_{v,i} + R_{3,int}p^j_{v,ext} + \dot{m}^j_{int} + R_{2,int}p^j_{v,is} = (-R_{1,int} + \frac{C_{1,int}}{\Delta t})p^{j+1}_{v,int} \tag{A.22}$$

Similarly, the indoor energy balance becomes:

$$C_{2,int}\frac{\partial T_i}{\partial t} = R_{4,int}T_i + R_{5,int}T_{is} + R_{6,int}T_e + \dot{Q}_{int} \tag{A.23}$$

with:

$$C_{2,int} = \rho_{air}C_{p,air}V$$
$$R_{4,int} = -(A\cdot h_{h,int} + nV\rho_{air}c_{p,air})$$
$$R_{5,int} = A\cdot h_{h,int}$$
$$R_{6,int} = nV\rho_{air}c_{p,air}$$

The discretised equation is:

$$\frac{C_{2,int}}{\Delta t}T^j_{int} + R_{6,int}T^j_{ext} + \dot{Q}^j_{int} + R_{5,int}T^j_{is} = \left(-R_{4,int} + \frac{C_{2,int}}{\Delta t}\right)T^{j+1}_{int} \tag{A.24}$$

A.4.4 Matrix system

Eqs. (A.15), (A.16), (A.18), (A.20), (A.21) and (A.24) characterise the coupled heat ans mass transfer model discretised. Therefore, these equations described the following matrix system:

$$[Res][U]^{j+1} = [Capa][U]^j + [B][L] + [Rad] + [S] + [R] + [K] \tag{A.25}$$

where:

- $[RES]$ is the resistance matrix containing all of the R parameters;

- $[U]^{j+1}$ is the driving potentials vector at the time step $j+1$;
- $Capa$ is the capacity matrix containing all of the C parameters;
- $[U]^{j}$ is the driving potentials vector at the time step j;
- $[B]$ is the convective boundary conditions coefficient vector;
- $[L]$ is the vector reading the boundary conditions (water vapour pressure and temperature);
- $[Rad]$ is the exterior radiative boundary conditions vector;
- $[S]^{j+1}]$ is the source vector (at the time step $j+1$ for an implicit scheme);
- $[R]$ contains the constant coming from the linearisation of the energy conservation conservation;
- $[K]$ contains the constant coming from the linearisation of the boundary conditions.

Solving this system can be done by inverting the matrice $[Res]$, but we favoured a LU decomposition as it is computationally less expensive and faster.

Appendix B

Climate data

B.1 Trappes

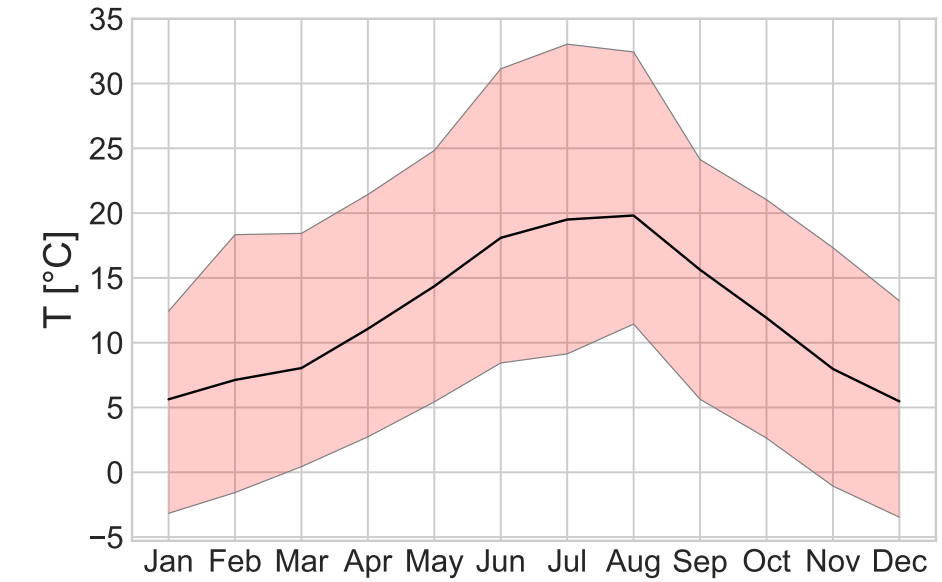

Figure B.1 – Yearly temperature in Trappes: average temperature and temperature range in red

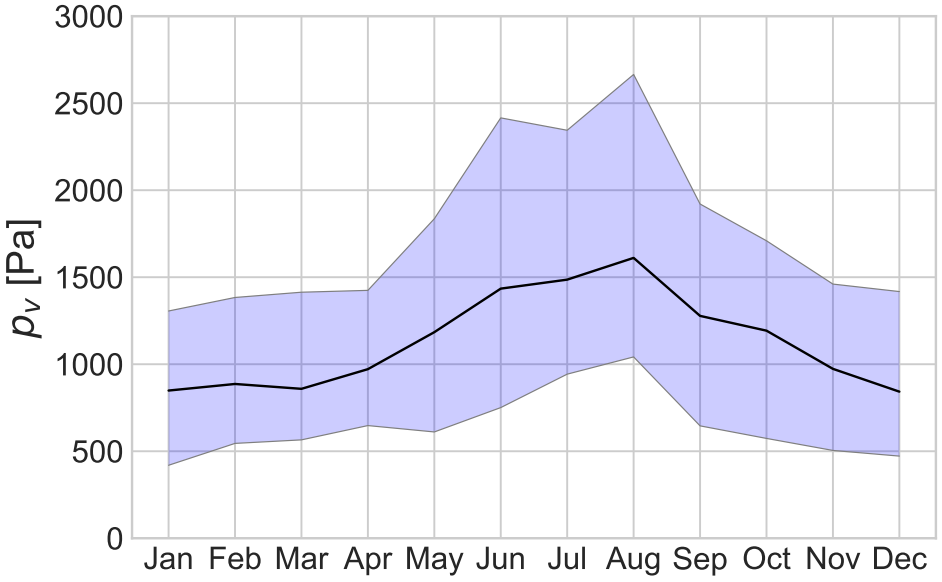

Figure B.2 – Yearly vapour pressure in Trappes: average vapour pressure and vapour pressure range in blue

B.2 Hong Kong

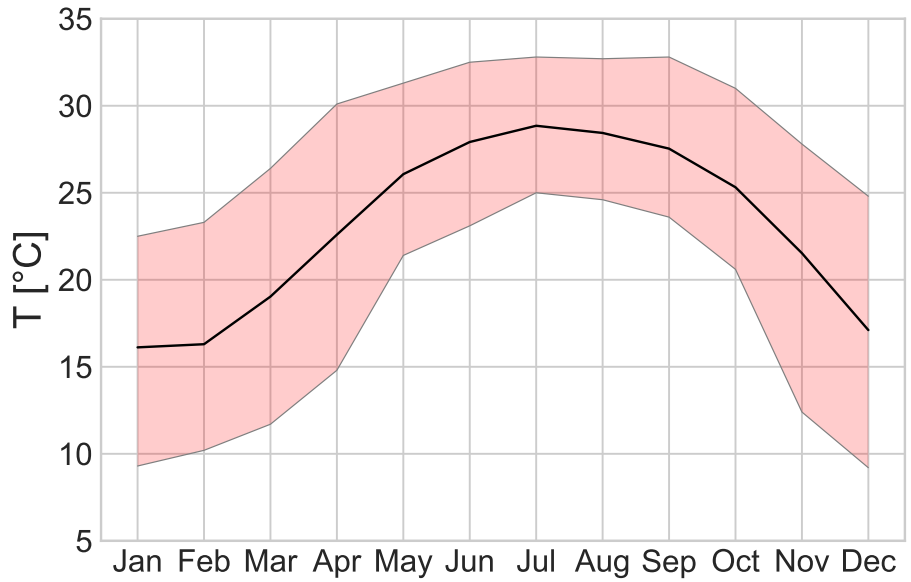

Figure B.3 – Yearly temperature in Hong Kong: average temperature and temperature range in red

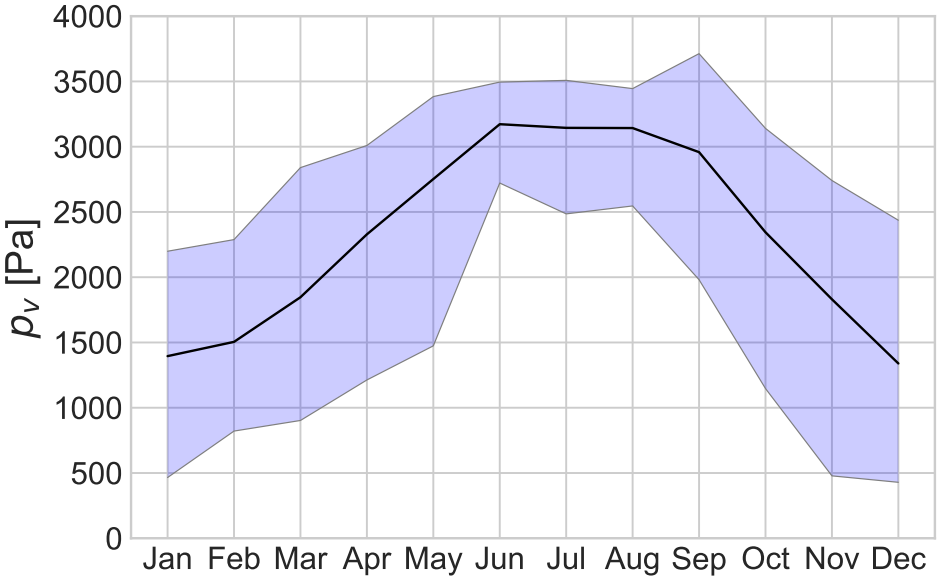

Figure B.4 – Yearly vapour pressure in Hong Kong: average vapour pressure and vapour pressure range in blue

B.3 Toronto

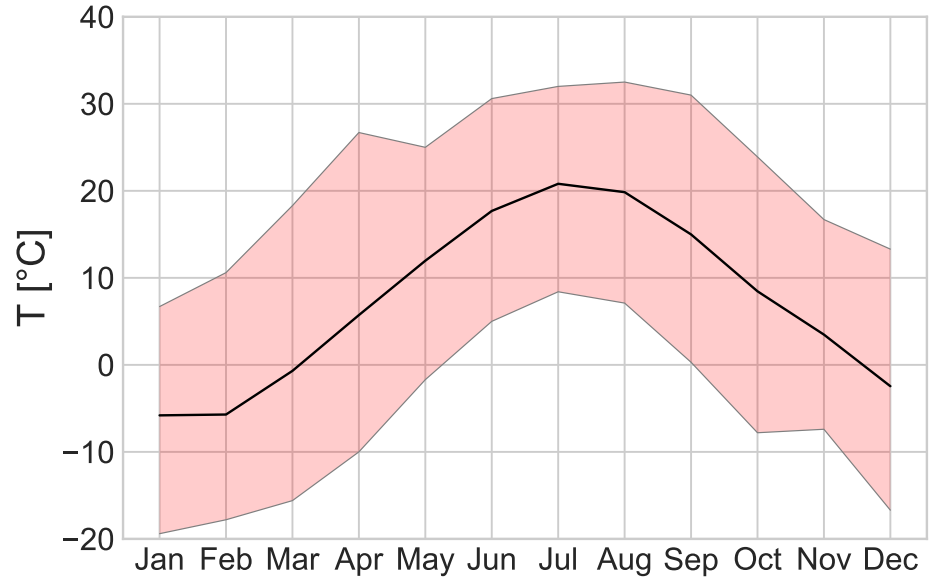

Figure B.5 – Yearly temperature in Toronto: average temperature and temperature range in red

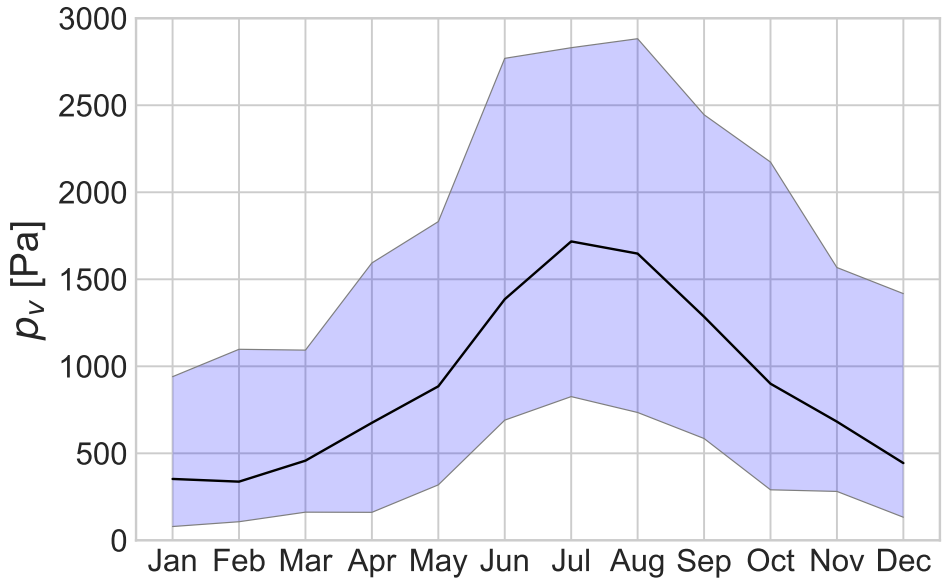

Figure B.6 – Yearly vapour pressure in Toronto: average vapour pressure and vapour pressure range in blue

Appendix C

Water vapour fluxes representation

C.1 Trappes climate

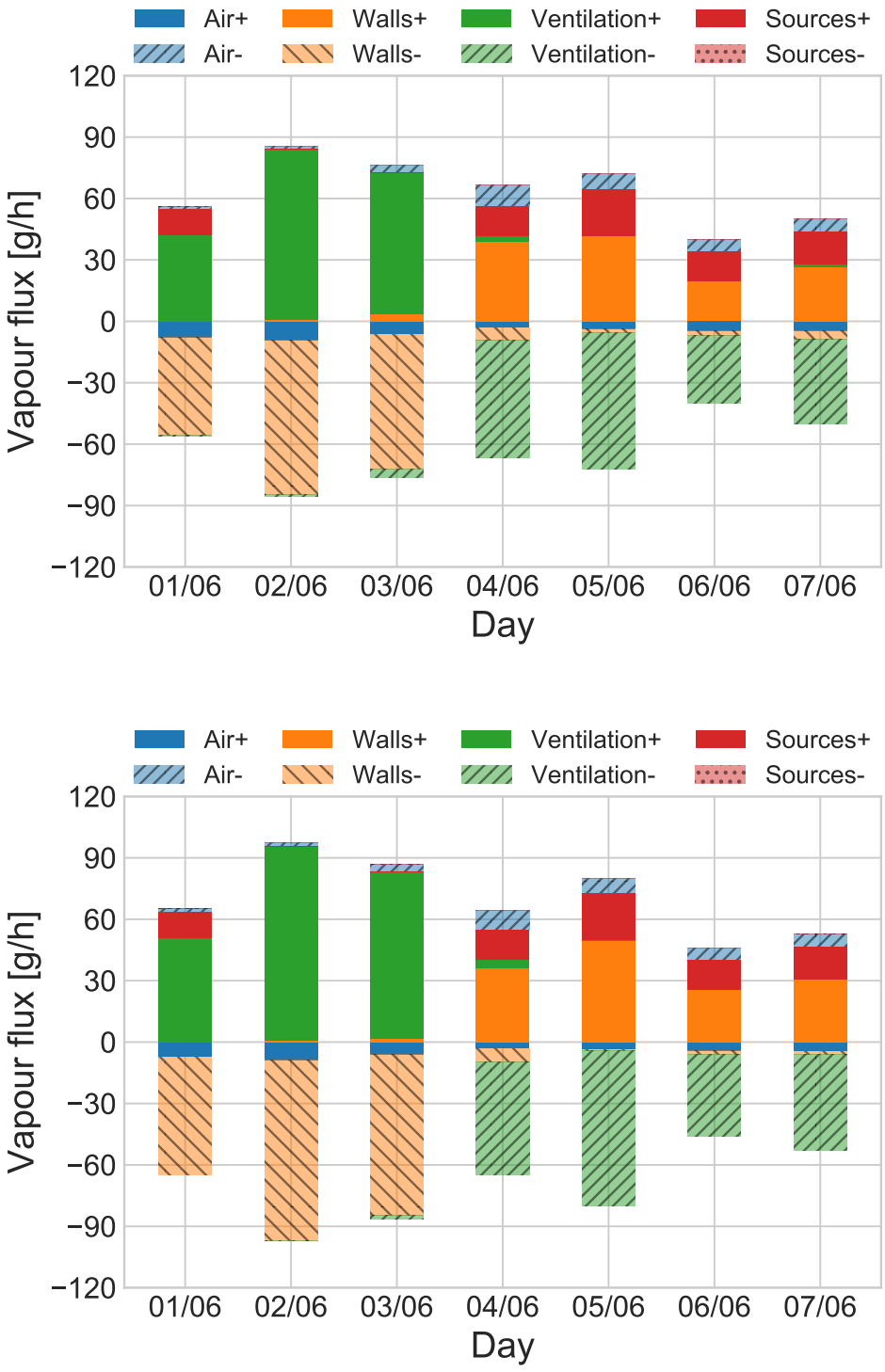

Figure C.1 – Vapour fluxes representation for $P_{12.5}$ and $P_{37.5}$ (from top to bottom) for Trappes climate for the first week of June

C.2 Hong Kong climate

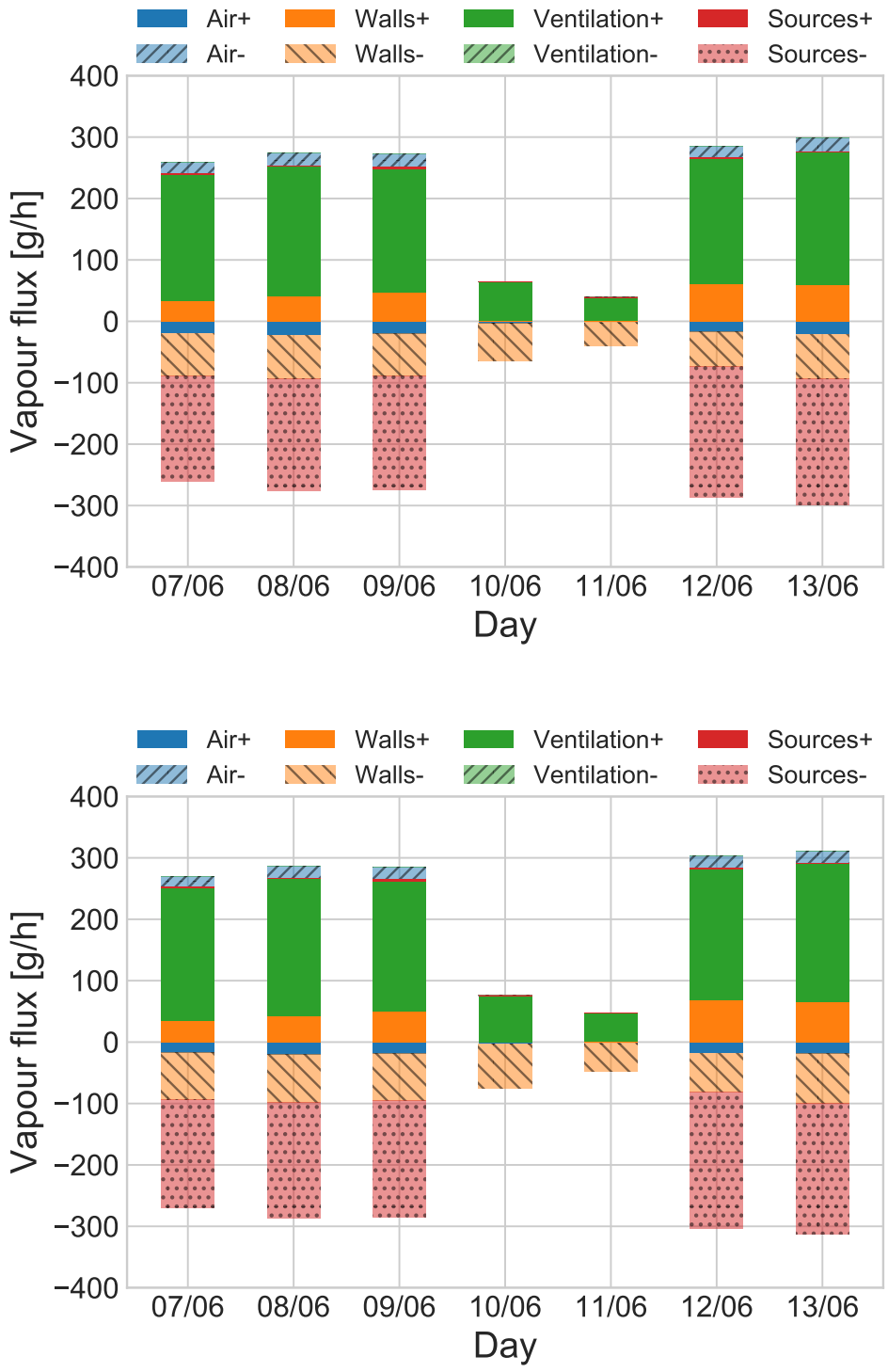

Figure C.2 – Vapour fluxes representation for $P_{12.5}$ and $P_{37.5}$ for Hong Kong climate for the second week of June

C.3 Toronto climate

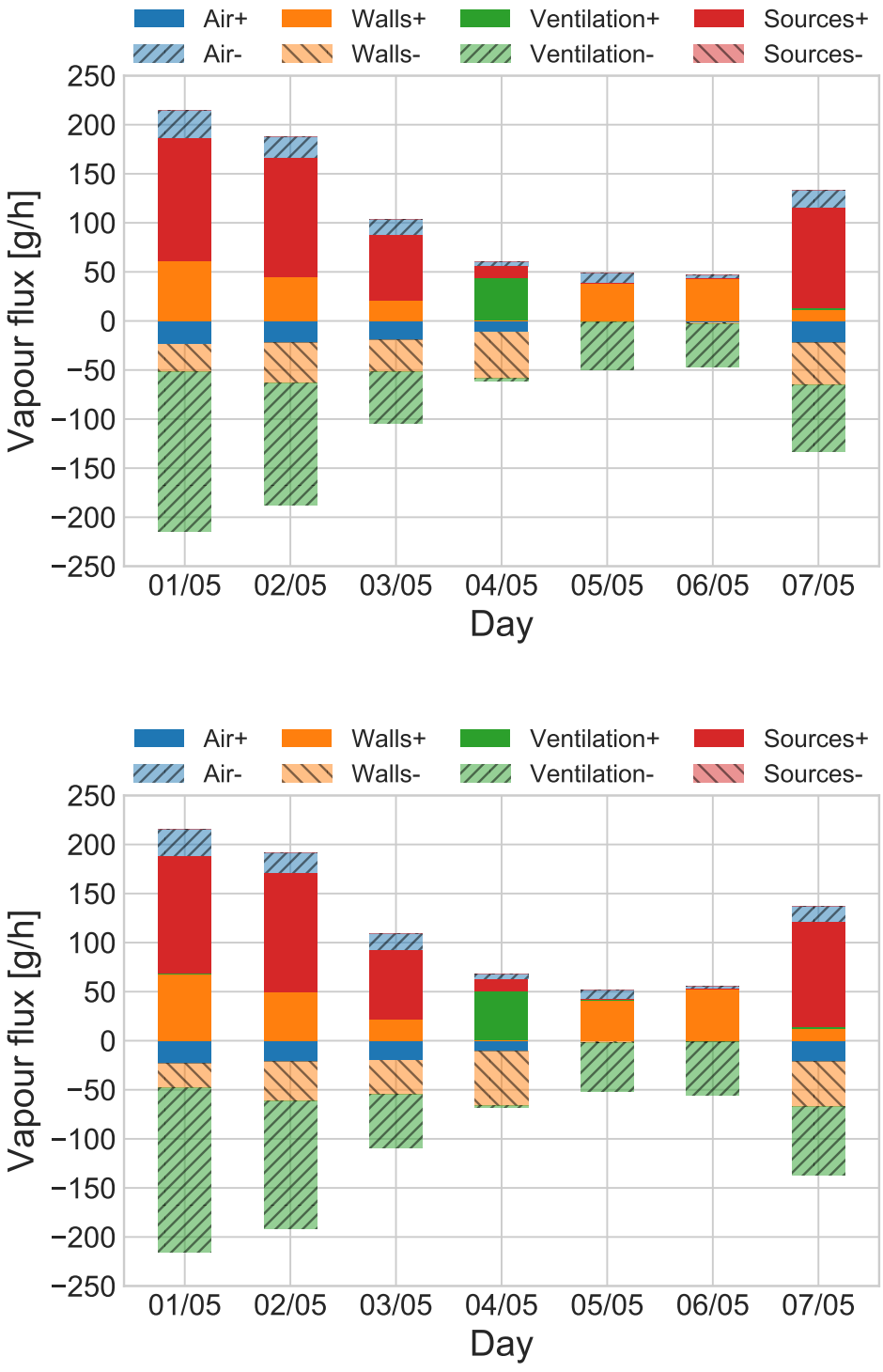

Figure C.3 – Vapour fluxes representation for $P_{12.5}$ and $P_{37.5}$ for Toronto climate for the first week of May